Lidar measurements of Bora wind effects on aerosol loading

Maruška Mole

University of Nova Gorica, Vipavska 13, SI-5000 Nova Gorica

Abstract

In the paper the analysis of wind measurements using two ultrasonic anemometers and a Mie-scattering lidar system is presented. Wind measurements with ultrasonic anemometers enabled a detailed analysis of wind direction and wind gusts in Vipava valley in winter 2015. During the same period the aerosol loading in the lower atmosphere was observed using a lidar system with wavelength of 1064 nm. Both data sets were analyzed in order to determine the correlation between wind speed and periodic structures appearing in some of the lidar measurements. The observed periodic structures are believed to be the orographic/gravity waves induced by the steep local orography. The influence of the wind on the height of planetary boundary layer was studied as well, focusing on the development of planetary boundary layer during the episodes of Bora wind. The height of well mixed lower level of atmosphere was used to obtain the depth of atmosphere with the strong wind during those episodes.

Keywords: downslope wind, lidar observations, gravity waves

1. Introduction

Bora wind is a phenomenon well known in south-west (SW) part of Slovenia as well as along the Croatian coast line, where it reaches its peak magnitudes around the town of Senj [1]. The occurrence of Bora wind in SW Slovenia is a consequence of the stably stratified air-masses flowing from NE over the ridges of Trnovski gozd, Nanos and Javorniki plateaus to Vipava valley and Karst region. The flow of cold air down the slopes

Email address: maruska.mole@ung.si (Maruška Mole)

causes strong winds at the lee side of the barrier [2], with the strongest gusts observed directly under the barriers.

In general winds caused by the flow over the barrier are called downslope winds [3]. They typically occur when stably stratified air is forced to rise over a topographic barrier. The topographic barrier causes the air to oscillate and form the so-called mountain waves, which can be classified as inner gravity waves. The direct consequence of such waves is a drag to the upper level of atmosphere, possible clear-air turbulence (CAT), which can be dangerous to the aviation, and strong surface winds blowing down the lee side of the mountains.

Using the Mie-scattering lidar one can observe the transport of aerosols in lower layers of atmosphere as well as the clouds above the planetary boundary layer (PBL). Lidar observations of aerosol structures can reveal the phenomenas in the atmosphere like gravity waves and rotors, which are hard to observe with any other technique.

2. Instrumentation and experimental set-up

The airflow behavior during the Bora wind episodes was observed using the Mie-scattering lidar system and two ultrasonic anemometers. Lidar system and one of the anemometers were positioned at the bottom of Vipava valley in urban environment with town of Ajdovščina. The second anemometer's location was at the top of the mountain barrier at Otlica observatory.

Figure 1: Mie-scattering lidar system of University of Nova Gorica (left) and ultrasonic anemometer, positioned at the rooftop in Ajdovščina (right).

Mie-scattering lidar of University of Nova Gorica uses as a transmitter the Nd:YAG pulsed laser with a wavelength of 1064 nm and has a range of

approximately 10 km with spatial resolution of 3.75 m. For each measurement the average of 10 laser pulses was computed, resulting in approximately 1.3 Hz sampling rate [4].

Measurements of wind speed and wind direction were performed using Vaisala WMT700 2D ultrasonic anemometers, which measure the time of flight of the sound due to the wind. The anemometer positioned in Ajdovščina has a sampling rate of 1 s, while the Otlica one was running at 10 min sampling rate and was mainly used just to confirm the presence of Bora wind.

3. Lidar observations during Bora wind outbreak

The lidar observations were performed in winter 2015 from Ajdovščina, which lies at the bottom of Vipava valley and thus offers a good viewing point for the observations of cold airflow over the mountain barrier. Out of the 12 measuring campaigns 6 were made during the Bora wind outbreaks (Tab. 1), 2 of them including gravity wave-like structures, which were spotted in the graphical representation of the lidar scans. The gravity waves are expected to be present in the atmosphere when there is a strong air flow perpendicular to the mountain barrier, but can sometimes be obscured by the clouds at the heights just above the top of the mountain barrier.

Measurements were preformed at a fixed elevation angle with lidar pointing along the mountain barrier at azimuth angle of 120 ° (SE), producing time-height indicator (THI) scans. The elevation angles of the measurements for different events are stated in Tab. 1.

3.1. Variations of PBL height during the outbreak

The height of PBL changes during the day due to solar radiation. One would expect a thin layer during the night, while in day time PBL height usually grows, especially if the day is sunny [5]. In some of the Bora cases the observed height of PBL stayed constant while the wind was strong enough, but started to grow after the wind gusts slowed down. This behavior indicates the layer in which Bora wind takes place is thin and it does not interfere with the upper layers by mixing, only by the shear at the top of the layer.

3.2. Orography induced waves above PBL

In two cases out of 6 the structures resembling the gravity waves were observed at the hight slightly above the mountain barrier height (Fig. 2). Gravity waves in general occur when the direction of airmass motion is

Date	Dur. [h]	El. [°]	WD [°]	Type of wind event
24. 2. 2015	1	20	60	strong Bora wind
26. 2. 2015	1	20	130	mild SE wind
27. 2. 2015	2	20	60	medium Bora wind
5. – 6. 3. 2015	70	30	130	mild SE wind
9. 3. 2015	2	48	130	mild SE wind
10. 3. 2015	8	48	60	mild Bora wind
12. 3. 2015	5.5	24	60	mild Bora wind
17. 3. 2015	8	23	60	strong Bora wind
5. 4. 2015	1	35	130	mild SE wind
13. 4. 2015	3	33	270	mild W wind
14. 4. 2015	8.5	30	60	mild Bora wind
16. – 17. 4. 2015	33	22	270	mild W wind

Table 1: Lidar measurements within the Winter 2015 and corresponding wind events. The second column presents the duration (Dur.) of each lidar measurement, third column the elevation (El.) angle of the lidar scan, while wind direction (WD) and type of wind event are obtained from wind data collected with ultrasonic anemometer in Ajdovščina. The wind speed is classified as follows: mild – peak value of wind speed distribution in range $0 - 3\,\mathrm{m/s}$, medium – peak in $3 - 6\,\mathrm{m/s}$, strong – peak in $6 - 9\,\mathrm{m/s}$.

perpendicular to the mountain barrier. The study of wind direction in Ajdovščina showed that the wind direction in Bora wind outbreaks can vary quite significantly, depending on the synoptic situation over the region. These variations in wind direction could explain why the waves were not observed in all of the cases.

4. Analysis of wind and aerosol loading properties

Within the selected period of 3 months (February – April 2015) 19 Bora wind episodes were identified, 5 of which were classified as strong events (peak of wind speed distribution in range $6 - 9\,\mathrm{m/s}$), 9 as medium ($3 - 6\,\mathrm{m/s}$) and 5 as mild Bora wind events ($0 - 3\,\mathrm{m/s}$). To declare a Bora wind event more than 10 % of wind direction should be between NE and ENE.

4.1. Periodicity of the Bora wind

Bora wind is known for its strong gusts, which haven't shown any significant period, which would be common to all the events. Studies of periodicity report the frequency range of wind gusts from 3 – 8 minutes [6, 7]. The study performed on wind data collected with cup anemometers in 2012

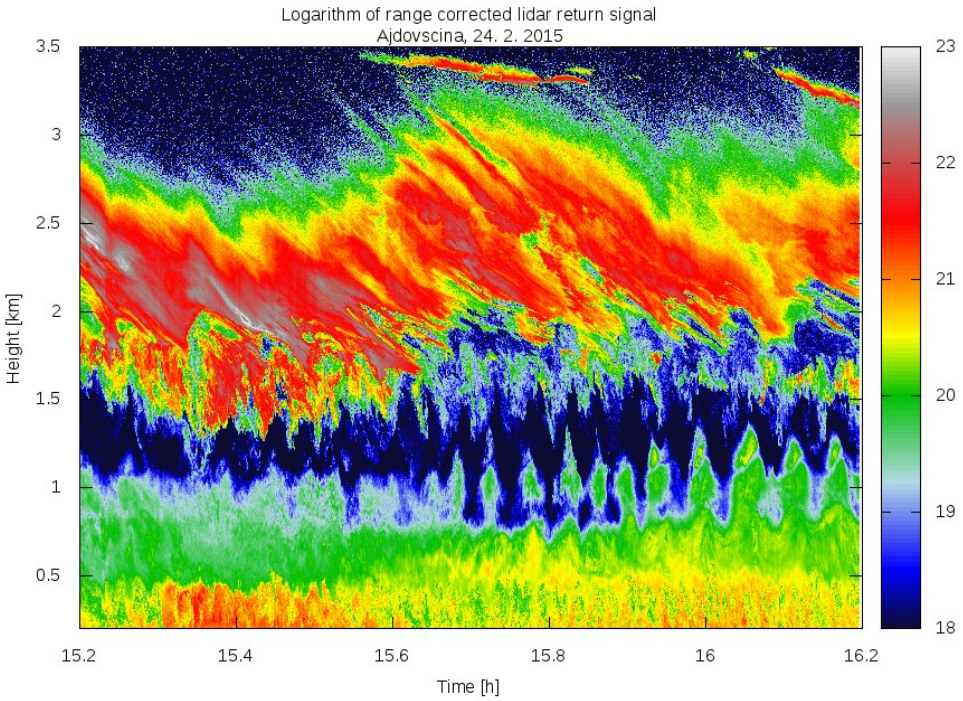

Figure 2: THI scan of the atmosphere during the Bora wind outbreak, taken in Ajdovščina on 24. 2. 2015 at elevation of 20 °. The color scale shows the logarithm of lidar return signal in arbitrary units. PBL height in the shown scan is within the range from 0.8 to 1.2 km, while the strong response between 1.4 and 3 km corresponds with the cloud layer present at the time of the measurement. The top of the PBL is experiencing a sort of a periodic behavior, which could be related either with the Bora wind gusts in the lower layer of atmosphere or with the gravity waves induced by the mountain barrier.

in Vipava valley confirmed the range, though the period of the gusts appears to be a characteristic of a single event, not as a Bora wind event in general.

4.2. Correlation between wind speed and aerosol loading at different heights

The analysis of lidar observations during Bora wind events was performed in order to study the possible correlations of aerosol loading and PBL height with the wind at the ground level. Lidar system measures the scattering of light on the aerosol particles, which are assumed to be light enough to move with the wind. The correlations between wind speed and the lidar response at fixed range were computed, resulting in the values of correlation coefficient within the range from 0.1 to 0.2. The analysis of the

correlations between wind speed and PBL height did not yield any significant correlation, which is most likely due to many factors that can affect the PBL height alongside with the wind speed (solar radiation, wind shear above the PBL height ect.).

5. Conclusions and future work

The aerosol loading in the lower layers of the atmosphere is affected by different factors, one of which is the wind speed. To further study the effects of the wind more advanced techniques of lidar scan analysis have to be developed, which will enable the separation of the atmosphere in different layers according to the characteristics of the single layer. Better separation of different atmospheric layers will make it easier to study the fluctuations in PBL height as well as helping identify the layers most affected by the wind.

References

[1] Z. Petkovšek, *Burja v Sloveniji in nekoliko južneje*, Pol stoletja Slovenskega meteorološkega društva, Ljubljana: Slovensko meteorološko društvo, 251-268 (2004).

[2] M. Žagar, J. Rakovec, *Characteristics of the Bora wind under different conditions of the lee background flow*, 29th International Conference on Alpine Meteorology ICAM 2007, Extended Abstracts, vol. 2, 309-312 (2007).

[3] D. R. Durran, *Downslope winds*, Encyclopedia of Atmospheric Sciencies, Elsevier Science Ltd., 644 - 650 (2003).

[4] T. He, *Study of atmospheric aerosol transport processes on local and regional scales*, Doctoral disertation (2013).

[5] V. A. Kovalev, W. E. Eichinger, *Elastic Lidar: Theory, Practice and Analysis Methods*, Wiley and Sons, New York (2004).

[6] Z. Petkovšek, *Periodičnost sunkov burje*, Razprave, vol. 20, 67 - 75 (1976).

[7] D. Belusić *et al.*, *Quasi-periodic bora gusts related to the structure of the troposphere*, Quarterly Journal of the Royal Meteorological Society, vol. 130, 1103 - 1121 (2004).

Analysis on the process of Sahara-dust detected by polarization lidar in Slovenia

Longlong Wang

University of Nova Gorica, Vipavska 13, SI-5000 Nova Gorica

Abstract

Long range tranport of aerosols over Slovenia, in particular mineral dust from nothern Africa was studied using polarization lidar device. Based on the theoretics of polarization lidar which were briefly described in the paper,and a new lidar system developed was shown. One course of the dust aerosol were observed by the lidar system in Ajdovscina, Slovenia (45.93N, 13.91E) The analysis of lidar data with regional dust modeling (DREAM) revealed the characteristics and distributions of the Sahara dust. In the upper region, large aerosol concentrations last a few days; during two events of Sahara dust were detected and forecasted. The backscattered intensity, depolarization ratio, extinction coefficient and aerosol optical depth obtained by lidar data used to analysis the transportion of Sahara dust events. The lidar data analysis show that the Saharan dust layer height reach and persist at 8-10 km altitude, and for the Saharan dust days, the boundary layer rese up to around 2.5 km, which was higher than before this event came out. The extinction coefficient from 0.2 to 10 km altitude were obtained using Klett's method. Meanwhile, aerosol opticl depth (AOD) was calculated which compare with DREAM can get fine consistency. By using the backward trajectories, the measured aerosol types have been related to the large-scale transport to the source regions.

Keywords: mineral dust, lidar, depolarization ratio, DREAM

1. Introduction

Mineral aerosols are amog the principal constituents of tropospheric aerosols. These dust particles are expected to produce a considerable in-

Email address: longlong.wang@ung.si (Longlong Wang)

fluence on the Earth radiative budget, through direct forcing, and indirect effects, that is, influencing the cloud nucleation processes and the cloud microphysical properties. A large uncertainties on the microphysical and optical properties, as well as on the global distribution of these particles, exist. The Saharan desert constitutes one of the main sources of mineral aerosols. The Saharan dust is a mixture of sand and dust from the Sahara desert, the vast desert area that covers most of North Africa. the strong wind can blow over deserts-whipping up dust and sand high into the sky [1]. The wind in the upper part of the atmosphere then transports the dust in the direction in which it's travelling, often towards the Europe. It can be transported worldwide, covering thousands of miles [2]. The Saharan dust commonly observated over southern Europe, and it happens several times per year when strong dust storms in the Sahara coincide with northern winds to bring dust to Slovenia as well. Some of dust as the migration process of continuous transmission settlement, scattered on the transmission line, and there are some small particles into the stratosphere to form a stable layer of dust layer, regardless of which kinds, they have a direct impact to air radiation and atmospheric climate [3]. Saharan dust deposition influences the bochemical cycels of Slovenia, and interface with the monitoring of the incidence of anthropogenic emissions on ambient air $PM_{2.5}$ levels over southern cetral of Europe [4]. In the regions neighboring deserts, mineral dust also represents a risk for human health [5] and air transport activites. In order to understand that it changes and its features, particularly for sandstorm monitoring. There are many monitoring methods, such as satellite, radar, sounding and so on. Monitoring dust with lidar is an effective means, which can from the ground to observe the changing and sturcture of dust.

Polarization lidar is a post-effective detection tool to detect the particle morphology of non-spherical particles using depolarization properties of sacttered Light. Aerosol particles of different shapes are generally divided into spherical and non-spherical particles, reflecting different properties, and the dust is one kinds of non-spherical particels in solid [6]. Polarization lidar can be applied into effectively distinguishing the different type of aerosol particles. The continuous observation on aerosol depolarization ratio will contribute to the analysis of the climate evolution and meanwhile, it is also significantly important in forecasting the source of polluting aerosols. Understanding of the atmospheric aerosol radiation, climate, environment and other effects, the study or aerosol physical and optical properties of the atmoshere will be necessary, to bring great significance of the detection of vertical resoluntion of atmospheric. Therefore, the

using of Polarization lidar detect the characteristics of shape of particales during these weathers has great significance for evolution of the climate reseach and prediction.

2. The detection theory of polarization lidar

2.1. The basic detection principles of polarization lidar

In the atmosphere, except for a few liquid particles which are spherical, most of the aerosol [7] particles are non-spherical particles. Different shapes of particles generated echo signals of backscatter having a different polarization properties, while the polarization lidar takes advantage of detecting depolarization ratio of non-spherical particle to study their optical and physical properties of the atmosphere. The schematic diagram of depolarization principle of aerosol particles contained by atmosphere shown in Figure 1:

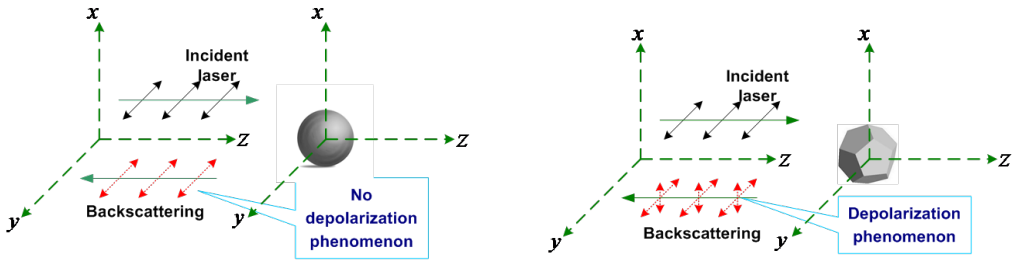

Figure 1: The schematic diagram of spherical and non-spherical particales depolarization, the figure in left is sacttering by particels in liquid and the figure in right is sacttering by particels in solid.

Can be seen from Figure 1, when sacttering particles are spherical and non-spherical, the backscatter is linearly polarization light based the on light sacttering theory of particles, and the vibration direction of electric vector is identical of incident light. However, in the case of non-spherical scattering particales, even if the incidet light is linearly polarized light, the light of backscatter generated also trens to be partially polarized light, which is called the phenomenon of depolarization.

2.2. Lidar equation and inversion method

When polarization lidar was probing the atmosphere, the ecah of parallel and vertical components of atmospheric backscattering power at the

range of r satisfy from the lidar equations as the following [8]:

$$P_p(r) = \frac{\kappa_p P_t}{r^2}\beta_p(r)\exp[-2\int_0^r \alpha_p(z)dz] \tag{1}$$

$$P_s(r) = \frac{\kappa_s P_t}{r^2}\beta_s(r)\exp[-\int_0^r (\alpha_p(z)+\alpha_s(z))dz] \tag{2}$$

Where $P_p(r)$ and $P_s(r)$ represent lidar received backscattering at the height r of the parallel and straight components of the echo power (unit: W), the subscript p and s represent both directions parallel and perpendicular transmited to the direction of laser polarization; P_t is the laser emission power; $\beta_p(r)$ and $\beta_s(r)$ represent the parallel and vertical component of the backscattering coefficient at the height r of the atmosphere (unit: $km^{-1}sr^{-1}$); $\alpha_p(r)$ and $\alpha_s(r)$ represent the parallel and vertical component of the extinction coefficient at the height r of the atmosphere (unit: km^{-1}); the k_p and k_s represent the system constants of parallel and vertical components of the detection channel, depending on the optical efficiency and quantum efficiency of each detection channel.

Thus, on the condition of sacttering, as the emitting linearly polarization laser, the intensity of light which received by telescope and its characteristics of polarization inferred the morphological characteristics of the scattering particales, and the spatial distribution of the optical properties of the atmoshere spherical and relative properties of non-sperical particles, such as the presence of characteristics parameters. First, assume that the lightt emitting atmosphere is a horizontal linear polarized light, and the intensity of it is I_0. After the atmospheric particle scattering, the backscattering light is not maintain the original linear polarization any longer. However the polarization state is not only in the horizontal direction, of which the intensity is I_2, but also contains polarized light in the vertical direction, of which the intensity is I_1, wherein the component is the depolarization effects from non-spherical particles. Thus, there is the vertical component of the backscattering intensity I_1 and the horizontal component of the echo signal intensity I_2. The ratio is defined as the linear depolarization ratio, that is [9]:

$$\delta = \frac{I_1}{I_2} \tag{3}$$

Based on the different value of I_1 and I_2, the value range of depolarization ration is changing from 0 - 1, and the numerical value show the level of particales in non-sperical. The higher numerical value indicates the particales in non-sperical account for higher ration. Therefore, using

depolarization technology can detect the distributions and microphysical properties of particales in non-spherical.

2.3. Lidar systems

Table 1: Specifications of the depolarization lidar.

Transmitter	Nd:YAG pulsed laser	Receiver	Cassegratin tlescope
Wavelength	355 nm	Detectors	PMTs
Pulse energy	150 mJ	Data recorder	Licel TR40-160
Pulse duration	8 ns	Beam splitting	PBS
repetition rate	10 Hz	Data inversion	PC

We can see Specifications of the system are summarized in Table 1 and a configuration of the polarization lidar system in Fig. 2. The lidar uses a frequency-tripled high power compact Q-Switched Nd:YAG pulsed laser. Pulse energy at the wavelength of 355 nm and pulse width of 4 ns is 100 mJ. Pulse repetition frequency is 10 Hz. The receiver was constructed using a telescope with a diameter of 800 mm and focal length of 410 mm. After light transmitted to spectrophotometric system by lens1, the echo signal is separated and extracted by spectroscopic system efficiently. In order to get echo signals in parallel and vertical components, a polarizing beam splitter (PBS) is used, then the return signals are detected by photomultiplier tubes (PMTs) for two 355nm channels. In the non-coaxial configuration of lidar system, the estimated complete overlap is from 200 m, which should be considered in the application of vertical measurements.Output of the detector is then amplified and digitized by a DAQ in analog mode. Signal averaging is performed inside the unit and a high speed data interface is applied to connect to the host computer, which allows readout of the acquired data between successive laser shots. Then analysed by computer.

3. Dust Regional Atmospheric Modeling (DREAM) System

DREAM (see [10, 11] for details) is a regional model designed to simulate and/or predict the atmospheric cycle of mineral dust aerosol. It solves the Euler-type partial differential nonlinear equation for dust mass continuity. DREAM is fully inserted as one of the governing equations in the atmospheric NCEP/Eta atmo- spheric model. The concentration equation simulates all major processes of the atmospheric dust cycle. During the

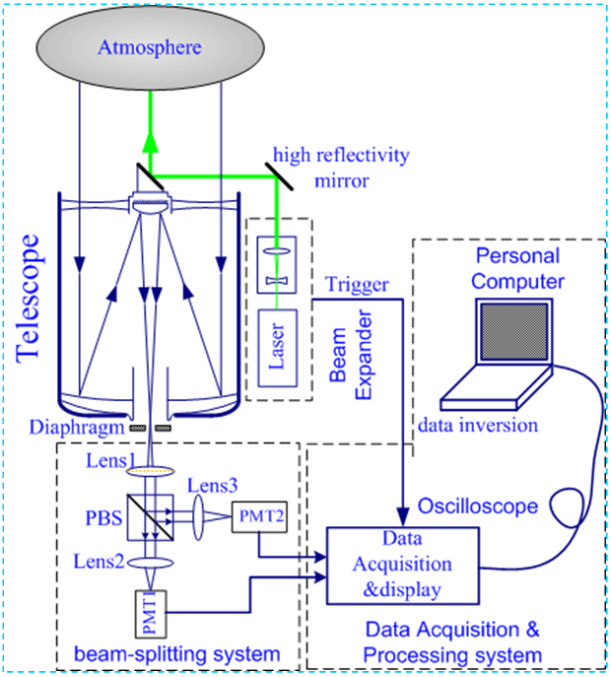

Figure 2: The configuration of the polarization lidar system. A de- tailed description of the beam-splitting system is shown as an enlargement. PBS: Polarization beam splitter, PMT: Photomultiplier Tube.

model integration, calculation of the surface dust injection fluxes is made over the model points declared as deserts. Once injected into the air, dust aerosol is driven by the atmospheric model variables: by turbulent parameters in the early stage of the process when dust is lifted from the ground to the upper levels; by model winds in the later phases of the process when dust travels away from the sources; finally, by thermodynamic processes and rainfall of the atmospheric model and land cover features which provide wet and dry deposition of dust over the Earth surface.

Dust loading was forecasted by DREAM model as Fig. 3 showed, The wind directions and dust concentrations were presented in part of Spain. From Fig. 3, we can deduced the dust tranported from Sahara to the Mediterranean following the wind, then got to Spain and Slovenia was passed through as well. This dust transportion case was forecasted at 14:00 CET time 16th Aprial, 2015 in Spain. At the same time, The DREAM model also show us the forecasting data in Slovenia as Fig. 4 showed. In Fig. 4, the profile in left showed the forecasting data at 4:00 CET time 16th Aprial, 2015 in Slovenia, and the profile in right showed the forecasting data at 20:00 CET time 16th Aprial, 2015 in Slovenia. From Fig 4, we can see the higher concentration of dust loading distributed in 8 - 10 km at 12:00 CET time, after 6 hours, the dust loading had a defined deposition, and mainly distribution in 6 - 9 km. In this period, pointed to this forecasting case, we did Observation using Mie lidar, in order to get correlation between the forecasting data and observation.

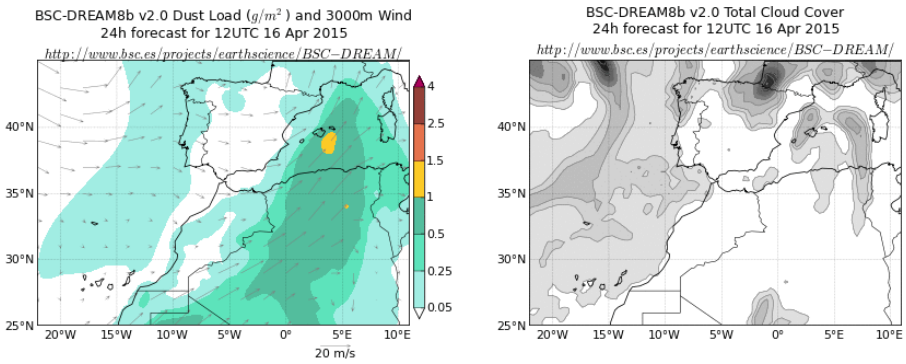

Figure 3: DREAM model dust loading in g/m^3 and winds at 3000 m on 16 April. The yellow spots indicate the location of the stations: North in Spain.

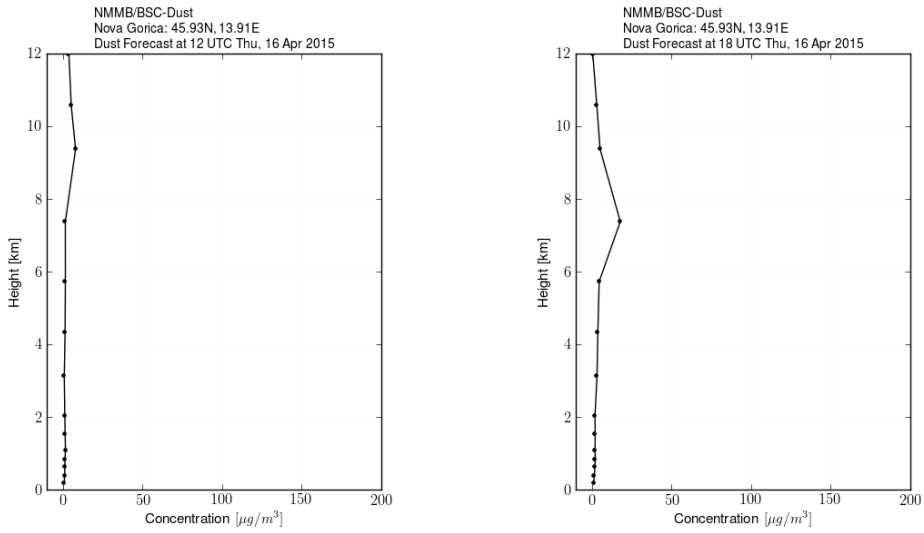

Figure 4: Dust forecast concentration profile at 14:00 CET time (left) and 20:00 CET (right) 16th. Aprial, 2015 in Nova Gorica of Slovenia.

4. Initial Observations of Sahara-dust

A preliminary analysis, based on the forcast of DREAM model and the lidar ovservations at the site, allowed the identification of cloud-free periods. The Mie lidar system in 1064 nm wavelength was employed in Ajdovscina. The measurements were observed between 12:00 and 00:00 CET on 16th April. The acquisition system is programmed to perform an integration of the backscattered signals over 600 laser shots, corresponding to 10 mins. The vertical resoluntion of the measurements is 3.75 m. The analyses have been carried out on 60 mins signal averages, corresponding to 3600 laser shots. An detected result by the lidar with elevation angle of 30^0 during the experiment over a period of about 12 hours. The time-height-indication (THI) diagram which was calculated by height-square-corrected presenting the variation of atmospheric extinction is shown in Fig. 5. Red indicates relatively high concentrations, and light blue are lowest. Fig. 5 is the Saharan dust layer structure obtained in Ajdovscina of Slovenia (45.93N, 13.91E), and it can be clearly seen that the dust layer around 8-10km from 12:00 to 17:00, then the layer descended to about 6-8 km. the data released by DREAM model forecasted had the strongest concentration of dust around 10 km height at 12:00 CET and 8 km at 18:00 CET,

therefore, it showed good homogeneity between realistic observations by lidar and forecasting by DREAM model.

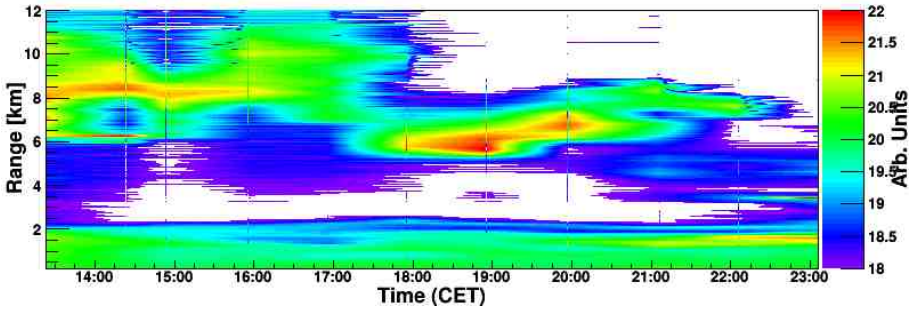

Figure 5: Time-height-indication diagram of atmospheric extinction shows the variations of atmospheric conditions from 0.1 - 12 km altitude during the 12:00-24:00 16th April 2015 in Ajdovscina of Slovenia (45.93N, 13.91E). Times refer to CET. The height which was calculated by 30^0 elevation angle of lidar is given relative to the altitude of the lidar site.

The atmospheric boundary layer (ABL) height on the basis of measurements from 12:00 to 24:00 16 April is shown in 6. The ABL height is higher than 2 km. However, the average ABL height during autumn in 2010 was about 1.35 km above the lidar site. In general, the ABL height in Europe is typically less than 2 km. The lidar results of aerosol extinction showed that aerosol loading could change totally by Saharan dust events, which is long range tranport over Slovenia.

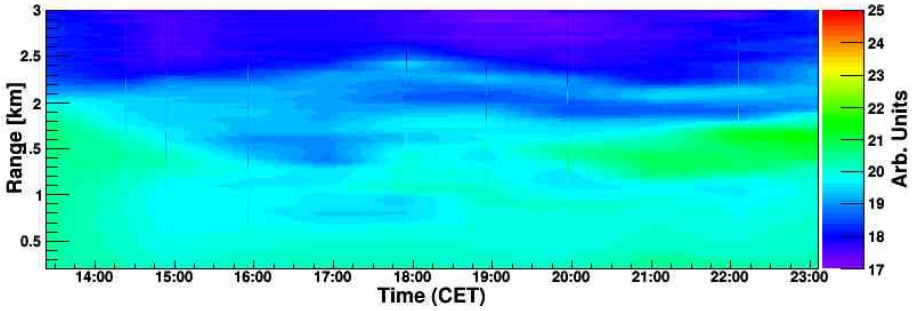

Figure 6: Time-height-indication diagram of atmospheric extinction shows the variations of atmospheric conditions from 0.1 - 3 km altitude during the 12:00-24:00 16th April 2015 in Ajdovscina of Slovenia (45.93N, 13.91E). Times refer to CET. The height which was calculated by 30^0 elevation angle of lidar is given relative to the altitude of the lidar site.

Fig. 7 shows that, in 16th of the dust weather, the atmospheric boundary layer every high of aerosol extinction coefficient [12] is generally more

low-level extinction coefficient close to the maximum extinction coefficient value 0.1 km^{-1}, and each time a change with time is not obvious. In Afternoon time aerosol extinction coefficient profile in a aerosol around 8000 m (Dust) concentration higher aggregation layers. Fig. 7 shows that on Apirl 16 the aerosol extinction coefficient is at a high level, close to the ground at an extinction coefficient of 0.1 km^{-1}, at 8 - 10 km height extinction coefficient reach 0.15 km^{-1} aerosol aggregation layer, delamination Structure more obvious. Therefore, from lidat data, it can be considered as a dust case, and the dust concentrated on 8-10 km. At 11 km height, the extinction coefficient reached the maximum value, it demonstrated the dust layer around 11 km height for this dust case. From the height of the dust layer, we can deduce the size of dust mainly focus on 5 - 10 μm. It will help to konw the size of dust based on the height of dust layer with the speed of deposition of dust for the next reseach.

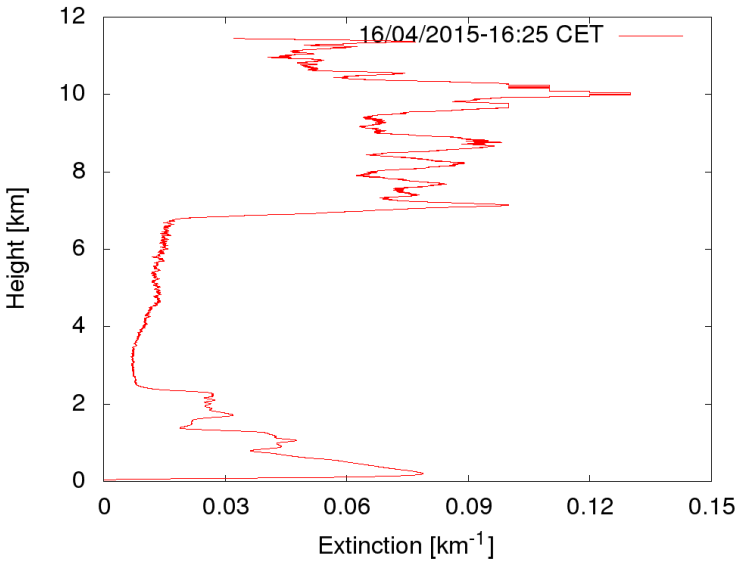

Figure 7: Observation of the lidar data from 16:04-17:04 averaged by 1 hour and extinction coefficient inverted from rang-square-corrected signal show the effect of the Sahara dust. The peak in the extinction coefficient profile between 8 - 11 km are due to the layer of dust. The measurements were performed at the fixed elevation angle of 30^o during the afternoon of 16 Aprial 2015 in Ajdovscina of Slovenia (45.93N, 13.91E).Times refer to CET. Height is given relative to the altitude of the lidar site.

5. Conclusion

In a recent Sahara-dust events in 2015, the vertical profiles of aerosol extinction coefficient, which was inverted from atmoshere of Slovenia over probe during the Saharan dust events, show significantly large aerosol layer in the middle troposphere. Combined with the DREAM forecasting data, Both them showed good consistency. Comparing with the normal day, the boundary layer in Saharan dust events was higher and rose up to around 2.5 km in midnight. The THI showed dust layer was over 8 km altitude and around 2 km thick. During Saharan dust days, the aerosol optical depths at 1064 nm wavelength were larger than 0.3 near the surface, which were much larger than nomal days. Lidar should be paly an important role in future research if observations are performed in regular time intervals with some other reasonably good density and pointed stations which use to get the concentration and radius of Saharan dust particales over a certain region in Slovenia. next work will use depolarization lidar distinguish the shape of dust to study dry dust and wet deposition during the transportion of Saharan dust events. With the local density of stations, for further analysis of imformation of sahara dust migration, structure changing, dust deposition and size distributions were studied.

References

[1] N. Tomoaki, *et al.*, *Aerosol retrieval from two-wavelength backscatter and one-wavelength polarization lidar measurement taken during the MR01K02 cruise of the R/V Mirai and evaluation of a global aerosol transport model*, Journal of Geophysical Research: Atmospheres (1984–2012) 113. D 21, (2008).

[2] S. Tetsu and Nagai, *et al.*, *Ice clouds and Asian dust studied with lidar measurements of particle extinction-to-backscatter ratio, particle depolarization, and water-vapor mixing ratio over Tsukuba*, Applied Optics 42. 36, 7103–7116 (2003).

[3] S. Nobuo and L, Choo Hie, *Characteristics of dust aerosols inferred from lidar depolarization measurements at two wavelengths*, Applied Optics 45. 28, 7468–7474 (2006).

[4] F. Volker, *et al.*, *Depolarization ratio profiling at several wavelengths in pure Saharan dust during SAMUM 2006*, Tellus B 61. 1, 165–179 (2009).

[5] G. Silke, *et al.*, *Characterization of Saharan dust, marine aerosols and mixtures of biomass-burning aerosols and dust by means of multi-wavelength depolarization and Raman lidar measurements during SAMUM 2*, Tellus B 63. 4, 706–724 (2011).

[6] F. Hyoun-Myoung, *et al.*, *Depolarization ratio and attenuated backscatter for nine cloud types: analyses based on collocated CALIPSO lidar and MODIS measurements*, Optics express 16. 6, 3931–3948 (2008).

[7] B. Luc R, *et al.*, *Range-height scans of lidar depolarization for characterizing properties and phase of clouds and precipitation*, Journal of Atmospheric and Oceanic Technology 18. 9, 1429–1446 (2001).

[8] K. Kremling and P. Streu, *et al.*, *Saharan dust influenced trace element fluxes in deep North Atlantic subtropical waters*, Deep Sea Research Part I: Oceanographic Research Papers 40. 6, 1155 - 1168 (1993).

[9] D. Yin, *et al.*, *Modeling wind-blown desert dust in the southwestern United States for public health warning: A case study*, Atmospheric Environment 39. 23, 6243 - 6254 (2005).

[10] BSC-DREAM8b v2.0 Atmospheric Dust Forecast System, `http://www.bsc.es/earth-sciences/mineral-dust-forecast-system/bsc-dream8b-forecast/north-africa-europe-and-middle-ea-0`, accessed in April, 2015.

[11] N. Slobodan, *et al.*, *A model for prediction of desert dust cycle in the atmosphere*, Journal of Geophysical Research: Atmospheres 106. D16, 18113–18129 (2001).

[12] J. D. Klett, *Stable analytical inversion solution for processing lidar returns*, Appl. Opt.2, 211–220 (1981).

Exposure of the surface detector of the Pierre Auger observatory to ultra-high energy neutrino fluence from gamma-ray bursts

Marta Trini

University of Nova Gorica, Vipavska 13, SI-5000 Nova Gorica

Abstract

High energy particles, historically named Cosmic rays, constantly reach the Earth from outer space, but their origin, composition and acceleration mechanisms are not entirely understood. Cosmic rays interact with Earth's upper atmospheric molecules nuclei and create a cascade of new particles which can be revealed at ground level by the surface detectors of the Pierre Auger observatory. Ultra high energy neutrinos will induce high inclined air showers initiated deep in the atmosphere, since neutrinos have a low interaction probability with matter. No neutrino induced shower has been detected so far. Gamma-ray bursts are supposed to produce a large high energy neutrino emission. In order to estimate the upper limit of the neutrino fluence, defined as the energy emitted in neutrinos per unit area, from a gamma-ray burst the calculation of the exposure of the surface detector is necessary. In this paper we calculate exposure of the surface detector for 43 gamma ray bursts, with zenith angle between 75 and 90 degrees, selected from GRBox catalog in the period November 2007 - May 2010 and placed the limit on the neutrino fluence from this Gamma ray bursts sample.

Keywords:
Ultra high energy neutrinos, Gamma ray bursts, Pierre Auger observatory, Exposure

1. Introduction

An open problem in high energy astrophysics is to clearly understand what is behind the huge amount of particles which are continuously hit-

Email address: marta.trini@ung.si (Marta Trini)

ting the Earth's atmosphere from all directions. These incoming particles are about 90 % protons and 9 % helium nuclei. The remaining 1 % is made of heavier nuclei, electrons, positrons, neutrinos and energetic gamma photons. When these particles interact with an atmospheric nucleon they create a shower of elementary particles that can reach the Earth's surface and can be detected. Their first discovery dates back to 1912 [1]. For some time it was believed that they had an electromagnetic nature, hence the name cosmic "rays" (CR). Even though hundred years have passed, nowadays there are still a lot of unknown aspects to comprehend. The lowest energy particles (below 10^{15} eV) are known to be produced by ordinary stars (like the Sun) and in exploding stars (Supernovae), but it was also discovered that there is a tiny fraction of higher energy (above 10^{18} eV) particles, named Ultra High Energy Cosmic Rays (UHECRs) [2], which must have a different origin. The most promising hypothesis up to now is that UHECRs are produced in Gamma Ray Bursts (GRBs) [3] and/or Active Galactic Nuclei (AGN) [4] engines. The study of the composition of the highest energy particles, determining if they are protons or heavy nuclei, it is still uncertain. Although these mysteries remain unsolved, CR study can also provide important information on the chemical evolution of the Universe and improve constraints on Galactic and extragalactic magnetic fields. On the other hand the atmospheric particle cascades could be used as a test for elementary particle physics [5].

The majority of CR are therefore charged particles, thus, they suffer of large scale cosmic magnetic field bending during they flight, making their arrival direction smeared. The rarest UHECRs will be less bent by magnetic fields therefore they should roughly keep their original direction and point towards their emission source [6]. The propagation distance of UHECRs is limited to $\sim$ 50 Mpc at $3x10^{20}$ eV, due to energy losses via interactions with the Cosmic Microwave Background (CMB) photons that induce the so called Greisen Zatsepin Kuzmin (GZK) [7] energy cutoff in the CR energy distribution (Fig. 1), i.e. the flux of incoming particles with an energy above $5x10^{19}$ eV will be largely suppressed. This feature has been seen in the UHECRs energy distribution, however, at present, we cannot be sure whether this suppression is a real imprint of the GZK cutoff or whether it is related to intrinsic limits of the UHECRs accelerator sources. The determination of the composition of UHECRs could validate one of these hypothesis [8]. The matter distribution in the Universe is not homogeneous over Mpc scales, hence if UHECRs have an extragalactic origin, one expects an anisotropy in their arrival direction distribution related to their sources, if magnetic fields are not too strong and they do not completely smear CR

trajectories. Otherwise, if UHECRs would have had a galactic origin, our galactic plane would be the prime source of the UHECR observed directions. At the moment a statistically significant departure from isotropy in the overall distribution of the arrival directions of CR with energies around the GZK cutoff has never been confirmed, but the statistic of these events is very low.

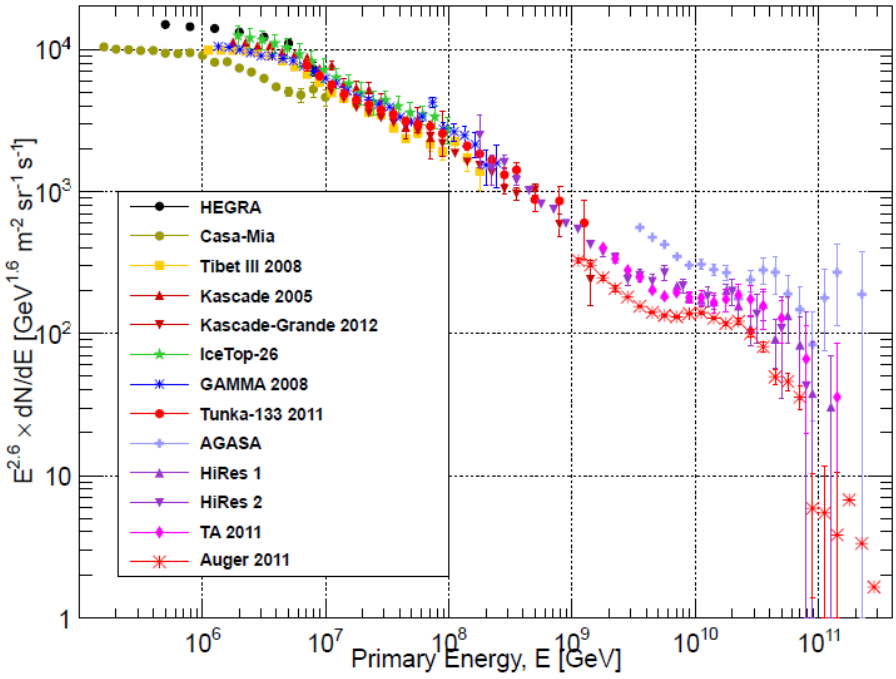

Figure 1: Energy spectrum of cosmic rays (all particles species) from air showers experiments. The fluxes are multiplied by $E^{2.6}$ to better appreciate the features. At 10^6 GeV one particle per year per m^2 is expected. At 10^9 GeV one particle per year per km^2 is expected. At 10^{11} GeV one particle per century per km^2 is expected [9]. The AGASA spectrum does not show a GZK feature, which is present in the other spectra, this is probably due to the systematic uncertainties in the energy reconstruction of the primary particle.

It is very difficult to study the production of these high energy particles without considering an associate ultra-high energy neutrino (UHEνs) component of the flux, which is produced in association with the highest

energy cosmic rays as they interact with radiation at the sources and/or with the CMB photons during their propagation. The observations of these neutrinos, differently from charged cosmic rays, will provide an unique window in astrophysical processes because these particles travel unhindered through space, pointing back to the original source and furthermore they can freely escape from environments that are opaque to photons. The absence of the observation of neutrino induced events allowed us to set the upper limit on neutrinos diffuse flux and upper limits on neutrino fluence from point-like sources. The expected spectrum of cosmogenic (i.e. originated in the GZK mechanism) neutrinos can vary considerably, depending on the spectrum and the chemical composition model of the cosmic ray sources. In the models where heavy nuclei dominate the cosmic ray spectrum, the cosmogenic neutrino flux can be suppressed by up to 2 orders of magnitude relative to CR proton dominated prediction [10], making its detection beyond the reach of current and planned neutrino telescopes. Other models consistent with the data, however, are proton dominated with only a small mixture (1 % - 10 %) of heavy nuclei and predict an associated cosmogenic flux within the reach of upcoming experiments. Over the course of the Pierre Auger experiment, ultra high energy (EeV) neutrino interactions in the atmosphere are expected to produce from zero to at most few detections.

2. Gamma-Ray Bursts

Gamma-ray bursts (GRBs) [11] are isolated bursts of gamma radiation (with $\lambda \leq 10$ pm) and, up to now, they are the most powerful singular events in the Universe. GRBs arrival directions distribution is isotropic, not biased towards any particular direction in space. If the sources were from within our own galaxy they would be strongly concentrated in or near the galactic plane. The longer GRBs are thought to be the explosion of the most massive stars in the early stages of the Universe, while the shortest are associated with the merging of neutron stars or black holes. After the initial bursts, a long afterglow across all the electromagnetic spectrum occurs and, with follow up optical observations, it is possible to identify the source of the initial GRB. Most high redshift GRB hosts are primordial faint galaxies. GRBs have been suggested as a source of UHECRs [12] accelerated in the blast wave and according to the "Fireball model" [13] neutrinos are also expected to be produced in these sources [14]. The acceleration of protons in the highly relativistic shock (i.e. collisions between faster and slower ejected shells of the exploded star) of a gamma-ray burst lead to the creation

of PeV - EeV neutrino by photopion interactions of ultrahigh energy CR (here assumed dominated by protons) with x-ray to optical photons of the GRB afterglow emission. Neutrinos are created from the decay of pions π, kaons K and muons μ in the following ways:

$$p + \gamma \rightarrow \Delta \rightarrow n + \pi^+ \Rightarrow \pi^+ \rightarrow \mu^+ + \nu_\mu \Rightarrow \mu^+ \rightarrow \overline{\nu}_\mu + \nu_e + e^+$$

$$p + \gamma \rightarrow K^+ + \Lambda/\Sigma \Rightarrow K^+ \rightarrow \mu^+ + \nu_\mu \Rightarrow \mu^+ \rightarrow \overline{\nu}_\mu + \nu_e + e^+$$

However it is important to remember that, while neutrinos travel cosmological distances to reach the Earth, we expect that ν_e, ν_μ, ν_τ are equally abundant, because of neutrino flavour oscillations [15].

3. Searching for UHE Neutrinos with Pierre Auger observatory

The Pierre Auger Observatory (Fig. 2), located in Malargüe, Argentina, is the largest existing hybrid (employing two independent methods of data collection) air shower detector [16]. It consists of an array of surface particle detectors (SD) on $\sim$ 3000 km^2 and four fluorescence telescope sites to collect the Cherenkov light (i.e. radiative emission of a particle which is moving in a medium with a velocity larger than the light phase velocity in that medium).

The SD array consists of $\sim$ 1600 purified water tank detectors arranged in a triangular grid with 1.5 km spacing between them. As charged particles enter in a tank they emit Cherenkov light which is collected by photomultiplier tubes and converted to a digital signal with a temporal resolution of 25 *ns*.

3.1. Selection criteria of neutrino search

Although the SD array of the Pierre Auger Observatory is primarily used for the collection of UHECRs, UHEνs can also be observed. Neutrinos, unlike protons and heavier nuclei, can generate deeply initiated showers into the atmosphere since they have a very low interaction probability. Using Monte Carlo simulations, it has been established that neutrino identification with the SD of the Auger Observatory can be performed efficiently as long as the search is restricted to showers with high zenith angle ($\theta \geq 75$ deg). The electromagnetic component (EM) of the inclined hadronic showers, which had initiated high in the atmosphere, will be absorbed before reaching the ground. The shower front is dominated only by muons, producing a signal which lasts tens of nanoseconds. On the other hand neutrino deep showers have a significantly large EM component at

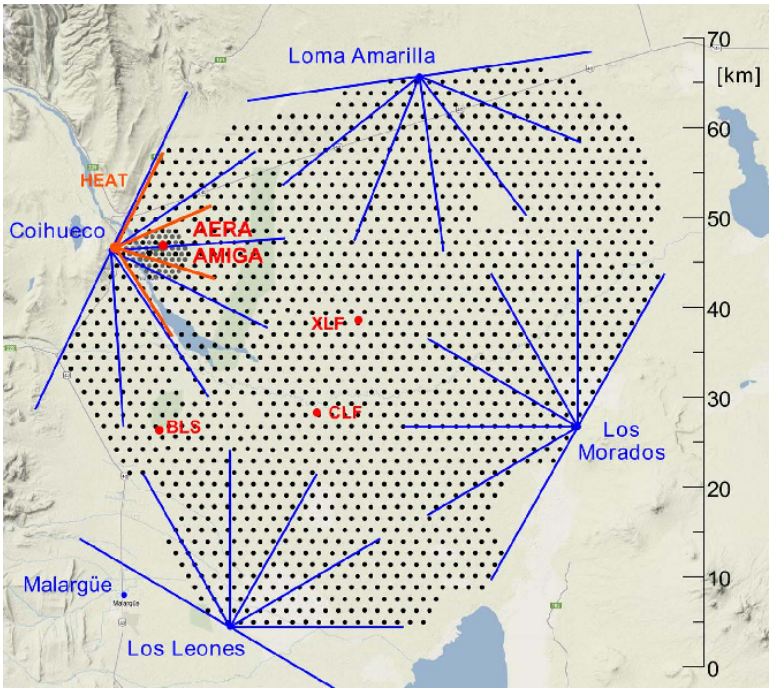

Figure 2: Layout of the Pierre Auger Observatory. Blue radial lines: view sectors of fluorescence detectors (FD), the buildings containing the telescopes are located at the edge of the array. Black dots: 1660 detector stations of the surface detector (SD). Red: new projects, three FD telescopes for higher altitudes detection (HEAT), underground muon counters (AMIGA), a radiotelescope array (AERA) for detecting radio emission from the showers.

ground, which will give a signal spread in time over hundreds of nanoseconds. Due to this feature, the large background of hadronic showers can be clearly separated from the neutrino induced showers, so that the search for neutrinos with Auger observatory is currently limited not by background but only by exposure.

3.2. Selection criteria of GRBs sample

The GRBs sample (Tab.1) for the exposure calculation has been selected with the following requirements:
1) GRBs must have declination and right ascension in the field of view of the Pierre Auger Observatory.
2) Only GRBs with high inclined zenith angle from the SD detector have been selected ($\theta \geq 75$ deg).

3) GRBs which occurred during bad periods of acquisition data inside the search period (i.e. from November 2007 to May 2010) have been excluded.
4) Low luminosity GRBs, classified as X-Ray flashes, have been excluded, since their neutrino production is disfavoured.

4. Exposure to UHE Neutrinos from GRBs

The effective area available for detection of a single GRB, which depends on the neutrino interaction atmospheric depth D measured in g cm^2, the zenith angle of the burst, as seen from the SD array, θ_{GRB} and the neutrino energy, is defined as the integral of the identification efficiency of the detector over the shower core position $\overrightarrow{r}$ with the index i that runs through the three neutrino flavours [17].

$$A_{i,eff}(E_\nu, D, \theta_{GRB}, t) = \int \epsilon_i(\overrightarrow{r}, E_\nu, \theta_{GRB}, D, t) dA$$

A combined exposure (i.e. the area of the detector times field of view in steradians times seconds) can be obtained by integrating over GRB duration time and interaction depth (Fig. 3)

$$\epsilon_{GRB}(E_\nu) = \frac{1}{m}\Sigma_i[\sigma_i(E_\nu \cos\theta_{GRB} \int\int A_{i,eff}(E_\nu, D, \theta_{GRB}, t) dD dt],$$

where m is the mass of an atmospheric nucleon, the $\cos\theta_{GRB}$ term represents the projection of the effective area onto the direction of the incoming flux and σ_i is the neutrino(ν_i)-nucleon(m) cross section for two different weak interaction processes:

$$Charged\ current : \nu_i, \overline{\nu_i} + m \rightarrow l_i^-, l_i^+ + X,$$

$$Neutral\ current : \nu_i, \overline{\nu_i} + m \rightarrow \nu_i, \overline{\nu_i} + X.$$

In charged current interactions the neutrino converts into the equivalent charged lepton l_i, where X is the final hadronic state. In neutral current interactions the neutrino remains a neutrino, but transfers energy and momentum.

5. Results

5.1. Limits to the neutrino fluence

In this work we calculated the exposure of the Pierre Auger Observatory to single GRBs UHEνs fluence. Knowing the exposure, the total number of events in a neutrino energy interval can be calculated, assuming a flux of UHE neutrinos from a single GRB, $\Phi_{GRB}(E_\nu)$, to be $k_{GRB} \cdot E_\nu^{-4}$, with an integration in energy range [17]

$$N_{GRB} = \int_{E_{min}}^{E_{max}} \Phi_{GRB}(E_\nu) \epsilon_{GRB}(E_\nu) dE_\nu.$$

Hence, the integrated limit on the value of k_{GRB} is

$$k_{GRB} = \frac{N_{up}}{\int_{E_{min}}^{E_{max}} E_\nu^{-4} \epsilon_{GRB}(E_\nu) dE_\nu}, \tag{1}$$

where N_{up} is the value of the upper limit in signal events for zero candidates and no expected background events at 90%C.L. in a Feldman-Cousins approach [18].
It is useful to calculate the limits on the fluence F_{GRB}, defined as the energy of emitted neutrinos per unit area

$$F_{GRB} = E_\nu^2 \, T90_{GRB} \, k_{GRB} \, E_\nu^{-4}, \tag{2}$$

where $T90$ is the time duration of the GRB.

To improve the sensitivity, the total expected number of the events for all the GRBs could be calculated as

$$N_{GRB} = \sum N_{GRB}$$

A corresponding k_{GRB}^{stack} and F_{GRB}^{stack} can be obtained using equations (1) and (2). We calculated the stacking limits to neutrino fluence F_{GRB}^{stack} from this GRBs sample in function of energy (Fig. 4).

5.2. Conclusions

The identification of potential neutrino-induced showers is based on first selecting those events that arrive in rather inclined directions, and then selecting among them those that have a signal spread in time, indicating deeply interacting neutrino shower. Over the Pierre Auger Observatory search period for neutrino induced showers detection, no candidate events surviving the selection criteria were found. This allow us to set the upper

limit on the UHE neutrino diffuse flux, but also to put constrains on GRBs neutrino production. In this paper we calculated exposure of the SD and constrain the UHE neutrino fluence for a 43 GRBs sample. The expected fluence of neutrino production in GRBs is too low to expect a detection. A future perspectives of no neutrino candidates could mean in principle either that GRBs are not the primary source of UHECRs or that the model for GRBs neutrino production is incorrect. Future experiments [19]will be able to make a robust statement on the connection between GRBs and neutrino emission.

Acknowledgments

Thanks to L. Yang and S. Vorobyev for the useful discussions and help with the code.

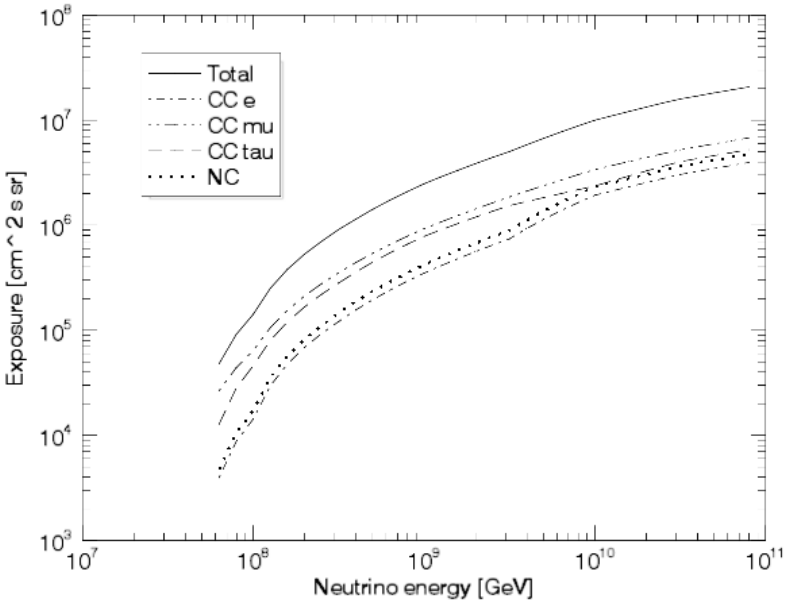

Figure 3: Exposure of the SD for a single GRB (091109B). The exposure of individual neutrino flavours and channels is shown.

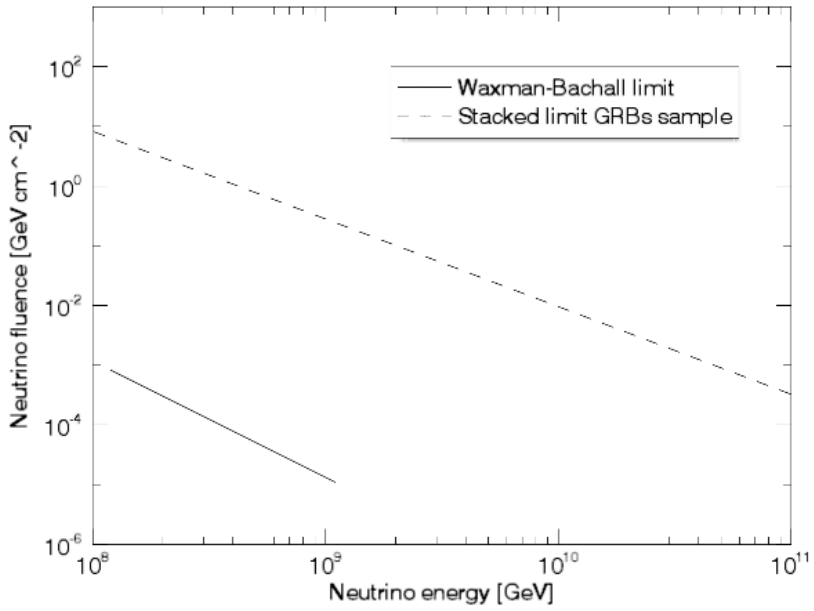

Figure 4: Limits to neutrino fluence from the GRBs sample. The theoretical Waxman-Bahcall model [3], a conservative upper limit on potential neutrino fluence, is also shown.

GRB ID	Year	θ [deg]	t90 [s]	Eb1 [GeV]	Eb2 [GeV]
100526B	2010	75.60	64.00	3.89E+05	2.26E+07
100510A	2010	84.06	31.00	1.11E+06	6.59E+06
100331A	2010	78.20	15.00	3.89E+05	1.19E+07
100225A	2010	85.09	13.00	4.52E+05	1.08E+07
100116A	2010	79.09	110.00	3.89E+05	3.43E+06
091109B	2009	89.54	0.19	3.89E+05	8.45E+05
091109A	2009	75.15	48.00	2.11E+05	4.61E+06
090915Z	2009	89.83	8.00	3.89E+05	7.75E+06
090727B	2009	78.46	25.00	5.12E+05	2.86E+06
090717A	2009	77.84	70.00	3.89E+05	2.42E+07
090706Z	2009	77.60	100.00	3.89E+05	1.58E+07
090626Z	2009	79.62	70.00	4.44E+05	8.66E+06
090625Z	2009	87.51	51.00	3.93E+05	1.47E+07
090621C	2009	76.50	59.90	5.26E+05	1.12E+07
090327Z	2009	89.46	24.00	8.74E+05	5.48E+06
090324Z	2009	77.15	30.00	3.89E+05	3.58E+06
090307A	2009	75.58	22.00	3.89E+05	1.78E+07
090222Z	2009	82.69	18.00	5.29E+05	5.55E+06
090202Z	2009	80.78	66.00	1.36E+05	5.35E+06
090201Z	2009	82.93	83.00	4.92E+05	3.22E+06
090129Z	2009	84.07	17.50	6.32E+05	5.59E+06
090117B	2009	87.67	27.00	3.11E+06	7.50E+06
081223Z	2008	87.48	0.89	2.78E+05	1.67E+06
081221Z	2008	89.92	34.00	1.01E+06	1.86E+06
081203B	2008	81.40	23.40	3.89E+05	1.26E+06
081126Z	2008	84.22	54.00	2.47E+05	7.84E+06
081121Z	2008	80.45	14.00	2.29E+05	2.31E+06
081105B	2008	80.09	0.18	3.89E+05	1.72E+06
081016B	2008	84.54	2.60	3.89E+05	9.93E+06
080927Z	2008	82.01	25.00	1.94E+06	4.06E+06
080916C	2008	87.47	66.00	5.77E+04	2.50E+05
080822A	2008	82.27	0.10	3.89E+05	1.94E+05
080727B	2008	84.88	8.60	3.44E+05	3.23E+06
080725Z	2008	82.45	120.00	5.98E+05	1.10E+07
080707Z	2008	82.48	27.10	2.43E+06	3.44E+07
080605Z	2008	83.73	20.00	3.38E+05	3.15E+06
080604Z	2008	79.05	82.00	6.00E+05	3.74E+07
080517Z	2008	89.07	64.60	3.89E+05	2.08E+07
080413A	2008	89.39	46.00	2.97E+05	4.82E+06
080319A	2008	80.27	64.00	3.89E+05	7.07E+06
080315Z	2008	78.36	64.00	3.89E+05	4.14E+07
080212Z	2008	88.75	123.00	3.89E+05	1.26E+07
080120Z	2008	81.57	20.00	3.89E+05	7.07E+06

Table 1: 43 selected GRBs grom GRBox catalog. From the left to the right: GRB identification number, year, zenith angle from the SD array, GRB duration, two energies break points (assuming the GRB spectral energy in form of power-law).

References

[1] F. Hess *Über Beobachtungen der durchdringenden Strahlung bei sieben Freiballonfahrten*, Physikalische Zeitschrift 13, 10841091 (1912).

[2] K. Kotera and A. V. Olinto *The Astrophysics of Ultra-high Energy Cosmic Rays*, ARAA 49, 119-153 (2011).

[3] E. Waxman and J. Bahcall *High Energy Neutrinos from Cosmological Gamma-Ray Burst Fireballs*, Physical Review Letters 78, 2292 (1997).

[4] W. Stecker et al. *High-energy neutrinos from active galactic nuclei* Physical Review Letters 66, 2697 (1991).

[5] L. Gonzalez Mestres *Cosmic rays and tests of fundamental principles*, Nucl. Phys. B, Proc. Suppl.212-213, 26 (2011).

[6] F. Aharonian et al. *Cosmic rays in galactic and extragalactic magnetic fields*, Space Science Reviews v.166, p.97-132 (2012).

[7] G.T. Zatsepin and V.A. Kuzmin *Upper bounds on the spectrum of cosmic rays*, Pis'ma Zhurnal Eksperimental noi i Teoreticheskoi Fiziki 4, 114 (1966).

[8] K. Kotera et al. *Cosmogenic Neutrinos: parameter space and detectabilty from PeV to ZeV*, JCAP 10, 013 (2010).

[9] T.K. Gaisser, T. Stanev and S. Tilav *Cosmic Ray Energy Spectrum from Measurements of Air Showers*, arXiv:1303.3565 [astro-ph.HE] (2013).

[10] D. Hooper et al. *The impact of heavy nuclei on the cosmogenic neutrino flux*, Astropart. Phys. 23, 11-17 (2005).

[11] P. Kumar and B. Zhang *The Physics of Gamma-Ray Bursts and Relativistic Jets*, Phys.Rept. 561 (2014).

[12] E. Waxman *Cosmological gamma-ray bursts and the highest energy cosmic rays* , Phys. Rev.Lett.75 (1995).

[13] E. Waxman and J. N. Bahcall *High-energy neutrinos from cosmological gamma-ray burst fireballs*, Phys. Rev. Lett. 78 (1997).

[14] S. Huemmer et al. *Neutrino Emission from Gamma-Ray Burst Fireballs, Revised*, Phys. Rev. Lett. 108 (2012).

[15] Y. Fukuda *Evidence for Oscillation of Atmospheric Neutrinos*, Phys. Rev. Lett. 81, 1562 (1998).

[16] R. Abraham et al. *Properties and performance of the prototype instrument for the Pierre Auger Observatory*, Nuclear Instruments and Methods, A523 (2004).

[17] P. Abreu et al. [Pierre Auger Collaboration] *A search for ultra-high energy neutrinos in highly inclined events at the Pierre Auger Observatory*, Phy. Rev. D 84, 122005 (2011).

[18] G. J. Feldman and R. D. Cousins *Unified approach to the classical statistical analysis of small signals*, Phys. Rev. D 57, 3873 (1998).

[19] M. G. Aartsen et al., *IceCube-Gen2: A Vision for the Future of Neutrino Astronomy in Antarctica*, arXiv:1412.5106 [astro-ph.HE] (2014).

Characterization of silicon photomultipliers for use in the Cherenkov Telescope Array

Gašper Kukec Mezek

University of Nova Gorica, Vipavska 13, SI-5000 Nova Gorica

Abstract

Very high energy gamma rays arriving to Earth are detected with the use of Imaging Atmospheric Cherenkov Telescopes (IACT), that observe the characteristic UV light emitted by charged particles in a large cascade. The next in line of such telescope arrays is the Cherenkov Telescope Array (CTA). The proposed cameras of large size telescopes will roughly have 1000 photomultiplier tubes (PMT), photodetectors widely used in astroparticle physics. However, with the development of new silicon based photodetectors, they are proving to be a possible replacement for the power hungry PMTs.

In this paper, silicon photomultipliers are considered for high energy physics use in the large size telescope camera of CTA. The characterization of these novel photodetectors include bias voltage, angle, teperature and position dependent measurements. Results of characterization measurements are described, which were performed as part of the Laboratory for astroparticle physics (University of Nova Gorica) contribution to the CTA consortium.

Keywords: silicon photomultipliers, Cherenkov Telescope Array, photodetector comparison, silicon photomultiplier characterization

1. Introduction

When high energy gamma rays enter the Earth's atmosphere, they interact with atmospheric molecules and produce a cascade of electromagnetic particles. Positrons and electrons in such a cascade have extremely high energy and produce a flash of Cherenkov radiation. These bursts are a

Email address: gasper.kukec@ung.si (Gašper Kukec Mezek)

result of particles traveling faster than the speed of light in the atmosphere and last for several nanoseconds. Since gamma rays are not deflected by magnetic fields, we can pinpoint the direction of their source by observing the incoming Cherenkov light. As opposed to gamma ray induced showers, extensive air showers (EAS) induced by heavier charged particles, do not show a preferred direction and produce a substantial background signal. This noise is statistically removed by determining the arrival direction, since charged particle EAS are isotropic.

The Cherenkov Telescope Array (CTA) [1, 2] is a next generation gamma ray observatory in the very high energy (VHE) regime (100 GeV to 100 TeV), that will replace or complement existing Imaging Atmospheric Cherenkov Telescopes (IACT) H.E.S.S. [3], MAGIC [4] and VERITAS [5]. It will consist of an array of Cherenkov telescopes of three different sizes:

- Small size telescopes (SST) with radius $\sim 4-6\,\mathrm{m}$ and field of view $\sim 10^{\circ}$ will cover energies above 10 TeV.
- Medium size telescopes (MST) with radius $\sim 10-12\,\mathrm{m}$ and field of view $\sim 6-8^{\circ}$ will cover energy ranges between 100 GeV and 1 TeV.
- Large size telescopes (LST) with radius $\sim 24\,\mathrm{m}$ and field of view $\sim 4-5^{\circ}$ will cover energies below 100 GeV.

With an order of magnitude higher sensitivity than current IACTs, the array will offer observations regarding the origin of cosmic rays, their acceleration to high energies and searches of physics beyond the standard model. CTA is planned to consist of two parts, one in the north, the other in the south hemisphere, which will make it the only ground based observatory with complete coverage of the sky. The detection method of Cherenkov telescopes is to collect light with a hexagonal grid of mirrors and focus it onto the plane of a camera. The camera consists of photosensitive detectors, converting the faintest of Cherenkov light bursts into a measurable electrical signal. For this purpose, the current camera design for CTA large size telescope consists of about 2500 photodetector pixels, making the size of the complete camera $\sim 2.5\,\mathrm{m}$ in diameter.

In this paper, a comparison between photomultiplier tubes and silicon photomultipliers is made for their use as photodetectors. Additionally, a measurement setup and characterization of silicon photomultipliers is presented to determine their suitability for the use in Cerenkov telescopes of CTA (at the Laboratory for astroparticle physics in University of Nova Gorica we focus on large size telescopes).

2. Cherenkov light detection

In many physics applications, a measurement of an observable is performed through detection of light with photodetectors. These photodetectors transform a small amount of incident light into a measurable signal through the use of charge carrier multiplication. In high energy physics, a photomultiplier tube (PMT) is most commonly used, but novel detectors, based on semiconductor technology, are being developed to try and solve some of the drawbacks occurring in PMTs. These drawbacks are explained in the following subsection.

2.1. Photomultiplier Tubes

Photomultiplier tubes use a photosensitive cathode to transform incident light into a measurable signal through an electron avalanche. The photocathode, upon an incident photon, emits electrons. These are then accelerated by a potential difference on the two terminals inside the vacuum tube of the PMT. Additional dynodes (electrodes in the vacuum tube) serve as electron multipliers and produce additional electrons when hit by accelerated electrons. With their multiple stage acceleration, PMTs amplify the signal with a high gain and low signal noise. However, due to their large vacuum tube and photosensitive cathode, they are very sensitive to mechanical shocks, can not be used in ambient light and are sensitive to magnetic fields. Additionally, the voltage requirements to enable electron avalanches inside the tube are in the range of $1\,\mathrm{kV} - 2\,\mathrm{kV}$ [6].

2.2. Silicon photomultipliers

Silicon photomultipliers (SiPM) are detectors consisting of a large number of avalanche photodiode (APD) cells, between 100 and 1000 per mm^2. Each APD cell has an active detection region between the p–type semiconductor substrate, with larger hole concentration, and n–type semiconductor substrate, with larger electron concentration. This detection area can further be increased by applying a reverse bias voltage (negative terminal on p–type and positive terminal on n–type). When a photon passes through the active region, it creates electron—hole pairs, that are accelerated to their respective terminals and produce additional charge carriers on their way. Each APD signal is summed to produce the final SiPM signal. Through this technique a measurable electric signal can be obtained from the passage of a single photon, making SiPMs extremely useful in low light conditions. The reverse bias voltage, as opposed to PMTs, remains under 100 V, which drastically lowers the power consumption and need of high voltage power

supplies. They produce a signal gain and light sensitivity similar to that of a PMT, but can still be used in ambient light. Due to their structure, they are mechanically robust and insensitive to magnetic fields. The most noticeable drawback to SiPMs is a fairly high signal noise, resulting from thermally produced electron–hole pairs, that can hide the true low level light signal [6].

3. Silicon photomultiplier characterization

Characterization of detectors is necessary in development stages to determine which detector to choose from and if it is suitable for the proposed application. As described in [2], CTA has selected certain criteria for photodetectors to be used for their Cherenkov telescopes. Out of all of the criteria, the following are especially important when considering SiPMs as CTA photodetectors:

- spectral sensitivity range should be $300 - 650\,\text{nm}$ with peak at $\sim$ $350\,\text{nm}$ (atmospheric extinction below and increasing noise above the range)
- ability to detect single photons and a dynamic range of up to 5000 photoelectrons
- detector lifetime of at least $\sim$ $10\,\text{years}$, with annular exposure of $\sim$ $2000\,\text{hours}$
- cross–talk (noise in pixel produced by adjacent camera pixels) must be kept below 1%

Most available SiPMs try to replicate the spectral sensitivity of PMTs and are thus well suited for Cherenkov light detection. The detection of single photons is possible, but can be hindered by thermal noise covering the signal. As for SiPM lifetime, they are extremely durable if used properly.

3.1. Measurement setup

The measurement setup was specifically built at the Jozef Stefan Institute (IJS) for the purpose of SiPM characterization and is constantly being upgraded to include a larger number of measured characteristics. The setup schematic is presented on Fig. 1 and consists of a sample holder and laser optics inside a climate chamber. The climate chamber, at the same time acting as a dark box, is a Shjianheng programmable high & low

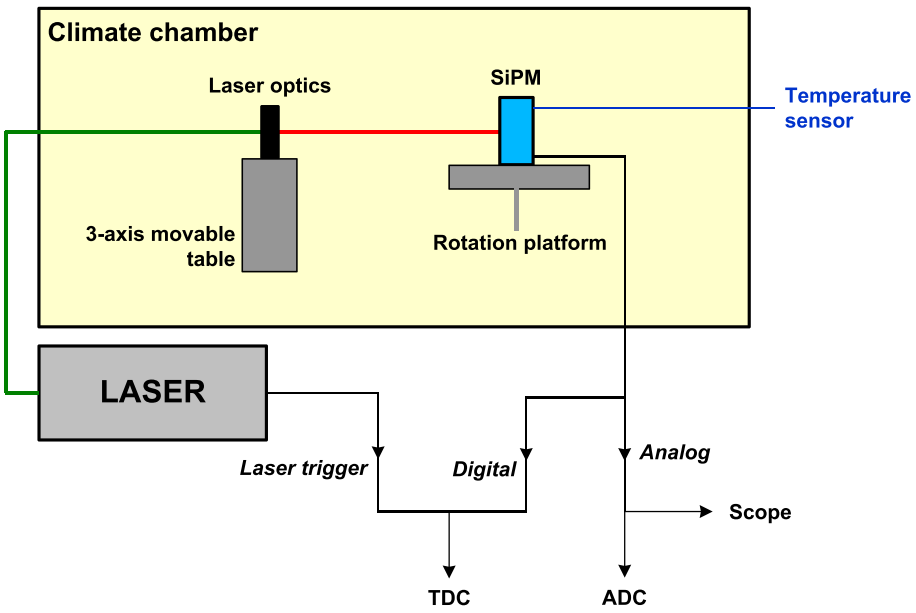

Figure 1: Schematic of the experimental setup: Laser optics system (light brought through optic fiber) and sample holder are inside a climate chamber. The laser optics are on a 3–axis movable table and the holder is stable, but can be rotated for incidence angle measurements. The laser trigger signal, combined with the SiPM signal, can be used for timing analysis (TDC). The analog SiPM signal can be used to perform waveform analysis on the oscilloscope (scope) and charge spectrum analysis (ADC). Internal temperature is more accurately measured with a temperature sensor positioned close to the sample.

temperature chamber with a temperature span between $-70°C$ and $140°C$. This temperature range is much larger than the predicted operational temperatures for CTA (between $0°C$ and $30°C$) [7]. The laser used for all measurements is a 600 nm (red) Picosecond laser (PiLAS) with variable pulse frequency, power and a possibility to exchange the laser head for different wavelength light (from UV to infrared). Before passing the laser light through an optic fiber to the laser optics inside the chamber, it is possible to place neutral density filters in front of the fiber to reduce the amount of light passing to the sample. As laser optics, a collimator lens or a pinhole are used, depending if focused light or a broad beam is needed, respectively. The optical system is then mounted on top of a 3–axis movable table to enable surface scans.

The sample holder is made from a stable metallic mount and holds the SiPM in place, while a platform enables the holder to be rotated for inci-

dence angle measurements. A temperature sensor (National Instruments FP–RTD–122) is positioned close to the sample mount to more accurately determine the inside temperature of the chamber. Part of the setup inside the chamber is shown on Fig. 2.

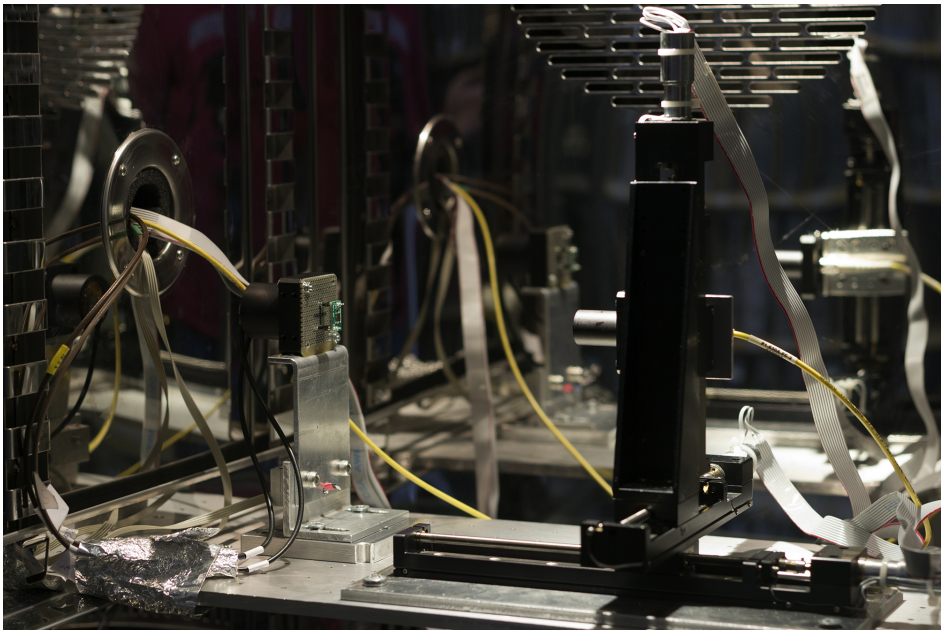

Figure 2: Experimental setup inside the climate chamber. On the left is the sample holder with an SiPM (on green board) and a temperature sensor (red). On the right is the 3–axis movable table with optic fiber (yellow) connected to the laser optics (pinhole in this case).

The SiPM testing board used for all measurements has one input (bias voltage) and one output (signal line), with simple RC filtering to reduce signal noise. Bias voltage is applied from a variable low and high voltage supply, while the signal line is passed to an inverting amplifier. The complete signal line schematic is shown on Fig. 3. The SiPM signal and the laser trigger signal are passed through different stages to a Computer Automated Measurement And Control (CAMAC) data acquisition module. With it, the gathered signal charge is measured through an Analog–to–Digital Converter (ADC) and the time difference between laser trigger and SiPM signal is determined with a Time–to–Digital Converter (TDC). Both the ADC and TDC can accommodate simultaneous measurements of 8 signals, which is useful for characterization of SiPM arrays.

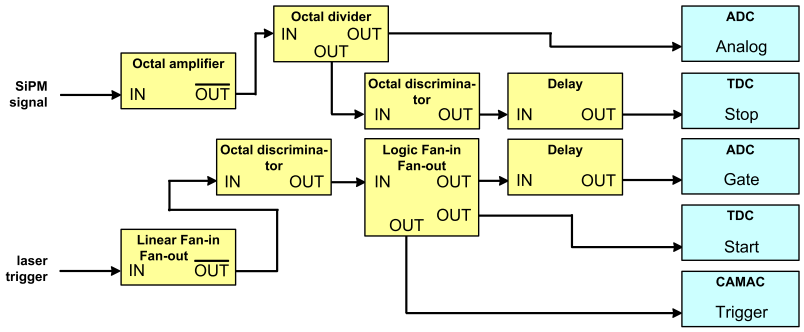

Figure 3: Signal from the SiPM is amplified and divided into analog (ADC analog) and digital parts (TDC stop). The laser trigger is inverted and spread to three digital inputs (TDC start, ADC gate and CAMAC trigger). ADC gate determines the time window where analog signal is integrated, while the two TDC inputs determine the endpoints for timing analysis.

3.2. Silicon photomultiplier samples

In order to select the most appropriate SiPM for CTA camera design, it is important to determine the characteristics of SiPMs from different manufacturers. Current SiPM manufacturers include Hamamatsu photonics [8], SensL [9] and FBK [10]. In this research, Hamamatsu S10362–11–050U [11] and FBK AdvanSiD RGB [12] silicon photomultipliers have been used. The main difference between the two is the active detector area size ($1 \times 1\,\mathrm{mm}^2$ and $3 \times 3\,\mathrm{mm}^2$, respectively) and the operating voltage ($\approx 70\,\mathrm{V}$ and $\approx 30\,\mathrm{V}$, respectively). The two samples measured for this work are shown on Fig. 4.

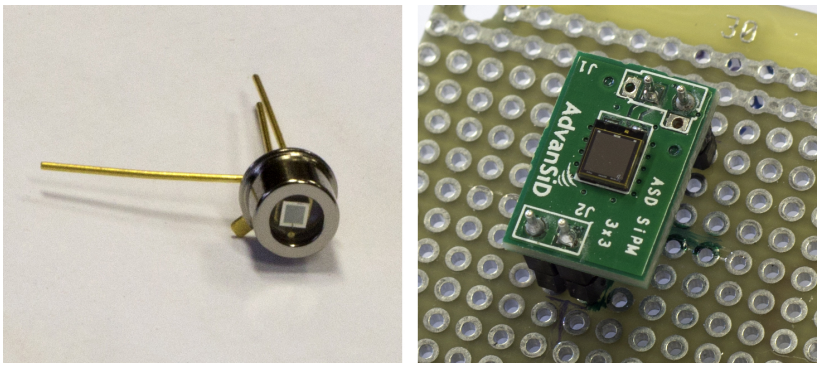

Figure 4: Silicon photomultipliers used for characterization presented in this paper: Hamamatsu S10362–11–050U [11] on the left and FBK AdvanSiD RGB [12] on the right.

3.3. *Measurement results*

In the following sections, characterization measurements are described with their results. At the moment, the experimental setup allows for voltage, surface and incidence angle scans, each described in its own section.

3.3.1. *Operating voltage measurements*

As a first comparison, the two SiPM samples are placed in the chamber at their 0°C operating bias voltages ($V_{OP} = 68.6\,V$ for Hamamatsu and $V_{OP} = 30.0\,V$ for FBK). For each sample, the oscilloscope trace, the charge spectrum (ADC) and the time spectrum (TDC) are recorded. Fig. 5 presents the ADC spectra and signal trace for both SiPMs. The charge spectrum de-

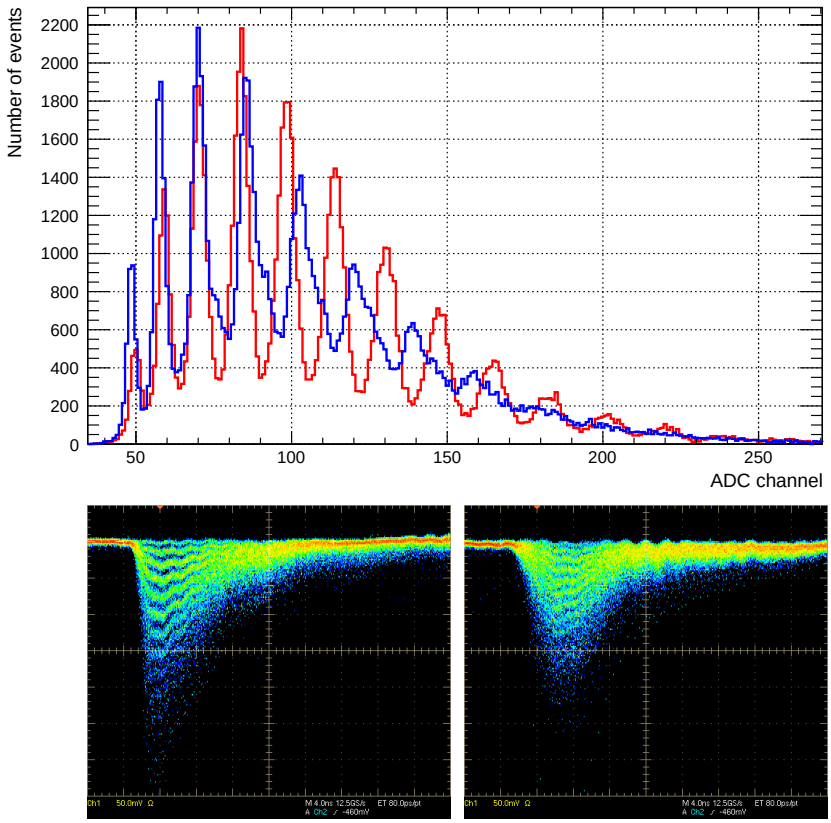

Figure 5: Charge spectra (ADC) for the Hamamatsu (blue) and FBK (red) silicon photomultipliers. The peak structure corresponds directly to the signal trace in the two oscilloscope images (Hamamatsu on the left and FBK on the right).

pends greatly on the amount of photons detected and the different photon

equivalent (p.e.) peaks can be recognized. The first peak on the charge spectrum is known as the pedestal peak and describes the case when no photons are detected. On the other hand, any further peaks are named sequentially as N–th photon equivalent peak (N p.e.), where N gives the proportional number of photons detected. From the charge spectra on Fig. 5, the Hamamatsu SiPM detected 8 photons, while the FBK SiPM detected 10 photons.

3.3.2. Breakdown voltage measurements

The breakdown voltage of a semiconductor is the maximal reverse biased voltage, without causing an exponential increase in current. Once this voltage is exceeded, the electron—hole pairs produced by a photon create a charge carrier cascade inside the semiconductor and exponentially increase the measured current at the terminals. SiPMs can only be used as photodetectors once the bias voltage overcomes its breakdown voltage. However, considerations need to be taken not to increase the applied bias voltage to too high levels, where irreparable damage can occur. Usually this should be kept below 5 V overvoltage (voltage difference between applied and breakdown voltage). For breakdown voltage measurements, a voltage scan in the region around operating voltage was performed for both samples, with bias voltage steps of 0.02 V. The charge spectrum (ADC) was then fitted for peaks using the ROOT data analysis framework [13] and the separation between the first p.e. and second p.e. peaks determined. Peak difference for SiPMs is proportional to their gain G [14]

$$G = \frac{d_{\mathrm{ADC}}\, k_{\mathrm{ADC}}}{q}, \tag{1}$$

where $q = 1.602 \cdot 10^{-19}\,\mathrm{C}$ is the elementary charge, $d_{\mathrm{ADC}}[ADC]$ is the peak separation and $k_{\mathrm{ADC}}[\mathrm{fC}/ADC]$ is the ADC channel conversion factor, depending on the used ADC. Breakdown voltage is therefore determined as the bias voltage, where gain goes to zero. Using a linear fit to the measured voltage scan points, the breakdown voltage for both SiPMs, plotted on Fig. 6 (top row), can simply be determined. This was repeated at temperatures between $0°C$ and $25°C$ (with $5°C$ step size) to check the temperature dependence of breakdown voltage. The temperature dependencies presented on the bottom row of Fig. 6 are $64.92\,\mathrm{mV}/°C \pm 29.34\,\mathrm{mV}/°C$ for Hamamatsu and $28.14\,\mathrm{mV}/°C \pm 9.29\,\mathrm{mV}/°C$ for FBK.

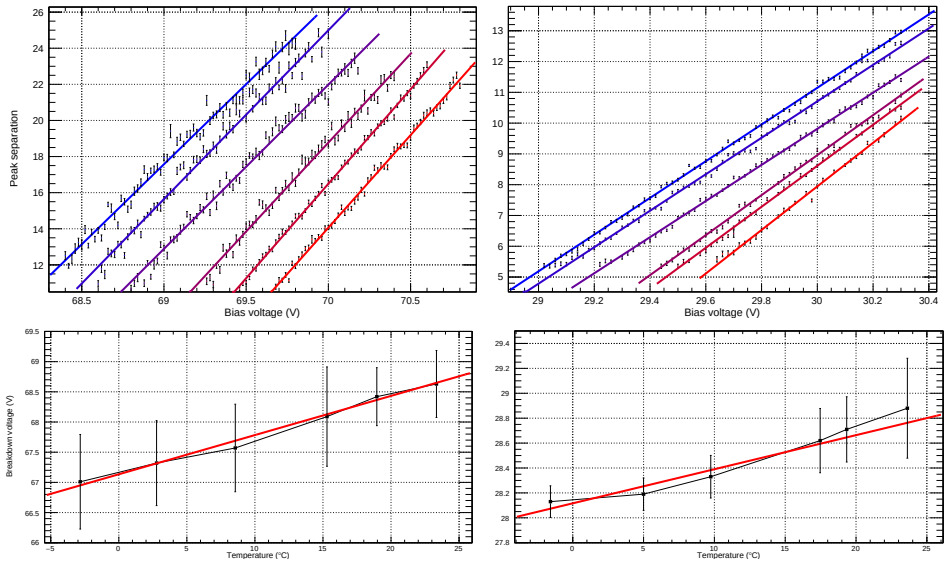

Figure 6: Peak separation versus applied bias voltage at temperatures going from $0°C$ (blue) to $25°C$ (red) with $5°$ steps (top row). Breakdown voltage (determined from linear fits to plots in the top row) versus the chamber temperature (bottom row). The two plots on the left are for the Hamamatsu SiPM, the ones on the right are for the FBK SiPM.

3.3.3. Relative photon detection efficiency measurements

The photon detection efficiency (PDE) is the fraction between the amount of detected photons and the number of photons emitted by the light source. For the purpose of CTA, the typical peak values of SiPM PDE are between 40% and 50% at wavelengths of $\sim$ 400 nm, depending on SiPM construction [15] and manufacturers [8, 9, 10]. Since the experimental setup does not have incident laser light measurement capabilities, an analysis of PDE relative to the incidence angle was performed. Due to reflections on the surface of the SiPM, the number of detected photons decreases with increasing incidence angle.

Relative PDE measurements were performed for the FBK SiPM at room temperature ($\sim 25°$), 30.3 V bias voltage and incidence angles between $0°$ and $75°$ (with $15°$ step size). $0°$ incidence angle corresponds to the perpendicular incidence of laser light onto the surface of the SiPM. With each step, the charge spectrum (ADC) is taken and the relative PDE determined with

$$\mathrm{PDE}(\theta) = \frac{\mu(\theta)}{\mu(0°)} \cdot \frac{1}{\cos(\theta)}, \tag{2}$$

where θ is the incidence angle, $\cos(\theta)$ is a geometrical factor (rotating the sample, a smaller perpendicular surface area is exposed to light source) and μ is the average number of detected photons. μ can be calculated as

$$\mu(\theta) = -\ln\left(\frac{N_{\text{pedestal}}}{N_{\text{total}}}\right), \tag{3}$$

where N_{pedestal} is the number of events in the pedestal peak and N_{total} is the number of all events in the charge spectrum. Both relative PDE and μ are plotted on Fig. 7. The relative PDE in these measurements stays at

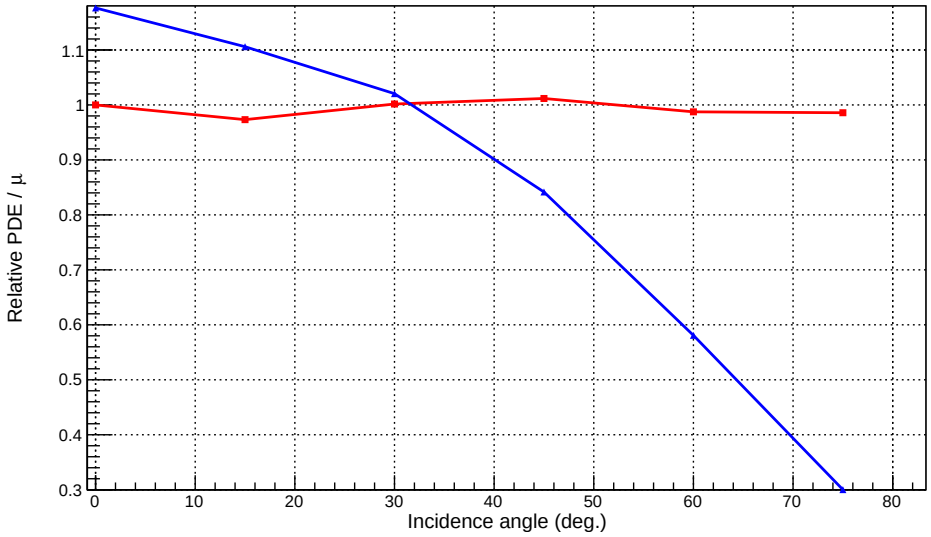

Figure 7: The relative photon detection efficiency (red, from Eq. (2)) and average number of photons μ (blue, from Eq. (3)) versus the incidence angle of laser light. At 0° the laser light is perpendicular to the sample surface. With increased incidence angle, μ decreases due to a geometrical factor (smaller perpendicular surface area).

roughly the value of 1, as expected when compared to work done in [16]. With the use of light guides (Winston cones [17]) that are currently being proposed for the large size telescope of CTA, the incidence angles are kept below $\sim 30°$, where reflection off the surface has almost no effect on PDE.

3.3.4. Surface scan measurements

When a collimator is used for focusing the laser light, it is possible to produce surface scans of SiPMs with the 3-axis movable table. Firstly, to determine the focus of laser optics, one directional scans over the edge

of the sample were made, while adjusting the distance between the optics and sample. The charge spectrum at each measurement point was integrated, resulting in the best approximation of the laser point size of FWHM $\approx 40\,\mu$m. This is about the size of each APD cell on the two samples, so only rough scans were possible with this setup.

The surface scans were performed similarly to determining the focal point, but by moving the laser across the sample surface and keeping the distance between laser optics and sample fixed. Again, an integral of the charge spectrum was calculated for each point and plotted on a contour plot (on Fig. 8). The Hamamatsu sample was measured at bias voltage

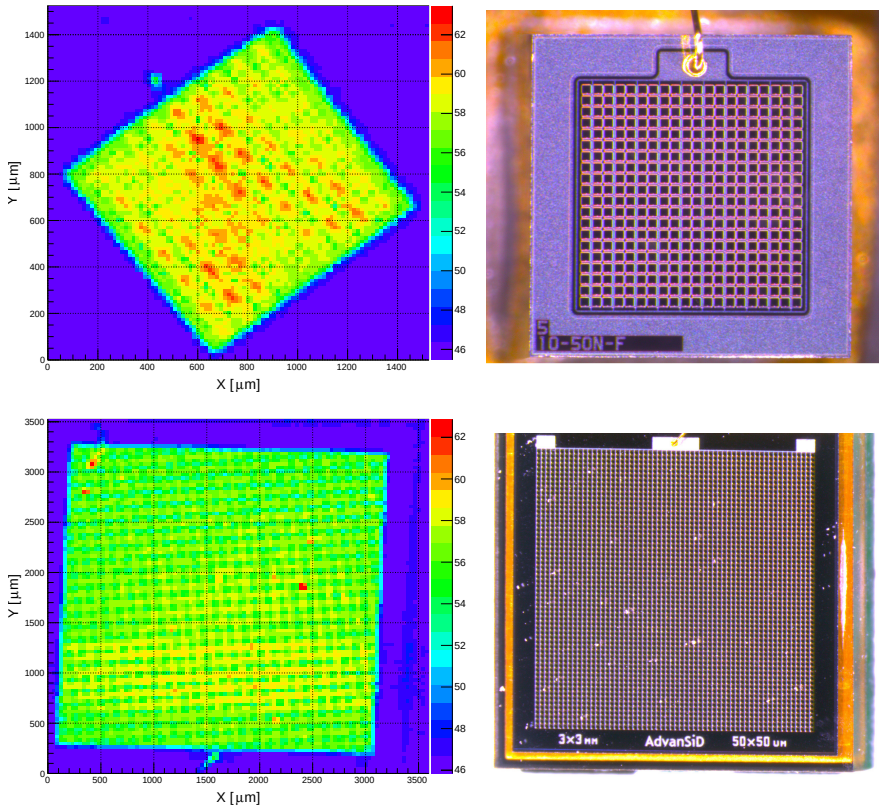

Figure 8: Surface scans of both SiPMs (left side) and their microscope images (right side). The top row is for the Hamamatsu SiPM and the bottom for the FBK SiPM. The Z-axis color scale shows the integral value divided by the number of measured events. Note that reflections on the connecting wire are falsely observed as a signal.

of 69.8 V, while the FBK sample was measured at 30.3 V. Both measure-

ments were performed without monitoring chamber temperature (roughly at room temperature). If more precise surface scans are needed for the large size telescope camera, far more precise laser optics are needed. For this, a Particulars 3D-TCT system [18] at the Jozef Stefan Institute (IJS) can be used, which focuses laser light down to a spot size of $\approx 6\,\mu$m.

4. Conclusions and future directions

From the measurements presented in this paper, a viable conclusion is that silicon photomultipliers have simple photon counting abilities (peaked structure), good sensitivity, high gain, very small bias voltage requirements and a relatively small temperature dependence. They also have good angular efficiency, due to antireflective coatings or antireflective glass on the surface of silicon. However, at this time it is not possible to give preference over conventional photomultipliers, until noise measurements are included in their characterization.

The experimental setup at the Jozef Stefan Institute is able to characterize only a handful of different photodetector characterizations. As future plans, newwer SiPM samples need to be characterized, an upgrade of the experimental setup and additional characterization measurements need to be performed. Both samples used in this work are fairly old (Hamamatsu $<$ 2010, FBK $<$ 2012), so new and improved samples need to be obtained.

At this time, the incidence angle measurements are performed manually by rotating the sample using predetermined 15° steps, that are limited by screw sizes. For the upgraded version, automation with a stepper motor is considered to reduce the step size down to $2.5^\circ - 5^\circ$. Smaller steps are not needed, since the relative PDE does not change drastically over the measured range. As a second upgrade to the setup, a sample holder for camera pixels that will be used for CTA (as a starting point, the MAGIC camera pixel configuration will be used) will be prepared. Since each pixel will be constructed from several SiPMs, some signal summation and shaping methods will have to be implemented to reduce the number of readout channels.

The additional characterization mostly concern noise measurements, since this is the most notable drawback for SiPMs. The scope, not used with current measurements, and TDC spectrum will be used for determining:

- dark count (thermally induced detector noise, when no light falls on the detector),

- cross–talk (detection of photons in a cell, which were produced in neighboring cells),
- afterpulsing (pulses produced by charge carriers trapped in semiconductor impurities and released with a time delay).

Additionally, the laser head will be exchanged to produce characterization results at a much more suitable (for CTA) wavelength in the ultra–violet or blue wavelength range.

References

[1] Cherenkov Telescope Array, `https://www.cta-observatory.org/`, (accessed in May, 2015).

[2] CTA Consortium, *Design concepts for the Cherenkov telescope array CTA*, `arXiv:1008.3703`.

[3] H.E.S.S., `http://www.mpi-hd.mpg.de/hfm/HESS/`, (accessed in May, 2015).

[4] MAGIC, `https://wwwmagic.mpp.mpg.de/`, (accessed in May, 2015).

[5] VERITAS, `http://veritas.sao.arizona.edu/`, (accessed in May, 2015).

[6] Introduction to the SPM, `http://www.sensl.com/downloads/ds/TN%20-%20Intro%20to%20SPM%20Tech.pdf`, (accessed in May, 2015).

[7] F. Dazzi, et al., *D204.8: LST Technical Design Report*, internal CTA sharepoint, (31.10.2014).

[8] Hamamatsu photonics, `http://www.hamamatsu.com/us/en/product/category/3100/4004/index.html`, (accessed in May, 2015).

[9] SensL, `http://sensl.com/products/silicon-photomultipliers/`, (accessed in May, 2015).

[10] FBK, `https://srs.fbk.eu/taxonomy/term/1`, (accessed in May, 2015).

[11] Hamamatsu S10362–11 datasheet, `http://www.phys.hawaii.edu/~idlab/taskAndSchedule/iTOP/SciFi_doco/s10362-11series_kapd1022e05.pdf`, (accessed in May, 2015).

[12] FBK, AdvanSiD RGB SiPM datasheet, http://advansid.com/attachment/get/up_53_1432741078.pdf, (accessed in June, 2015).

[13] ROOT data analysis framework, https://root.cern.ch/, (accessed in May, 2015).

[14] CAEN SiPM characterization, *SiPM characterization*, http://www1.caen.it/xtra/newsletter/2011_04_04/AN2502_SiPM_Characterization.pdf, application note AN2502, (accessed in May, 2015).

[15] S.K. Yang et al., *Precision measurement of the photon detection efficiency of silicon photomultipliers using two integrating spheres*, Optics Express 22, Issue 1 (2014) 716 – 726.

[16] D. Wilson, *Angular dependence of the relative photon detection efficiency of silicon photomultipliers*, Bachelor thesis, September 2012, http://web.physik.rwth-aachen.de/~hebbeker/theses/wilson_bachelor.pdf (accessed in June 2015).

[17] Winston cone, http://scienceworld.wolfram.com/physics/WinstonCone.html (accessed in June 2015).

[18] Particulars advanced measurement systems, http://particulars.si/products.php (accessed in June 2015).

Simulation of micro-nozzle flows with the blob based method of fundamental solutions

Rizwan Zahoor

University of Nova Gorica, Vipavska 13, SI-5000 Nova Gorica

Abstract

A novel numerical technique is presented to compute the Stokes flow when boundaries are immersed. The method is based on the smoothing of forces that leads to the regularization of Stokes fundamental solution which is non singular at the source points. The resulting expressions are stated in terms of forces and can be inverted to calculate the forces driving the flow. The method eliminates the requirement of artificial boundaries compared with conventional method of fundamental solutions.

Keywords: Flow focusing, Stokes flow, Fundamental solution

1. Introduction

Understanding the fundamentals of liquid streams issued from micro-nozzles is vital for various applications in industry, technology and medicine (e.g. combustion, agriculture, surface finish, drug delivery, atomic spectrometry). The production of thin, long and stable fluid jets is necessary in every aerosol production process. Production of micro jets is steadily achieved in the laminar flow regime when sufficient energy is injected into system to overcome the resistance offered by the surface tension and viscosity at the fluid–fluid interface. The recent advent of hard x-ray free electron lasers is allowing for new insights into the atomic structure of matter through methods like serial femtosecond crystallography (SFX). The full intensity of this bright source is necessary for sufficient signal from weakly scattering samples, like membrane protein crystals. In the process, the sample is destroyed by the X-ray pulse, but not before a diffraction pattern is collected. Such diffraction-before-destruction experiments have driven innovation in experiment design and sample delivery. The nozzle characteristics in terms of liquid crystal sample delivery is very important. However, to date little is known about how the nozzle geometry determines jet stability. The results of femtosecond crystallography are widely dependent upon jet characteristics of sample which can be controlled by nozzle parameters [1]. The capillary jets are natural precursors of drops, bubbles and emulsions used in various technological applications. They are produced by focusing of a fluid by another co-flowing

Email address: rizwan.zahoor@ung.si (Rizwan Zahoor)

immiscible lower viscosity fluid [2]. The success of fluid focusing technique lies in the existence of a robust steady jetting regime over wide operating conditions and ready control of jet features through operational parameters [3, 4]. Control of input parameters (liquid flow rate and pressure drop) predicts the behavior of focused liquid at exit (jetting/dripping) [5, 6, 6, 7, 8]. Ganan-Calvo studied the behaviour of focused fluid at different Reynolds numbers [5]. Herrada and Ganan-Calvo performed stability analysis on the gas focused jets [9]. Experiments on atomization of viscous and non-Newtonian liquids by a coaxial, high-speed gas jet and droplet size modelling was performed by Aliseda along with his coworkers [10]. Jet characteristics (stability, growth and breakup etc.) at the nozzle exit were experimentally investigated in [11, 12, 13, 14]. However, to date most of the work is performed experimentally and little is known how the system inflow parameters control the behaviour of the jet at outlet. Current work encompasses the formulation of a computational model to provide enhanced understanding of gas focused flow of liquid in a micro-nozzle. It will present a novel meshless method to solve the problem in order to predict the liquid jet shape (diameter and length) as a function of geometry, material properties and operating conditions. The conventional numerical methods (FEM, FDM, FVM) use full domain meshing of the geometry to solve flow that requires considerable amount of time and care in mesh generation. To capture the more realistic and better results, more refined meshing is required at the nozzle outlet, so more time is required to perform calculation over the full domain. A considerable amount of work has been done in mesh reduction methods that helps reducing meshing efforts and calculation time. The method of fundamental solutions (MFS) also called the F-Trefftz method, charge simulation method, or singularity method) [15] is a numerical technique that belongs to the class of methods generally called boundary element methods (BEM). These methods are best applicable in situations where a fundamental solution of the partial differential equation in question is known. In such cases, the dimensionality of the discretization is reduced. The BEM, for example, requires polygonisation of the boundary surfaces in general three-dimensional (3D) cases, and boundary curves in general 2D cases. This method requires the solution of complicated regular, weakly singular, strongly singular, and hyper singular integrals over boundary segments. This is usually a cumbersome and non–trivial task. The classical MFS is singular at the source point which requires special treatment to avoid singularity. Different approaches have been used so far to avoid this source point singularity. Chen introduced the artificial boundary outside the original boundary to avoid the source point singularity [15]. Any flow where length scale is short and Reynolds number is very low can be modeled as stokes flows. Stokes equation are linear and their fundamental solution exists. A novel meshless technique for the problem of stokes flow using blob based MFS will be explored where flow is driven by external forces. This scheme admits the idea based on conventional MFS, but is preferred because of its non singular behaviour at the source points, thus eliminating the requirement of artificial boundary.

2. Problem formulation

Considering the steady laminar flow, Navier-Stokes equation can be simplified to Stokes equations after linearizing the non linear convective terms. The main features of the nozzle flow including shape and length of jet can be analyzed using Stokes flow. Stokes equation can efficiently handle the problem where the length scale is very small and Reynolds number is low $Re >> 1$. Many sensitivity studies were carried out that provide confidence using stokes flow for subject problem. Stokes flow has no dependency on time other than through time-dependent boundary conditions. This means that, given the boundary conditions of a Stokes flow, the flow can be found without considering time dependency. Eq. 1 is obtained after linearizing the Navier–Stokes equations considering the steady state laminar flow where length scale and $Re >> 1$. It can be solved along with Eq. 2.

$$\mu \Delta \mathbf{v} = \nabla p - \mathbf{f} \tag{1}$$

$$\nabla \cdot \mathbf{v} = 0 \tag{2}$$

where μ, $\mathbf{v}$ and $\mathbf{f}$ represents viscosity, velocity and the force.
The fundamental solution of Stokes equation represents the solution due to concentrated force at the origin and boundary conditions vanishing at infinity. Due to singular behaviour of fundamental solution at the source point a novel approximate fundamental solution method is adapted, where forces are spread over a small region represented by smooth blob functions, instead of using concentrated point forces.

$$\mathbf{f(p)} = f\phi_\epsilon(\mathbf{p}, s) \tag{3}$$

where blob ϕ is a radially symmetric smooth function with parameter ϵ, that represents the force spreading over a 2D domain Ω. It has the following property,

$$\int_\Omega \phi_\epsilon d\Omega = 1. \tag{4}$$

A typical example of a 2D blob is

$$\phi_\epsilon(\mathbf{p}) = \frac{3\epsilon^3}{2\pi}(r^2 + \epsilon^2)^{-5/2}, \tag{5}$$

where

$$r = \left[(p_x - s_x)^2 + (p_y - s_y)^2\right]^{\frac{1}{2}}. \tag{6}$$

The blob function is plotted in Figure 1 for different values of the shape function parameter ϵ. Solution of Eq. 1 and Eq. 2, where force is represented by Eq. 3 can be calculated using the following Green's function approach,
let $\hat{\hat{\phi}}$ be the solution of $\Delta\hat{\hat{\phi}} = \hat{\phi}$
let $\hat{\phi}$ be the solution of $\Delta\hat{\phi} = \phi$.

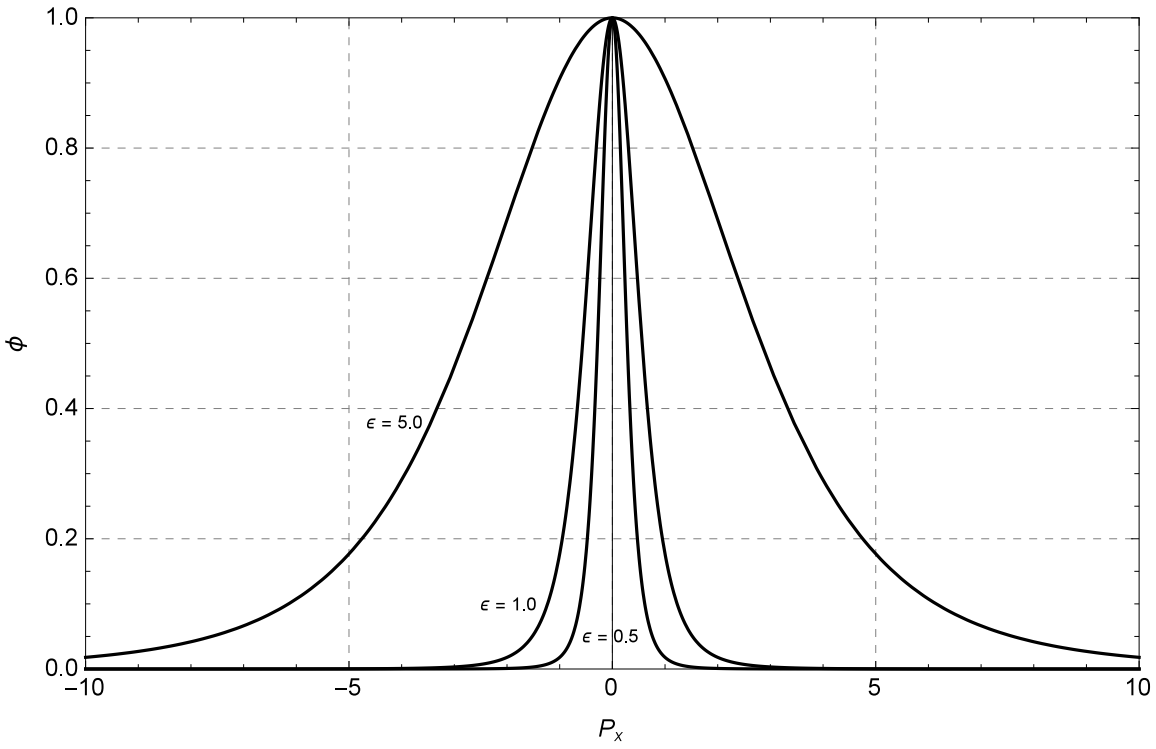

Figure 1: 2D blob function for shape parameter values of $\epsilon = 0.5$, $\epsilon = 1.0$, $\epsilon = 5.0$

3. Solution procedure

The blob based fundamental solution approach is used to construct the solution of Stokes flow in case the force is spread over a smooth region and not concentrated on a point. Taking the divergence of Eq. 1 and using Eq. 2 pressure can be found as

$$P(\mathbf{p}) = \mathbf{f} \cdot \nabla \hat{\phi}_\epsilon(\mathbf{p}, \mathbf{s}). \tag{7}$$

Now using the value of pressure, velocity can be calculated from the momentum conservation equation,

$$\mathbf{v}_n(\mathbf{p}) = \frac{1}{\mu} \left[(\mathbf{f}_n \cdot \nabla) \nabla \hat{\hat{\phi}}_\epsilon(\mathbf{p}, \mathbf{s}_n) - \mathbf{f}_n \hat{\phi}_\epsilon(\mathbf{p}, \mathbf{s}_n) \right]. \tag{8}$$

$\hat{\phi}$ and $\hat{\hat{\phi}}$ can easily be calculated using the following equations,

$$\hat{\phi}_\epsilon = \int \frac{1}{r} \left[\int r \phi_\epsilon(r) dr \right] dr + C_1 \log(r) + C_2, \tag{9}$$

$$\hat{\hat{\phi}}_\epsilon = \int \frac{1}{r} \left[\int r \hat{\phi}_\epsilon(r) dr \right] dr + C_3 \log(r) + C_4. \tag{10}$$

C_1, C_2, C_3 and C_4 are the integration constants, that can be set arbitrarily so that the equation can be written in simplified form. Once $\mathbf{v}_n$ in known, velocity at the field points can be calculated using

$$\mathbf{v}(\mathbf{p}) = \sum_{n=1}^{N} \mathbf{v}_n(\mathbf{p}) = \sum_{n=1}^{N} \frac{1}{\mu} \left[(\mathbf{f}_n \cdot \nabla) \nabla \hat{\hat{\phi}}_\epsilon(\mathbf{p}, \mathbf{s}_n) - \mathbf{f}_n \hat{\phi}_\epsilon(\mathbf{p}, \mathbf{s}_n) \right]. \tag{11}$$

3.1. Finding forces from velocity calculation

The numerical method derived so far, is used to find the velocity in the domain, when the forces driving the flow are know. In some cases when the velocity is known and it is required to find the forces that causes the flow. Eq. 11 can be used to impose the velocity boundary conditions. It is then simple to write from $i = 1, 2, --N$ the system of equations that can be formulated as

$$\mathbf{v}(\mathbf{p}_i) = \sum_{j=1}^{N} A_{ij} f_j, \tag{12}$$

or a matrix equation

$$\mathbf{Ax = b}, \tag{13}$$

where **A** is square matrix which represents the velocity at field points, **b** is a vector obtained from the boundary conditions and **x** is the required vector of forces. With the imposition of proper boundary condition in the right hand side matrix **b** and evaluating the **A** matrix on the left **x** vector can be easily calculated.

4. Results

Figure 2 shows the typical nozzle arrangement, where water and helium are used as focused and focusing fluids, respectively. Behaviour of the jet is largely dependent upon the liquid and gas inlet parameters. Surface tension also plays an important role in the development of liquid jets, because for higher surface tensions, more energy is required in the system to overcome the resistance at the liquid–gas interface.

5. Conclusions

Numerical technique introduced to calculate the force driven Stokes flow. The real fundamental solution is recoverable at the limit, when spreading/shape factor (ϵ) approaches zero. It is well established to deal with Dirichlect and Neumann boundary conditions. Only steady state model is solved so far, so this method can not track the generation of droplets. Sensitivity studies were carried out for convergence of the numerical method and it was found that method converges comparatively faster for large values of force spreading parameter but it is less accurate. Accuracy can be increased by introducing small values of shape parameter. The sensitivity of the results were comprehensively studied over a range of shape parameter values and found that the results were no more sensitive, when discretization length and shape function were proportional.

Figure 2: Development of liquid jet in typical 2D flow focusing nozzle arrangement, water is being focused by Helium gas as a focusing medium

References

[1] H. N. Chapman, *et al.*, *Femtosecond X-ray protein nanocrystallography*, Nature. Rev. 470, 73-77 (2011).

[2] O. A. Basaran, *Small scale free surface flows with breakup: Drop formation and emerging applications*, AIChE Journal. Rev. 48, 1842-1848 (2002).

[3] A. J. Acero, *et al.*, *A new flow focusing technique to produce very thin jets*, Journal of Micromechanics and Microengineering. Rev. 23, 065009 (2013).

[4] A. J. Acero, *et al.*, *Focusing liquid microjets with nozzles*, Journal of Micromechanics and Microengineering. Rev. 22, 065011 (2012).

[5] A. M. Ganan–Calvo, *Generation of steady liquid microthreads and micron-sized monodisperse sprays in gas streams*, Physical Review Letters. Rev. 80, 285 (1998).

[6] A. M. Ganan–Calvo, C. Ferrera and J. M. Montanero, *Universal size and shape of viscous capillary jets: application to gas–focused micro jets*, Journal of Fluid Mechanics. Rev. 670, 427-438 (2011).

[7] A. M. Ganan–Calvo, C. Ferrera, *et al.*, *Experimental and numerical study of the recirculation flow inside a liquid meniscus focused by air*, Microfluidics and nanofluidics. Rev. 11, 65-74 (2011).

[8] A. M. Ganan–Calvo, *Jetting–dripping transition of a liquid jet in a lower viscosity co-flowing immiscible liquid: the minimum flow rate in flow focusing*, Journal of Fluid Mechanics. Rev. 553, 75-84 (2006).

[9] M. A. Herrada, A. M. Ganan–Calvo and P. Guillot, *Spatiotemporal instability of a confined capillary jet*, Physical Review Letters. Rev. 78, 046312 (2008).

[10] A. Aliseda *et al.*, *Atomization of viscous and non-Newtonian liquids by a coaxial, high-speed gas jet: Experiments and droplet size modelling*, International Journal of Multiphase Flow. Rev. 34, 161-175 (2008).

[11] J. B. Keller, S. I. Rubinow and Y. O. Tu, *Spatial instability of a jet*, Physics of Fluids. Rev. 16, 2052-2055 (1973).

[12] S. J. Leib and M. E. Goldstein, *Convective and absolute instability of a viscous liquid jet*, Physics of Fluids. Rev. 29, 952-954 (1986).
[13] J. M. Montanero, M. N. Rebollo, M. A. Herrada and A. M. Ganan–Calvo, *Global stability of the focusing effect of fluid jet flows*, Physical Review Letters. Rev. 83, 036309 (2011).
[14] T. Si, F. Li, *et al.*, *Modes in flow focusing and instability of coaxial liquidgas jets*, Journal of Fluid Mechanics. Rev. 629, 1-23 (2009).
[15] MA. Golberg and CS. Chen, *Discrete projection methods for integral equations*, Computational mechanics publications. (1997).

Simulation of micro-nozzles flow with the phase-field method

Nazia Talat

Laboratory of Multiphase Processes, University of Nova Gorica, Vipavska 13, SI-5000 Nova Gorica

Abstract

Numerical simulation of gas-liquid two phase flow in micro-nozzle is carried out. The focus is laid upon the dynamics of jetting-to-dripping transition of a flow-focused liquid jet surrounded by a co-flowing immiscible, lower viscosity liquid (gas). An axisymmetric two-dimensional flow is assumed. The phase field method is employed to capture the interface. The mechanism is that the interface is driven by the diffusion of chemical potential. The flow is based on unsteady incompressible Navier-Stokes equations coupled with Cahn-Hilliard equation. A novel meshless method "local radial basis function collocation method" is used to solve coupled mass, momentum and Cahn-Hilliard equation with explicit time stepping. The fractional step method is used to couple the pressure and velocity fields. Results are obtained and presented for different flow rates.

Keywords: Dripping-jetting transition, phase field method, Incompressible Navier-Stokes Cahn-Hilliard equations, local radial basis function collocation method

1. Introduction

The controlled production of micro jets is of great interest in various fields such as pharmacy, biotechnology and the food and agriculture industry [1, 2]. Microjets are the natural antecedent of the drops, bubbles, emulsions and capsules used in various technological applications [3]. They are produced in laminar regime by injecting sufficient energy into the system to overcome the surface tension and viscosity. Impulsive growth of waves on the interface gives rise to the jet pinching, producing fluid shapes

Email address: nazia.talat@ung.si (Nazia Talat)

whose morphology mainly depends on the jet features. Microjet production techniques satisfy the existence of a robust steady jetting regime stable over a wide range of experimental conditions and control of jet features through the operational parameters. A force generated by a co-flowing stream stretches a fluid meniscus until a thin fluid ligament is emitted. Generally, two driving forces are used to expel the fluid jet: the viscous drag force exerted by an external liquid (water) and the suction force caused by the pressure drop induced by a co-flowing fluid (gas) stream. Flow focusing (FF) is a technology whose aim is the production of drops or bubbles at a constant rate. It has developed as a research area since the experimental observation that a funnel shaped lens forms when a flowing gas creates shearing forces on a liquid forcing a pressure drop across an orifice. The liquid is defined as the core fluid and the gas is the non-core fluid. The core fluid (water) proceeds through the lens and forms a jet. This relatively new discovery allows for the production of droplets of the liquid on the scale of micrometers. The flow focusing technique [4] in formation of jetting mode uses the pressure gradient exerted by the outer gas stream to focus a steady liquid meniscus from whose tip a microjet is emitted. Both the liquid microjet and the co-flowing gas stream pass through an orifice whose diameter is much larger than that of the microjet. The jet size depends upon the liquid flow rate and the pressure drop. This technique uses hydrodynamic means to produce monodisperse collection of micro-meter drops at a continuous rate [4]. The flow focusing gives the emulsions and micro capsules if the axisymmetric gas stream is replaced with co-flowing liquid [5]. High speed stable drawing of polymer fibers is obtained by focusing highly viscous jets with this co-flowing arrangement [6]. Flow focusing (FF) technique uses another fluid flow, either gas or liquid. This fluid is injected through a small orifice hole which is aligned with the capillary fluid. The gas dynamics forces produced by the gas exiting the orifice deform the fluid surface from the capillary and create a highly focused jet. Flow-focusing phenomenon in a micrometer nozzle by examining both the stability of the steady jetting regime and the size of the emitted jets is experimentally analyzed in [7].

In this paper, we analyzed numerically flow-focusing phenomenon in a micrometer nozzle for the calculation of jetting-dripping transitions of a flow-focused liquid jet surrounded by a co-flowing immiscible, lower viscosity liquid. The mathematical model, coupled Navier-Stokes equations and Cahn-Hilliard equation is described in section 2. In section 3 solution procedure is described. Finally, the paper ends up with some results and conclusions in section 4.

2. Problem Formulation

2.1. Governing Equations

An isothermal liquid-gas two phase flow is considered (Fig.1) by assuming that the gas and liquid are immiscible and incompressible and phase change does not occur. Phase field method is used to capture the interface, which replaces a sharp interface by a thin but nonzero thickness transition region. The phase field function $\phi(\mathbf{x}, t)$ assumes distinct constant values in each bulk phase and undergoes rapid but smooth variation in the interfacial region. It is used to identify the liquid and gas phase at any time t by the following relation

$$\phi(\mathbf{x}, t) = \begin{cases} 1 & \text{for } \textit{liquid} \\ -1 & \text{for } \textit{gas}. \end{cases}$$

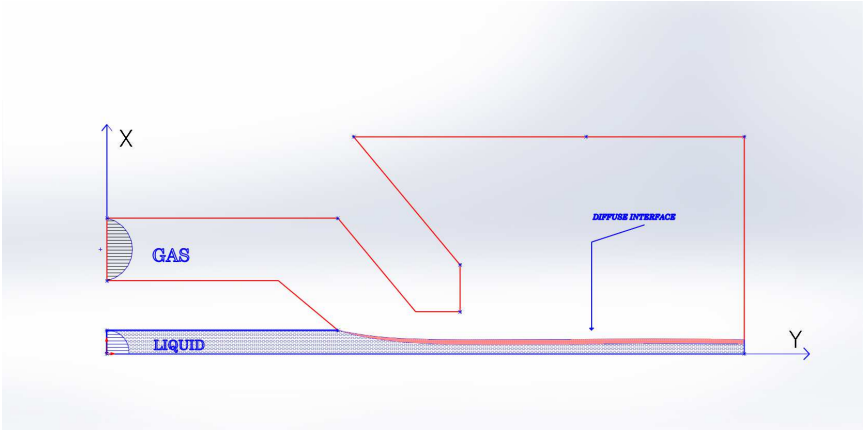

Figure 1: Simulated fluid flow domains.

We have used the Phase field model [8] which uses the familiar Ginzburg-Landau form of elastic (mixing) energy for the interaction between the two fluids

$$W(\phi, \nabla\phi) = \lambda \int_V \left(\frac{1}{2} |\nabla\phi|^2 + F(\phi) \right) dV, \tag{1}$$

where

$$F(\phi) = \frac{1}{4\eta^2}(\phi^2 - 1)^2,$$

is a usual double-well potential of the bulk energy with η is the capillary width (width of the mixing layer). The evolution of ϕ is governed by the Cahn-Hilliard convective-diffusion equation:

$$\frac{\partial \phi}{\partial t} + (\mathbf{u} \cdot \nabla)\phi = \gamma \triangle \omega, \tag{2}$$

where

$$\omega = \frac{\partial W}{\partial \phi} = -(\triangle \phi - f(\phi)).$$

Here $\mathbf{u}$, $\frac{\partial W}{\partial \phi}$ is the variation of energy W with respect to ϕ known as chemical potential and $f(\phi)$ is a polynomial of ϕ such that

$$f(\phi) = F^{'}(\phi) = \frac{1}{\eta^2}\phi(\phi^2 - 1),$$

and γ represents the elastic relaxation time of the system. In [9, 10] it was proven that as $\gamma, \eta \to 0$, the phase equation will approach to the following transport equation:

$$\frac{\partial \phi}{\partial t} + (\mathbf{u} \cdot \nabla)\phi = 0. \tag{3}$$

As Eq.(2) converges to Eq.(3), together with the incompressiblility condition ($\nabla \cdot \mathbf{u}$), the density ρ satisfy the continuity equation:

$$\rho_t + \nabla \cdot (\rho \mathbf{u}) = 0. \tag{4}$$

The momentum equation with variable density and viscosity takes the form

$$\begin{aligned}(\rho(\phi)\mathbf{u})_t + (\mathbf{u} \cdot \nabla)(\rho(\phi)\mathbf{u}) = -\nabla \tilde{p} \quad + \quad & \nabla \cdot (\mu(\phi) D(\mathbf{u})) \\ & - \lambda \nabla \cdot (\nabla \phi \otimes \nabla \phi) + \mathbf{f}, \end{aligned} \tag{5}$$

where ρ is the density of a mixture, $\tilde{p}$ is the pressure, μ is the viscosity and λ corresponds to the surface tension, i.e., $\lambda \sim$ surface tension$\times$ capillary width, $D(\mathbf{u}) = \frac{1}{2}(\nabla \mathbf{u} + (\nabla \mathbf{u})^T)$ and $(\nabla \phi \otimes \nabla \phi)_{ij} = \nabla_{i\phi} \nabla_{j\phi}$ is the usual tensor product. By using the identity

$$\nabla \cdot (\nabla \phi \otimes \nabla \phi) = \nabla \phi \triangle \phi + \frac{1}{2}\Big(\nabla (\nabla \phi)^2\Big),$$

the Eq.5 is further simplified by redefining the pressure term $\tilde{p} = p + \frac{\lambda}{2}|\nabla \phi|^2$. So, for the mixture of two incompressible fluids with variable

density and viscosity the system of equations is as follows:

$$\begin{aligned} \rho_t + \nabla \cdot (\rho \mathbf{u}) = 0, \\ (\rho(\phi)\mathbf{u})_t + (\mathbf{u} \cdot \nabla)(\rho(\phi)\mathbf{u}) + \nabla \tilde{p} - \nabla \cdot (\mu(\phi) D(\mathbf{u})) + \lambda \triangle \phi \nabla \phi = \mathbf{f}, \\ \frac{\partial \phi}{\partial t} + (\mathbf{u} \cdot \nabla)\phi = -\gamma \triangle (\triangle \phi - f(\phi)). \end{aligned} \tag{6}$$

Once the shape and position of interface is calculated, the physical properties of fluids are calculated by averaging those of gas and liquid phases:

$$\rho(\phi) = \frac{2\rho_1\rho_2}{\rho_1(1-\phi) + \rho_2(1+\phi)} \quad \mu(\phi) = \frac{2\mu_1\mu_2}{\mu_1(1-\phi) + \mu_2(1+\phi)}.$$

The coupled non-linear equations will be subjected to the initial conditions

$$\mathbf{u}|_{t=0} = \mathbf{u}_0 \quad \phi|_{t=0} = \phi_0 \quad \omega|_{t=0} = \omega_0.$$

2.2. Boundary Conditions

The conventional no-slip boundary condition is used at the solid wall boundaries. The Hagen- Poiseuille profile $U_l(r) = V_1[1 - (\frac{r}{R_1})^2]$ is defined at the liquid inlet. At the gas inlet, a uniform axial flow, $U_g(r) = V_2$ is imposed. The liquid and gas flow rates can be derived from the inlet velocity field. Zero guage pressure is prescribed at the outlet, which is far from the jet breakup region. At the axis $r = 0$ a symmetry condition $u_r(0, z) = 0, (u_z)_r(0, z) = 0$ is defined.
Boundary conditions are also needed for Cahn-Hilliard equation. By applying the divergence theorem to Eq.2 and integrating it over the whole domain Ω, the first condition for the chemical potential is obtained:

$$\int_\Omega \frac{\partial \phi}{\partial t} dV + \int_{\partial\Omega} (\mathbf{u} \cdot \mathbf{n}) \phi ds = \frac{1}{\gamma} \int_{\partial\Omega} \nabla \omega \cdot \mathbf{n} ds.$$

Under the no-slip boundary condition (*i.e.*, $\mathbf{u} \cdot \mathbf{n} = 0$) and conservation of mass in Ω, $\int_\Omega \frac{\partial \phi}{\partial t} dV = 0$, the chemical potential ω has to satisfy the no-flux boundary conditions, i.e.,

$$\nabla \omega \cdot \mathbf{n} = 0,$$

and the natural boundary condition for the phase field function is

$$\nabla \phi \cdot \mathbf{n} = 0.$$

3. Solution Procedure

For time stepping, explicit Euler method is used. For space discretization, local radial basis function collocation method [11] is used. The detail of local radial basis function collocation method (LRBFCM), used for space discretization is explained in subsection 3.1. For the pressure velocity coupling, the fractional step method (FSM) [12] is used. The solution procedure is structured as follows. First, the intermediate velocity $\mathbf{u}^*$ at $t_0 + \triangle t$ is calculated from the momentum equation without the pressure gradient term

$$\begin{aligned}(\rho(\phi)\mathbf{u})^* &= (\rho(\phi)\mathbf{u})_0 + \triangle t[(-\mathbf{u}\cdot\nabla)(\rho(\phi)\mathbf{u}) + \\ &\quad \nabla\cdot(\mu(\phi)D(\mathbf{u})) - \lambda\nabla\cdot(\nabla\phi\otimes\nabla\phi) + \mathbf{f}]_0. \end{aligned} \tag{7}$$

In this method, the velocity components are corrected by the pressure gradient. The pressure gradient ,i.e. the pressure correction is calculated from the Poisson's equation

$$\nabla^2 p = \frac{1}{\triangle t}\nabla\cdot(\rho(\phi)\mathbf{u})^*, \tag{8}$$

with Neumann boundary conditions

$$\frac{\partial p}{\partial \mathbf{n}} = 0.$$

Finally, the velocity and pressure are updated as

$$(\rho(\phi)\mathbf{u}) = (\rho(\phi)\mathbf{u})^* - \triangle t\nabla p, \tag{9}$$

and solution is ready for the next step.

3.1. Local Radial Basis Function of Collocation Method

In the LRBFCM, a set of radial basis functions (RBFs) and collocation is used to solve the governing equations. The method is implemented locally on a set of neighbouring nodes, which can be uniformly or non-uniformly distributed over the whole domain (Fig.2). The whole computational domain consists of N nodes, of which there are N_Ω domain and N_Γ boundary nodes. It is divided into N subdomains, each of which consists of ${}_lN$ nodes ${}_lp_n$, where $l = 1, ..., N$ and $n = 1, ...,{}_l N$ is the number of nodes in each subdomain (Fig.3).

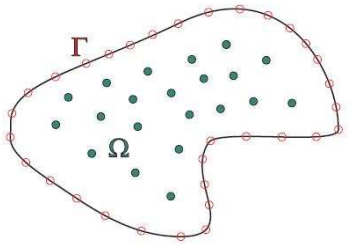

Figure 2: Node arrangement for the meshless method. Green full circles: domain nodes. Red empty circles: boundary nodes.

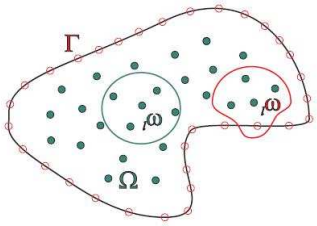

Figure 3: Node arrangement with subdomains. Green full circles: internal nodes. Red empty circles: boundary points.

On each of the N subdomains, the function θ is represented with RBFs as

$$\theta(\mathbf{p}) \approx \sum_{k=1}^{{}_lK} {}_l\psi_k(\mathbf{p}) {}_l\alpha_k, \tag{10}$$

where $\mathbf{p}$ is position vector, ${}_l\psi_k$ are a set of RBFs centered in points ${}_lp_k$, ${}_l\alpha_k$ are the coefficients and ${}_lK$ is the number of shape functions. In the present paper, five-noded subdomains are used and LRBFCM is implemented with multiquadratic (MQ) RBF shape functions. In order to determine the coefficients, the collocation

$$\theta({}_l\mathbf{p}_n) =_l \theta_n = \sum_{k=1}^{{}_lK} {}_l\psi_k({}_l\mathbf{p}_n) {}_l\alpha_k, \tag{11}$$

is used. A linear system of ${}_lk$ equations is obtain from Eq.11

$${}_l\mathbf{\Psi}_l\boldsymbol{\alpha} =_l \boldsymbol{\theta}. \tag{12}$$

For the coefficients to be computable, the number of the shape functions has to match the number of the collocation nodes ${}_lK =_l N$, and collocation matrix has to be non-singular. The coefficients can be computed from

$${}_l\boldsymbol{\alpha} =_l \mathbf{\Psi}^{-1}{}_l\boldsymbol{\theta}. \tag{13}$$

By considering the expression for coefficient, the function $\theta(\mathbf{p})$ can be approximately represented as

$$\theta(\mathbf{p}) \approx \sum_{k=1}^{{}_lN} {}_l\psi_k(\mathbf{p}) {}_l \sum_{n=1}^{{}_lN} {}_l\psi_{kn}^{-1}(\mathbf{p}) {}_l\theta_n. \tag{14}$$

We consider two dimensional cartesian coordinates system with base vectors $\mathbf{i}_\zeta$ and coordinates $p_\zeta; \zeta = x, y$, i.e $\mathbf{p} = \mathbf{i}_x p_x + \mathbf{i}_y p_y$. In order to solve the governing equations, the involved derivatives of the function $\theta(\mathbf{p})$ need to be calculated on each subdomain. The first spatial partial derivatives on each of the subdomain are expressed as follows:

$$\frac{\partial}{\partial p_\zeta}\theta(\mathbf{p}) \approx \sum_{k=1}^{{}_lN} \frac{\partial}{\partial p_\zeta} {}_l\psi_k(\mathbf{p})_l \sum_{n=1}^{{}_lN} {}_l\psi_{kn}^{-1}(\mathbf{p})_l\theta_n; \zeta = x, y. \tag{15}$$

Similarly second, third and fourth spatial partial derivatives are:

$$\begin{aligned}
\frac{\partial^2}{\partial p_\zeta^2}\theta(\mathbf{p}) &\approx \sum_{k=1}^{{}_lN} \frac{\partial^2}{\partial p_\zeta^2} {}_l\psi_k(\mathbf{p})_l \sum_{n=1}^{{}_lN} {}_l\psi_{kn}^{-1}(\mathbf{p})_l\theta_n; \zeta, = x, y, \\
\frac{\partial^3}{\partial p_\zeta^3}\theta(\mathbf{p}) &\approx \sum_{k=1}^{{}_lN} \frac{\partial^3}{\partial p_\zeta^3} {}_l\psi_k(\mathbf{p})_l \sum_{n=1}^{{}_lN} {}_l\psi_{kn}^{-1}(\mathbf{p})_l\theta_n; \zeta, = x, y, \\
\frac{\partial^4}{\partial p_\zeta^4}\theta(\mathbf{p}) &\approx \sum_{k=1}^{{}_lN} \frac{\partial^4}{\partial p_\zeta^4} {}_l\psi_k(\mathbf{p})_l \sum_{n=1}^{{}_lN} {}_l\psi_{kn}^{-1}(\mathbf{p})_l\theta_n; \zeta, = x, y.
\end{aligned} \tag{16}$$

The MQ-RBF is defined as:

$${}_l\psi_k(\mathbf{p}) = [{}_lr_k + c^2]^{1/2}; \quad {}_lr_k = (\mathbf{p} -_l \mathbf{P}_k).(\mathbf{p} -_l \mathbf{P}_k),$$

where c represents the free parameter. The explicit values of involved derivatives of ${}_l\psi_k$ are

$$\begin{aligned}
\frac{\partial {}_l\psi_k}{\partial p_x} &= \frac{p_x -_l p_{kx}}{({}_lr_k + c^2)^{1/2}}, \quad \frac{\partial {}_l\psi_k}{\partial p_y} = \frac{p_y -_l p_{ky}}{({}_lr_k + c^2)^{1/2}}, \\
\frac{\partial^2 {}_l\psi_k}{\partial p_x^2} &= \frac{(p_y -_l p_{ky}) + c^2}{({}_lr_k + c^2)^{3/2}}, \quad \frac{\partial^2 {}_l\psi_k}{\partial p_y^2} = \frac{(p_x -_l p_{kx}) + c^2}{({}_lr_k + c^2)^{3/2}}, \\
\frac{\partial^3 {}_l\psi_k}{\partial p_x^3} &= \frac{-3({}_lr_k^2 + c^2)^{1/2}(p_x -_l p_{kx})}{({}_lr_k^2 + c^2)^3}, \\
\frac{\partial^3 {}_l\psi_k}{\partial p_y^3} &= \frac{-3({}_lr_k^2 + c^2)^{1/2}(p_y -_l p_{ky})}{({}_lr_k^2 + c^2)^3},
\end{aligned} \tag{17}$$

and similarly fourth order derivatives are as follows:

$$\begin{aligned}
P_{\text{num}} \quad = \quad & -3[({}_lr_k^2 + c^2)^{1/2} + (p_x -_l p_{kx})({}_lr_k^2 + c^2)^{5/2}] + \\
& 9(p_x -_l p_{kx})^2({}_lr_k^2 + c^2)^{5/2},
\end{aligned}$$

$$P_{\text{denom}} = ({}_l r_k^2 + c^2)^6.$$

$$\frac{\partial^4 {}_l\psi_k}{\partial p_x^4} = \frac{P_{\text{num}}}{P_{\text{denom}}} \tag{18}$$

$$\begin{aligned} P_{\text{num}} &= -3[({}_l r_k^2 + c^2)^{1/2} + (p_y -_l p_{ky})({}_l r_k^2 + c^2)^{5/2}] + \\ & 9(p_x -_l p_{kx})^2({}_l r_k^2 + c^2)^{5/2}, \end{aligned}$$

$$P_{\text{denom}} = ({}_l r_k^2 + c^2)^6.$$

$$\frac{\partial^4 {}_l\psi_k}{\partial p_y^4} = \frac{P_{\text{num}}}{P_{\text{denom}}} \tag{19}$$

In the Fractional step method, the Poisson's equation has to be solved globally, so in this case each local ${}_l\mathbf{p}_n$ coincides with global point $\mathbf{p}_k; k = 1, ..., N$. A relation between the local and global point indices on each of the subdomain is introduced as $\mathbf{p}_{k(l,n)} =_l \mathbf{p}_n$. The pressure is represented on each of the subdomains by RBFs and their coefficients as

$$p(\mathbf{p}) = \sum_{n=1}^{{}_l N} \psi_{k(l,n)}(\mathbf{p}) {}_l\alpha_n; \mathbf{p} \in {}_l\omega. \tag{20}$$

The coefficients ${}_l\alpha_n$ are calculated by collocation

$$p(\mathbf{p}_{k(l,m)}) = \sum_{n=1}^{{}_l N} {}_l\psi_{k(l,n)}(\mathbf{p}_{k(l,m)}) {}_l\alpha_n; \mathbf{p} \in {}_l\omega, m = 1, ...,_l N. \tag{21}$$

The RBFs representation of pressure function on each of the subdomain is as

$$p(\mathbf{p}) = \sum_{n=1}^{{}_l N} {}_l \sum_{m=1}^{{}_l N} {}_l\psi_{k(l,m)}(\mathbf{p}) {}_l\psi^{-1}_{k(l,m)} p_{k(l,m)}. \tag{22}$$

The calculated derivatives are then used to solve the governing equations which represents the solution of the problem.

4. Results and Conclusion

Numerical simulation of gas-liquid two phase flow in micro-nozzle was carried out. A diffuse interface formulation, namely, phase field method was used to capture the interface and also to resolve the singularities arising from the interaction of liquid and gas. There was no explicit tracking of interface. The fractional step method and local radial basis function collocation method was used to discretize the Navier-stokes Cahn-Hilliard system. We showed good agreements with the experimental results.

Acknowledgements

The author is very grateful to the reviewers for their helpful suggestions. The work was supported by Young Researcher programme of the Slovenia.

References

[1] J. Eggers, *Nonlinear dynamics and breakup of free-surface flows*, Rev. Mod. Phys. 69 865-929 (1997).

[2] J. Eggers and Villermaux E, *Physics of liquid jets*, Rep. Prog. Phys. 71 1-79 (2008).

[3] O.A. Basaran , *Small-scale free surface flows with breakup: drop formation and emerging applications*, AlChE J. 48 1842-8 (2002).

[4] A.M. Ganan-Calvo, *Generation of steady liquid microthreads and micron-sized monodisperse sprays in gas streams*, Phys. Rev. Lett. 80 285-8 (1998).

[5] A. M. Ganan-Calvo *et al.*, *Focusing capillary jets close to the continuum limit Nature*, Phys.3 737-42 (2007).

[6] A. M. Ganan-Calvo *et al.*, *Steady high viscosity liquid micro-jet production and fiber spinning using co-flowing gas conformation*, Eur. Phys. J. B 39 131-7 (2004).

[7] A. J. Acero, *et al.*, *Focusing liquid microjets with nozzles*, J. Micromech. Microeng. 22. 065011 (10pp) (2012).

[8] C. Liu, J. Shen, *A phase field model for the mixture of two incompressible fluids and its approximation by a Fourier-spectral method*, Physica D 179: 21128 (2003).

[9] C. Liu, S. Shkoller, *Variational phase field model for the mixture of two fluids*, priprint (2001).

[10] C. Liu, N.J. Walkington, *An Eulerian description of fluids containing visco-hyperelastic particles*, Arch. Rat. Mech. Anal. 159 229252 (2001).

[11] B. Sarler, R. Vertnik, *Meshfree explicit local radial basis function collocation method for diffusion problems*, Computers and Mathematics with Applications. 51, 1269-1282 (2006).
[12] A. Chorin, *Numerical solution of Navier-Stokes equations*, Mathematical Computation. vol.22,pp.745-762 (1968).
[13] R. Vertnik, *Heat and fluid flow Simulation of the continous casting of steel by a meshless method*, (2010).

Implementation of a Quasi-Upwind Scheme in a Diffuse Approximate Method

Vanja Hatič

University of Nova Gorica, Vipavska 13, SI-5000 Nova Gorica

Abstract

Upwind scheme is a method used for solving the convection-diffusion equation. The method is especially needed when solving problems with convection dominated term. In this paper a simple type of an upwind-style calculation is used to solve the transport equation of a one-dimensional convection dominated flow. Meshless methods are used to solve the transport equation. The basic idea is to adopt the upwind principles when calculating weights of meshless methods. In the first part of the paper, the diffuse approximate method type of meshless methods is presented, along with a detailed description of the weighting function. In the second part a simple example case is presented, where the upwind approach is compared to the usual approach and the analytical solution.

Keywords: Upwind, Diffuse approximate method, Convection, Casting simulation

1. Introduction

Meshfree or meshless methods are numerical methods used to build mathematical models, which could also be constructed with traditional methods such as finite difference method or finite volume method. The main difference is that traditional methods require a structured grid of data points, where each point has to be assigned with a number of neighboring points. The defined connections between the neighbor points are used to simulate mathematical operators such as gradient or derivative. On the other hand, one of main benefits of meshless methods is that they do not need a structured grid. Instead an interpolation functional is fitted on the

Email address: vanja.hatic@gmail.com (Vanja Hatič)

unstructured grid. The mathematical operators of the mathematical model can be then applied directly on functionals.

At the Institute of Metals and Technology meshfree methods were used to develop a simulator of direct chill casting [1]. The Low frequency electromagnetic casting simulator uses mass, momentum, energy and species conservation equations to predict temperature, liquid fraction, pressure, concentration, velocity and magnetic force fields at various stages of casting process. Sometimes the process is not fully stable especially in the presence of electromagnetic forces. Fluctuations are caused by the strong convective flow. Therefore a modified meshless version of upwind differencing scheme is proposed, where weights of the diffuse approximation method (DAM) are calculated using "upwind principles".

2. Meshless method approach

Selection of an appropriate interpolation function could be challenging when using a meshfree approach. There are many different options which can be used to determine a suitable approximation of the scattered data, for instance least squares, weighted least squares or moving least squares (MLS) methods. Methods differ from each other by the accuracy and complexity of the implementation. For the approximation of the scattered nodal data in the Low Frequency electro-magnetic casting (LFEMC) simulator, a diffuse approximate method (DAM) is used, which is a method derived from the MLS approximation. DAM is thoroughly described in publications by Sadat and Prax [2, 3, 4].

2.1. Diffuse approximation method

MLS method for interpolation of data is a special case of weighted least squares, where the global computational domain is further divided into local subdomains. Consequently each computational node is assigned with its own domain, where weighted least squares parameters are computed. From this set of local functions a continuously smooth and differentiable global function is obtained. A MLS approximation $\hat{f}(\boldsymbol{x})$ of a function f at a point $\boldsymbol{x}$ of a local domain is defined as:

$$\hat{f}(\boldsymbol{x}) = \sum_{j=1}^{m} p_j(\boldsymbol{x})\alpha_j(\boldsymbol{x}) = \boldsymbol{p}^T(\boldsymbol{x})\boldsymbol{\alpha}(\boldsymbol{x})$$

where $\boldsymbol{p}^T(\boldsymbol{x})$ is the polynomial basis vector of dimensions m and $\boldsymbol{\alpha}(\boldsymbol{x})$ is the vector, containing coefficients $\alpha_j(\boldsymbol{x})$. Two-dimensional quadratic base vector is:

$$\boldsymbol{\alpha}(\boldsymbol{x})^T = \left[f, \frac{\partial f}{\partial x}, \frac{\partial f}{\partial y}, \frac{\partial^2 f}{\partial x^2}, \frac{\partial^2 f}{\partial x \partial y}, \frac{\partial^2 f}{\partial y^2}\right].$$

Coefficients of vector $\boldsymbol{\alpha}$ must be obtained through the minimization of the following statement:

$$J = \sum_{i=1}^{n} \theta(\boldsymbol{x_i}, \boldsymbol{x})[f(\boldsymbol{x_i}) - \boldsymbol{p}^T(\boldsymbol{x_i})\boldsymbol{\alpha}(\boldsymbol{x})]^2 \tag{1}$$

where n is the number of nodes in the reference domain, associated with points $\boldsymbol{x}$ and $\theta(\boldsymbol{x_i}, \boldsymbol{x})$ are the weights correlated with each point in the domain. Determination of the weights will be thoroughly described in section 3 of this paper. With the minimization of equation (1), the following system of equations is obtained:

$$\boldsymbol{A}(\boldsymbol{x})\boldsymbol{\alpha}(\boldsymbol{x}) = \boldsymbol{B}(\boldsymbol{x})\boldsymbol{f}(\boldsymbol{x}) \tag{2}$$

where matrices $\boldsymbol{A}$, $\boldsymbol{B}$ and $\boldsymbol{f}$ are defined as :

$$\boldsymbol{A}(\boldsymbol{x}) = \sum_{i=1}^{n} \theta(\boldsymbol{x}, \boldsymbol{x_i})\boldsymbol{p}(\boldsymbol{x}_i)\boldsymbol{p}^T(\boldsymbol{x_i}),$$

$$\boldsymbol{B}(\boldsymbol{x}) = \sum_{i=1}^{n} \theta(\boldsymbol{x}, \boldsymbol{x_i})\boldsymbol{p}(\boldsymbol{x}_i),$$

$$\boldsymbol{f}(\boldsymbol{x})^T = [f(\boldsymbol{x_1}), f(\boldsymbol{x_2}), ..., f(\boldsymbol{x_n})].$$

Because of the second order differential equation, a two-dimensional polynomial quadratic base was chosen:

$$\boldsymbol{p}^T(\boldsymbol{x_i}, \boldsymbol{x}) = \left[1, (x_i - x), (y_i - y), (x_i - x)(y_i - y), (x_i - x)^2, (y_i - y)^2\right]$$

The system of equations (2) can be reversed as long as the matrix $\boldsymbol{A}(\boldsymbol{x})$ is not singular. Which is true if the total number of points in the neighborhood is bigger or at least equal to the size of vector of coefficients $\boldsymbol{\alpha}(\boldsymbol{x})$. From the reversed system, the solution, a vector of coefficients is obtained:

$$\boldsymbol{\alpha}(\boldsymbol{x}) = \boldsymbol{A^{-1}}(\boldsymbol{x})\boldsymbol{B}(\boldsymbol{x})\boldsymbol{f}(\boldsymbol{x}).$$

3. Weighting function

Various functions such as Gaussian, cubic spline or quadratic spline can be used to calculate least squares weights. The Gauss function has proven to preform well during the calculation of the DAM test cases, therefore it was also used in the LFEMC simulator.

3.1. Central weighting scheme

Equation (3) represents the general form of the Gaussian used to calculate weights:

$$\theta(r) = e^{-\lambda \frac{r^2}{h^2}} \tag{3}$$

where λ is the Gaussian free shaping parameter and must be picked carefully, h is the average dispersion of nodal points in the local neighborhood and depends on the size of the local support. The effect of both h and λ on the shape of the Gaussian can be observed from Figure (1). Parameter r represents the distance between the central node and neighboring data nodes of the subdomain ($r = \boldsymbol{x_i} - \boldsymbol{x}$).

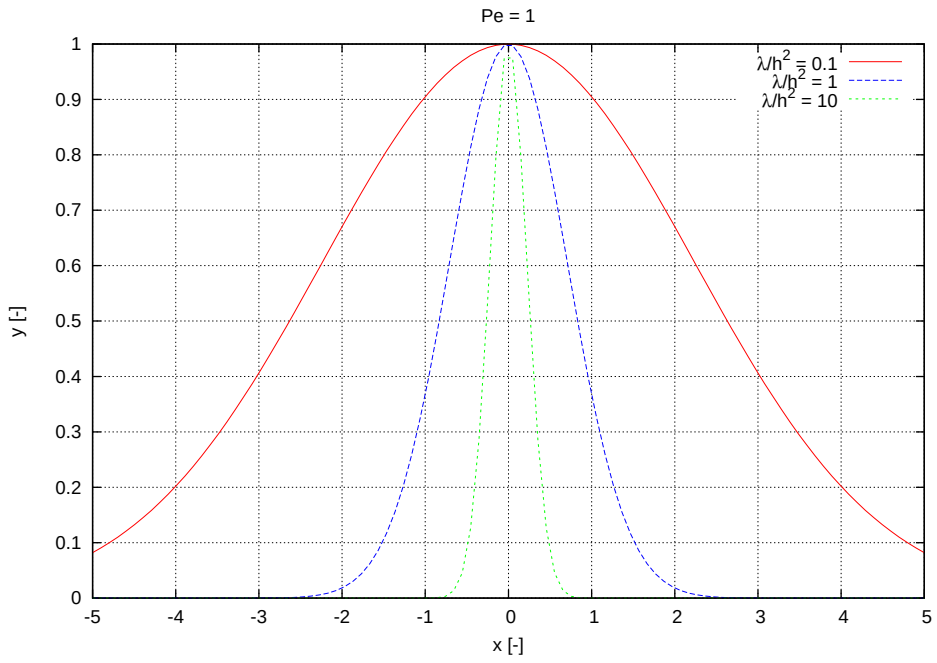

Figure 1: Gaussian functions for different λ/h^2 values are presented. Graph shows that λ/h^2 controls the width of the Gaussian "bell"

It is known that central weighting scheme gives good and stable results when solving conservation equations in cases where the convection term is not dominant. The influence of the convective term on the conservation equation is measured with the dimensionless Péclet number:

$$\mathrm{Pe} = \frac{\ell |\boldsymbol{v}|}{\kappa}$$

where Pe is the Péclet number, ℓ is the characteristic length scale, $|\boldsymbol{v}|$ is the magnitude of velocity and κ is diffusivity. Effect of convection is low for small Pe. On the contrary, for large Pe number (Pe $\gtrapprox$ 20) conservation equation becomes a convection driven problem [5]. Therefore the central weighting scheme becomes unstable, when solving systems with large Péclet numbers. Instabilities are shown in the oscillations of the numerical solution around the target value. A solution to this problem could be in the implementation of the upwind weighting scheme.

3.2. Upwind weighting scheme

The upwind differencing scheme was proposed in the 1950s in order to differentiate the convection term [6]. The main benefit of this method is that it takes into account the flow direction. Therefore the nodes which stand in front of the central node in the velocity direction can be given smaller weight, than those which stand behind it.

In case of meshfree methods, a simple implementation of the upwind procedure would be to adapt the upwind principles when calculating weights. In the terms of DAM this means that the distance in the Gaussian function is not calculated regarding the central node, but regarding an abstract shifted central node. The shift must be preformed in the direction opposite to the velocity direction in order to attain the upwind effect. The weighting function remains the Gaussian:

$$\theta(\tilde{r}) = e^{-\lambda \frac{\tilde{r}^2}{h^2}}$$

where it can be noted that the only modification in comparison with eq. (3) is in the determination of the distance $\tilde{r}$ which now represents the distance between the shifted central node ($\tilde{\boldsymbol{x}}$) and neighboring data nodes of the subdomain ($\tilde{r} = \boldsymbol{x_i} - \tilde{\boldsymbol{x}}$).

The calculation of the central node shift distance magnitude must be proportional to the Péclet number and the subdomain size. As it was proposed by Lin and Atluri [7] it can be calculated by the following equation:

$$\tilde{\boldsymbol{x}} = \boldsymbol{x} - \gamma r_0 \boldsymbol{S}_v$$

where r_0 is the subdomain diameter, $\boldsymbol{S}_v$ the unit vector of the flow velocity direction and γ the coefficient of the domain shift is calculated by:

$$\gamma = \coth \frac{\mathrm{Pe}}{2} - \frac{2}{\mathrm{Pe}}$$

and Péclet number is determined by:

$$\mathrm{Pe} = \frac{v r_0}{D}$$

where v is the magnitude of velocity and D is the diffusivity constant.

4. Numerical example

To test the stability and reliability of the upwind weighting scheme in comparison with the standard central weighting scheme, a simple test case was calculated. A basic conservation equation of a general quantity was solved with an implicit Euler method. The convection-diffusion equation can be written in the following form:

$$\frac{\partial \phi}{\partial t} + \nabla \cdot (\boldsymbol{v}\phi) = \nabla \cdot (D \nabla \phi) + S_C$$

where ϕ is a general scalar quantity, $\boldsymbol{v}$ is the velocity vector field and S_C is the source term. Problem was solved on a square domain with unit sides, where discretisation of a regular rectangular grid was made with eleven points in both x and y direction. Scattered data was approximated with subdomains containing 13 nodal points.

One dimensional case was calculated as a quasi two dimensional case, where all quantities were set to constant in the y direction. Initial conditions were set to $\phi(x = 0) = 1$ and $\phi(x = 1) = 0$. The Neumann boundary conditions were implemented at ”west” and ”east” boundary and isolated conditions at ”north” and ”south” boundary. Diffusivity was constant and set to 0.01 and source term to 0 for all cases. Velocity was also set to constant and steady throughout the whole domain, but it was varied through different cases in order to get different Péclet numbers.

A simplified and 1-dimensional equation can be written in the following form:

$$\frac{\partial \phi}{\partial t} = \frac{\partial^2 \phi}{\partial x^2} - v_x \frac{\partial \phi}{\partial x}$$

where v_x is the velocity magnitude in the x direction. If the unsteady term is set to zero, a second order differential form is attained, for which an exact solution exists. Taking into account boundary conditions the following solution is gained:

$$\phi = \frac{1}{1 - e^{v_x/D}}(e^{v_x x/D} - e^{v_x/D}).$$

5. Results

Test case was calculated for different Péclet numbers and results are given on figures 2 and 3. It is evident that both schemes give good results for cases with Pe numbers of 1 and 10. However the central weighting scheme shows oscillations at higher Pe numbers, which contradicts the analytical results. Yet the upwind scheme is free of these uncertainties.

6. Conclusion

Two possible schemes of local DAM weights calculation were presented in the paper. Both were tested on a simple one dimensional case of transport equation. It was found out that both schemes give similar results for lower Péclet numbers (Pe $\leq$ 20). At higher Péclet numbers the central-based scheme results where unstable. On the contrary the upwind results did not show any oscillations. Nevertheless it should be pointed out that numerical examples were only preformed for a simple 1D case and further evaluations are required. In future work more complicated cases should be studied. Firstly 2D cases should be studied, followed by the implementation of the upwind weighting scheme in a driven cavity case.

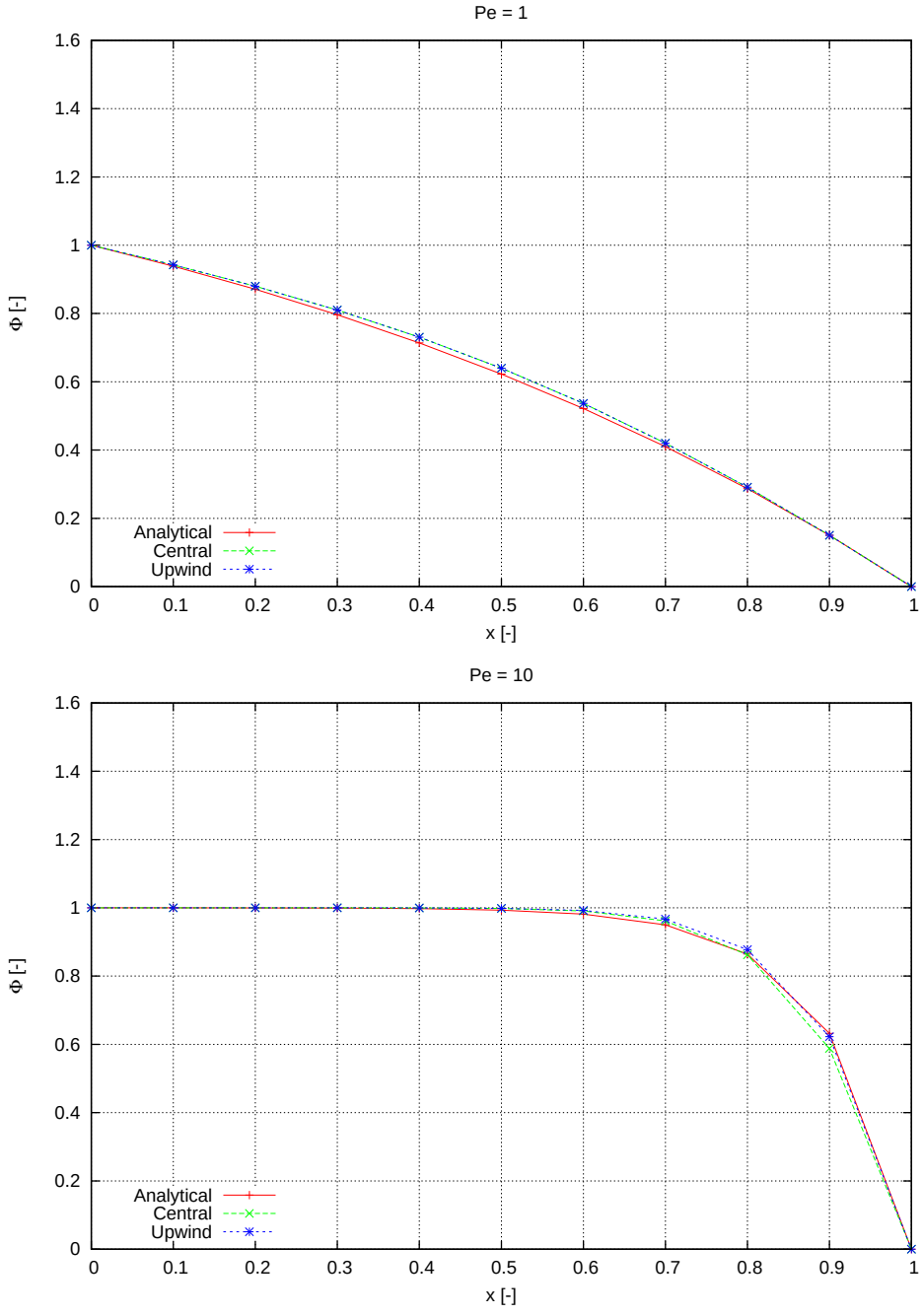

Figure 2: Numerical and analytical results for low Péclet numbers. x denotes the dimensionless distance and ϕ denotes a general dimensionless scalar quantity. Diffusivity D is set to 10^{-2} for both cases. Horizontal velocity is equal to $v_x = 0.01$ for case Pe $= 1$ and to $v_x = 0.1$ for case Pe $= 10$. It is clearly visible that results for central and upwind weighting scheme overlap completely

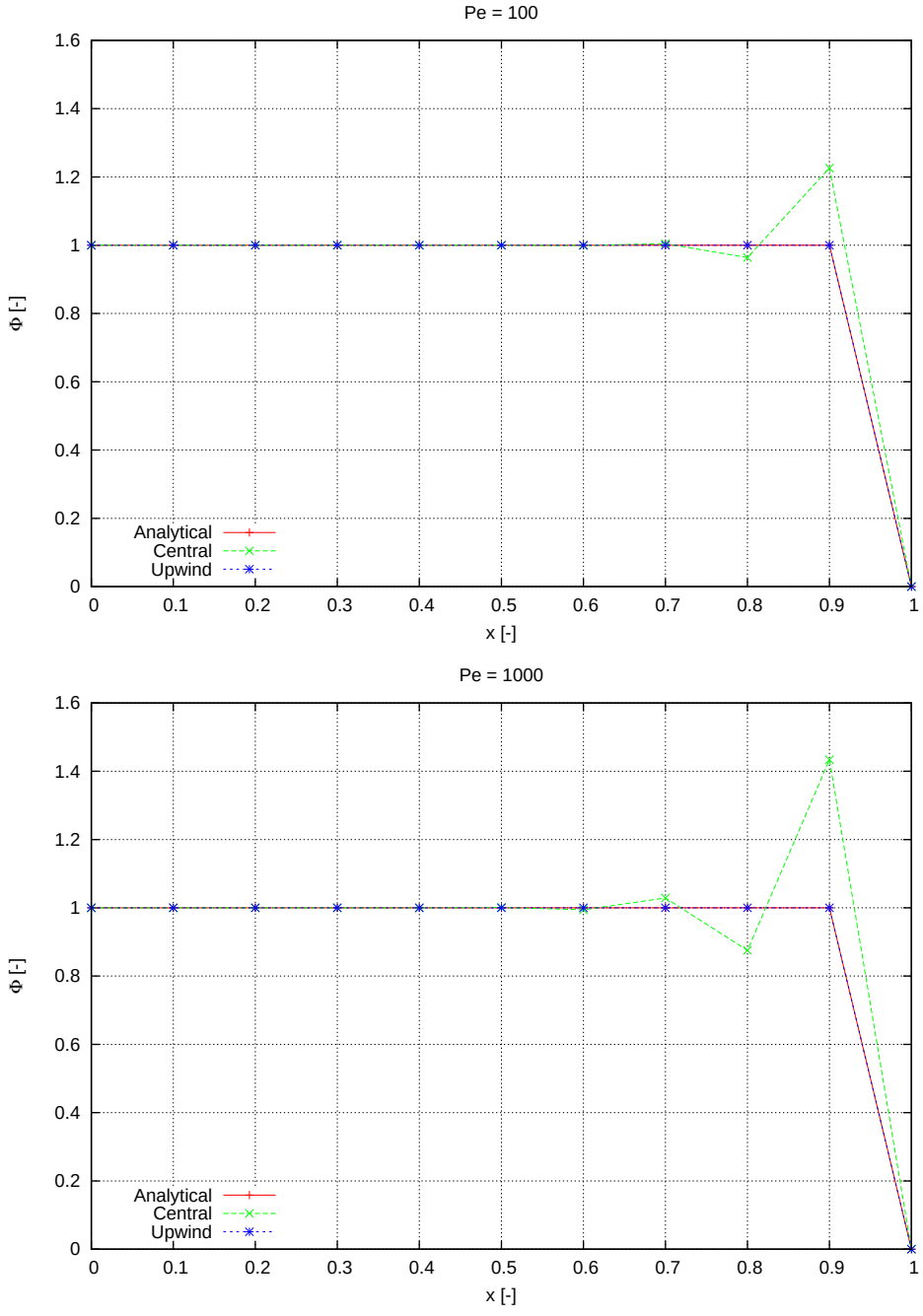

Figure 3: Numerical and analytical results for high Péclet numbers. x denotes the dimensionless distance and ϕ denotes a general dimensionless scalar quantity. Diffusivity D is set to 10^{-2} for both cases. Horizontal velocity is equal to $v_x = 1$ for case Pe $= 100$ and to $v_x = 10$ for case Pe $= 1000$.

References

[1] B. Šarler *et al.*, *Simulation of multiscale inudstrial solidification problem under influence of electromagnetic field by meshless methods*, Cupled problems 2015 181–190 (2015).

[2] H. Sadat *et al.*, *Application of the diffuse approximation for solving fluid flow and heat transfer problems*, International Journal of Heat and Mass Transfer 39, 214–218 (1996).

[3] C. Prax *et al.*, *Evaluation of high order versions of the diffuse approximate meshless method*, Applied Mathematics and Computation 186, 1040–1053 (2007).

[4] T. Sophy *et al.*, *On the Numerical Solution of Unsteady Fluid Flow Problems by a Meshless Method*, Revue Europenne des lments 11, 989–1004 (2002).

[5] R. Vertnik *et al.*, *Solution of a continuous casting of steel benchmark test by a meshless method*, Engineering Analysis with Boundary Elements 45 (2014).

[6] S. Patankar, *Numerical Heat Transfer and Fluid Flow*, CRC Press, New York, 1 edition edn. (1980).

[7] H. Lin *et al.*, *The Meshless Local Petrov-Galerkin (MLPG) method for solving incompressible Navier-Stokes equations*, CMES - Computer Modeling in Engineering and Sciences 2, 117–142 (2001).

[8] Q. Du *et al.*, *Modeling Macrosegregation during Direct-Chill Casting of Multicomponent Aluminum Alloys*, Metallurgical and Materials Transactions A 38, 180–189 (2007).

A comparative analysis of meshless methods for dynamic coupled thermoelasticity problem

Boštjan Mavrič

University of Nova Gorica, Vipavska 45, 5000 Nova Gorica

Abstract

A meshless local radial basis function collocation method is applied to two-dimensional transient coupled thermoelasticity problem in Cartesian coordinates. The problem consists of equation of motion for deformations coupled with heat transport equation. The proposed method uses nine nodes in the influence domains and multiquadrics with shape parameter value of 10^{-3} with linear augmentation monomials to discretize differential operators. Second order backward differentiation formula is used for time stepping. The method is applied to a quasi one-dimensional transient benchmark problem. The tests are performed for two possible ways of generating the stress wave: by thermal shock and by pressure shock. Results are compared with the solution obtained by a novel version of the meshless local Petrov-Galerkin (MLPG) method. Our method is found to match the results obtained with the MLP well, with some discrepancies resulting from different treatment of traction boundary conditions.

Keywords: local radial basis function collocation method, local Petrov-Galerkin method, meshless methods, Kriging, collocation, thermomechanics

1. Introduction

Thermomechanical phenomena are important in many different fields of science and engineering, since they have significant impact on constructions and parts that either undergo repeated reheating cycles or are exposed to fast changes in temperature. The stresses generated during this kind of events greatly affect the reliability and failure rate of engineering parts and

Email address: bostjan.mavric@imt.si (Boštjan Mavrič)

scientific equipment. Therefore a considerable effort is made in developing new methods to model this kind of phenomena.

To accurately model the thermomechanical problems we need to simultaneously solve two sets of equations: a hyperbolic equation of motion for elastic deformation and a parabolic equation governing the heat conduction. Different nature of the governing equations prevents us from obtaining any analytical solutions of the fully coupled problem. The exact soutions can be obtained only if we omit full coupling as done in the fundamental work by Danilovskaya [1]. To benchmark numerical methods on fully coupled problems we are thus limited to cross-code comparisons.

Since numerical methods are of great practical importance in the field of coupled thermomechanics, many reference solutions using different approaches can be found. From traditional methods used in commercial codes, to contemporary methods including a large spectra of meshless approaches [2, 3, 4, 5].

The local radial basis function collocation method (LRBFCM) is in this paper extended to coupled thermoelasticity problem. The method calculates the discretized differential operators using a local interpolant constructed from radial basis functions and linear monomials. The formulation of the method is given in detail in section 3. The method has been successfully applied to many different fields in science and engineering [6, 7, 8] including the work done by the present authors in the field of solid mechanics [9, 10].

Because of the great interest in the meshless methods comparisons between them are quite common. Great reference in this regard is [11]. There have also been some comparisons done between the two methods considered in this paper regarding the computational time and accuracy when solving parabolic problems [12], which found the MLPG method to be slower of the two, but just as accurate.

In this paper we will first present the benchmark problem we are solving, and then present a detailed formulation of the LRBFCM method. The formulation of the method is followed by a short discussion on the implementation details followed by the result for the two cases: the temperature driven shock and the pressure driven shock.

In this work, we compare the solutions with the results provided by the meshless local Petrov-Galerkin method (MLPG) using Kriging interpolation, as described in [13]. We chose the specified method because it belongs to the class of well-known meshless local Petrov-Galerkin methods [14, 15] and has been already successfully used in many different fields ranging from fluid mechanics [16] and convection-diffusion problems [17] to piezo-

electricity [18] and solid mechanics [4].

2. Governing equations

In this work we are solving the coupled thermoelasticity problem given by the following equations for temperature T, velocity $\boldsymbol{v}$ and deformation vector fields $\boldsymbol{u}$ [19]

$$\rho c_p \dot{T} = k\nabla^2 T - \beta T_0 \nabla \cdot \boldsymbol{v} \tag{1}$$

$$\rho \dot{\boldsymbol{v}} = (\lambda + 2G)\nabla^2 \boldsymbol{u} + (\lambda + G)\nabla\nabla \cdot \boldsymbol{u} - \beta\nabla(T - T_0) \tag{2}$$

$$\dot{\boldsymbol{u}} = \boldsymbol{v}. \tag{3}$$

Here ρ represents mass density, c_p heat capacity, k the thermal conductivity, β the thermoelastic coupling parameter given by $\beta = (\lambda + 2G)\alpha$, where α is the thermal expansion coefficient. The mechanical material properties are given by the Lamé parameters λ and G. The temperature at which the thermal strains are assumed to be zero is denoted by T_0. The equations are stated in terms of first time derivatives by introducing the auxiliary velocity field $\boldsymbol{v}$, which is otherwise not present in the equations.

To allow easier comparison of the results, we introduce standard dimensionless quantities for coordinate x_i, time t, stress σ_{ij}, temperature T and deformation u_i [20]:

$$\begin{aligned}
\hat{x}_i &= \frac{x_i}{l}, \\
\hat{t} &= \frac{tC_1}{l}, \\
\hat{\sigma}_{ij} &= \frac{\sigma_{ij}}{\beta T_0}, \\
\hat{T} &= \frac{T - T_0}{T_0}, \\
\hat{u}_i &= \frac{\lambda + G}{a\beta} u_i,
\end{aligned}$$

where the length scale is determined by $l = k/\rho c_p C_1$ and the time scale by the speed of the longitudinal wave $C_1 = \sqrt{(\lambda + 2G)/\rho}$.

The thermoelastic coupling is measured by the dimensionless thermoelastic parameter C defined as [20]

$$C = \frac{T_0 \beta^2}{\rho c_p (\lambda + 2G)}, \tag{4}$$

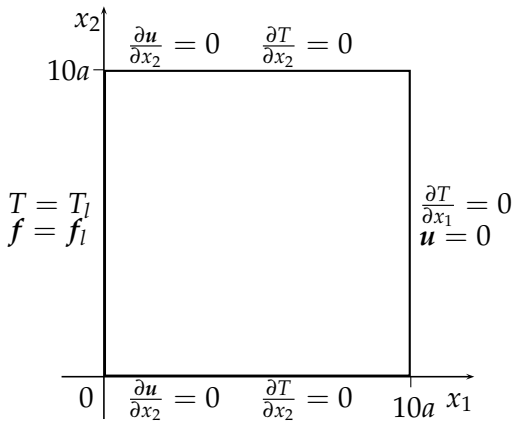

Figure 1: Boundary conditions. On the top and the bottom symmetry boundary conditions are specified. On the right edge, the material is thermally isolated and fixed by specifying deformation to be zero. On the right hand side we stimulate the system by either thermal or pressure shock.

with $C = 0$ denoting uncoupled case. Typical values found in real materials range from 0.01 to 0.1.

2.1. Boundary conditions

The benchmark problem is the same as the one described in [13]. We are considering a square shown in Fig. 1 with side length $10a$, thermally isolated on all sides, except for the left side at $x_1 = 0$, where the temperature value T_l is given. On the same side the traction is specified by $\boldsymbol{f}_l$, while on the side at $x_1 = 10a$ the deformation is set to 0. On the top ($x_2 = 10a$) and bottom ($x_2 = 0$) sides the symmetry boundary conditions are assumed. Different benchmark settings are specified by changing the values T_l and $\boldsymbol{f}_l$.

3. Discretization of the governing equations using local radial basis function collocation method

3.1. Domain discretization and sub-domain selection

We consider a compact domain Ω with boundary Γ. Firstly, the computational points, called nodes, are distributed over the interior and on the boundary of the domain, thus defining the computational domain. The nodes used in this work are positioned on a rectangular grid, however use

of more general meshes is possible [21]. The position of l-th node is denoted with $\boldsymbol{r}_l$. To generate the approximation of the solution at each node, a set of neighboring points ${}_l\Omega$, called the subdomain, needs to be chosen. Although the choice of the subdomain is in principle arbitrary, given that every subdomain overlaps with at least one of the others, usually a certain number of nearest neighbors is chosen. We denote the number of nearest neighbors in the subdomain of the node with index l by ${}_lN$. We note that with the choice of the subdomain, we have introduced a mapping ${}_ls$ from the set of integers from 1 to ${}_lN$ to the global index assigned to every computational node.

3.2. Construction of local interpolants

The field values are interpolated over the nodes in the subdomain using translations of multiquadrics (MQ), one of the many examples of radial basis functions (RBFs). An MQ centered at node i is given by

$$\Phi_i(\boldsymbol{r}) = \sqrt{\sum_\xi \frac{\epsilon^2}{h_i^2}(x_\xi - x_{i,\xi})^2 + 1}. \tag{5}$$

Here ϵ is the shape parameter and h_i is the size of the subdomain, on which the interpolation is being constructed. It is defined as

$$h_i = \sqrt{\sum_{j=1}^{{}_lN} \frac{|\boldsymbol{r}_{{}_is(j)} - \boldsymbol{r}_i|^2}{{}_lN - 1}}. \tag{6}$$

Since MQ's are only conditionally positively definite, the interpolation problem in which only MQ's are used is not well defined. The solution is to augment the interpolation problem with m monomials $p_i(r)$, of up to linear order. The approximation of an arbitrary field $\boldsymbol{y}$ approximation is then given by

$$y_\xi(\boldsymbol{r}) \approx \sum_i^{{}_lN} {}_l\alpha_{i,\xi}\Phi_i(\boldsymbol{r}) + \sum_{i={}_lN+1}^{{}_lN+m} {}_l\alpha_{i,\xi}p_i(\boldsymbol{r}) = \sum_i^{{}_lN+m} {}_l\alpha_{i,\xi}\Psi_i(\boldsymbol{r}). \tag{7}$$

Here the subdomain l is the subdomain centered on the node closest to the test point $\boldsymbol{r}$. The index ξ is running over the components of the physical field which is being interpolated.

The main idea of the method is to use the approximation in Eq. (12) to estimate any linear differential operator $\mathcal{D}$ acting on a physical field $\boldsymbol{y}(\boldsymbol{r})$.

Since the coefficients ${}_l\alpha_{i,\xi}$ are constants, it is straightforwad that

$$\mathcal{D}\boldsymbol{y}(\boldsymbol{r}) = D_{\xi\chi}(\boldsymbol{r})y_\chi(\boldsymbol{r}) \approx \sum_{i,\xi}^{{}_lN+m} {}_l\alpha_{i,\xi}\, D_{\xi\chi}(\boldsymbol{r})\Psi_i(\boldsymbol{r}). \tag{8}$$

The coefficients ${}_l\alpha_{i,\xi}$ are determined by collocation of the field values at each domain point. For the points on the boundary the boundary condition $B_{\xi\chi}(\boldsymbol{r})y_\xi(\boldsymbol{r}) = b_\xi(\boldsymbol{r})$ is imposed instead. In this manner we obtain an interpolant that analytically satisfies the boundary conditions. The system of equations is written in matrix form

$$\sum_{i,\chi} {}_lA_{ji,\xi\chi}\, {}_l\alpha_{i,\chi} = {}_l\gamma_{j,\xi} \tag{9}$$

defining the local collocation matrix ${}_lA$ and collocation right-hand side column ${}_l\gamma$. The indices ξ, χ and ζ run over the components. The elements of the collocation matrix are given by

$${}_lA_{ji,\xi\chi} = \begin{cases} \Psi_i(\boldsymbol{r}_{{}_ls(j)})\delta_{\xi\chi} & \text{if} \quad \boldsymbol{r}_{{}_ls(j)} \in \Omega \\ B_{\xi\chi}(\boldsymbol{r}_{{}_ls(j)})\Psi_i(\boldsymbol{r}_{{}_ls(j)}) & \text{if} \quad \boldsymbol{r}_{{}_ls(j)} \in \Gamma \\ p_j(\boldsymbol{r}_{{}_ls(i)})\delta_{\xi\chi} & \text{if} \quad j \geq {}_lN \end{cases} \tag{10}$$

and the elements of the right-hand side vector by

$${}_l\gamma_{j,\xi} = \begin{cases} y_\xi(\boldsymbol{r}_{{}_ls(j)}) & \text{if} \quad \boldsymbol{r}_{{}_ls(j)} \in \Omega \\ b_\xi(\boldsymbol{r}_{{}_ls(j)}) & \text{if} \quad \boldsymbol{r}_{{}_ls(j)} \in \Gamma \\ 0 & \text{if} \quad j \geq {}_lN \end{cases} . \tag{11}$$

3.3. Application to differential operators

Now we have everything set up to discretize the differential operator $\mathcal{D}$. As it has already been noted it is possible to use the RBF-interpolant to estimate the value of a differential operator. At each node l we can approximate the operator value by

$$D_{\xi\chi}(\boldsymbol{r}_l)y_\chi(\boldsymbol{r}_l) \approx \sum_{i,\xi}^{{}_lN+m} {}_l\alpha_{i,\xi}\, D_{\xi\chi}(\boldsymbol{r}_l)\Psi_i(\boldsymbol{r}_l). \tag{12}$$

The coefficients ${}_l\alpha_{i,\xi}$ are however unknown. They can be determined by solving the system given by the Eq. (14) by formally calculating the matrix ${}_lA^{-1}$. Using the inverse, the expansion coefficients can be expressed

in terms of the elements of the column ${}_l\underline{\gamma}$. The value of the differential operator stated in Eq. (17) is then written as

$$D_{\xi\chi}(\boldsymbol{r}_l)y_\chi(\boldsymbol{r}_l) \approx \sum_{k,\chi} {}_l\gamma_{k,\chi} \sum_{i,\zeta} {}_l A^{-1}_{ik,\zeta\chi} D_{\xi\zeta}\Psi_i(\boldsymbol{r}_l). \tag{13}$$

Although this equation appears quite involved, it represents nothing but multiplication of field values with weights in the same manner as it is usual for the finite difference methods.

3.4. Time stepping

To discretize the time domain, the field values $\boldsymbol{v}$, $\boldsymbol{u}$ and T are assembled in a column $\underline{Y}$

$$\underline{Y} = \begin{bmatrix} \boldsymbol{v} \\ \boldsymbol{u} \\ T \end{bmatrix}. \tag{14}$$

The set of governing equations becomes

$$\dot{\underline{Y}} = G(Y, t). \tag{15}$$

To propagate the system in time second order backward differentiation formula is used [22]

$$\underline{Y}_n = \frac{4}{3}\underline{Y}_{n-1} - \frac{1}{3}\underline{Y}_{n-2} + \frac{2}{3}\Delta t G(\underline{Y}_n, t_n), \tag{16}$$

where t represents time and Δt the step size. The implicit stepping given by Eq. (21) is solved using Newton-Rhapson method using GMRES iterations to solve the linearized system. The Jacobian matrix is estimated using forward difference formulas. The first step is calculated using implicit midpoint Euler method.

4. Results

The method was implemented in Fortran and compiled using Intel Visual Fortran 2014. The implementation of the GMRES (generalized minimal residual method) from Intel MKL was used. The results shown were obtained by the method using ${}_lN = 9$ nodes per influence domain and the shape parameter value $\epsilon = 10^{-3}$. The operator weights were calculated in quadruple precision, while the rest of the calculations was performed in double precision arithmetics.

The results for two benchmark cases were compared. The first, when only thermal shock is applied to the boundary at $x_1 = 0$ and the second, when the pressure shock is applied to the same side. For each of the cases two different values of the thermomechanical coupling parameter C are used: $C = 0$ and $C = 0.1$.

4.1. Thermal shock

In this case the boundary condition on the left side is $T_l = 5t\exp(-2t)$ and $f_l = 0$. The results for deformation $\hat{u}_1$ are shown in Fig. 2 and the temperature in Fig. 3. We can see that the LRBFCM can accurately reproduce the results obtained by the MLPG method for the temperature field. However, some differences appear when the deformation is considered, especially near the boundary at $x_1 = 0$.

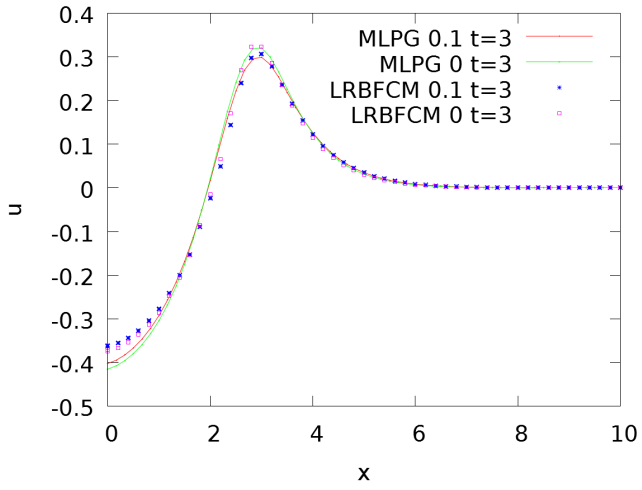

Figure 2: Deformation in x_1 direction for the case of thermal shock at $\hat{t} = 3$. The lines show the solution obtained by MLPG, while the dots represent the solution values obtained by LRBFCM.

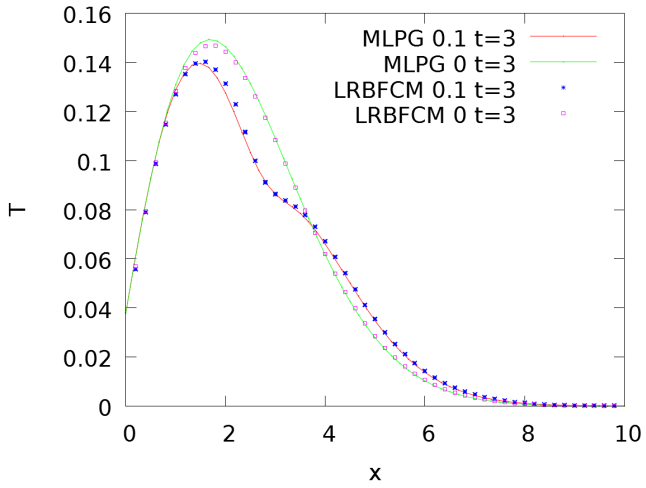

Figure 3: Temperature profile for the case of thermal shock at $\hat{t} = 3$. The lines show the solution obtained by MLPG, while the dots represent the solution values obtained by LRBFCM.

4.2. *Pressure shock*

The condition on the left boundary is $T_l = 0$ and $\boldsymbol{f_l} = (5t\exp(-2t), 0)$. The results for deformation $\hat{u}_1$ are shown in Fig. 4 and for temperature in Fig. 4. In this case the difference in the treatment of the boundary conditions for $\hat{u}_1$ at $x_1 = 0$ is even more pronounced, since, in this case, this is the driving term. From Fig. 4 we can see that the deformation jump caused by the thermal shock, which is calculated by the LRBFCM solution, does not reach the same amplitude as the one calculated by the MLPG. This difference is then transferred also to the temperature profile shown in Fig. 5. The lower amplitude of the jump in the deformation does not heat the material as much as the jump reproduced with the MLPG method. The temperature obtained by the LRBFCM is thus always lower than the one obtained by MLPG.

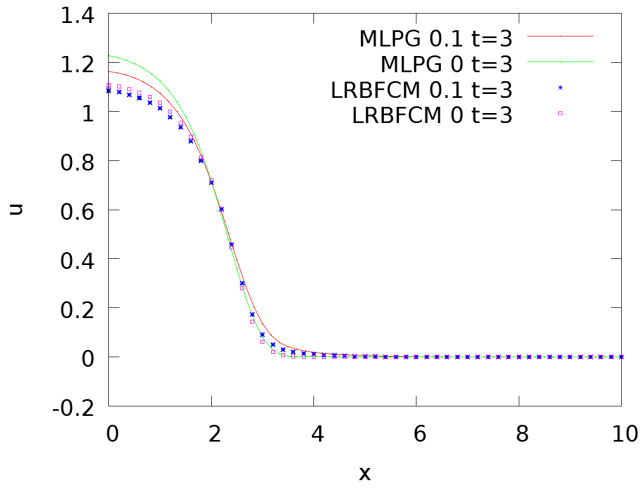

Figure 4: Deformation in x_1 direction for the case of pressure shock at $\hat{t} = 3$. The lines show the solution obtained by MLPG, while the dots represent the solution values obtained by LRBFCM.

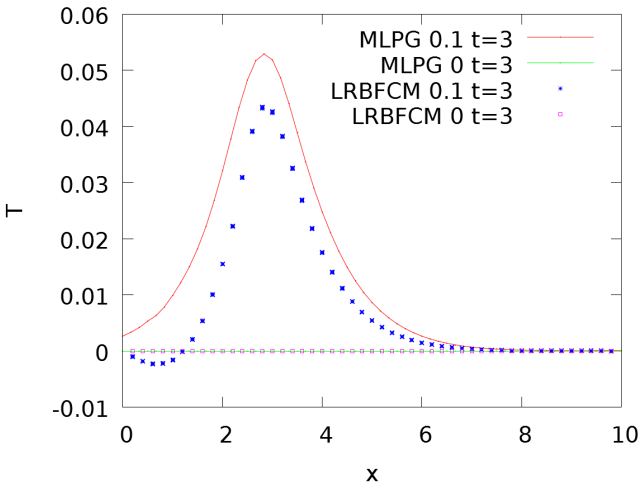

Figure 5: Temperature profile for the case of pressure shock at $\hat{t} = 3$. The lines show the solution obtained by MLPG, while the dots represent the solution values obtained by LRBFCM.

5. Conclusions

We can see that the current implementation of the LRBFCM and the MLPG method show some discrepancies when treating the traction boundary conditions. There are several possible reasons for this: the approaches of the methods are slightly different as the MLPG solves the problem in weak formulation while the LRBFCM solves the strong formulation problem. The problems with the treatment of some types of boundary conditions are well known to be present in methods that use weak formulation [23]. It is also possible that in the current LRBFCM code a bug dwells in the part of code responsible for the treatment of the traction boundary conditions.

Apart from the problem with traction boundary conditions, the LRBFCM method performs quite well. The algorithm used for solution of Eq. (21) is accurate and stable. The iterative nature of the GMRES also keeps the time of the computation as a whole linearly proportional to the number of discretization nodes and thus not prohibitively long for large node counts.

In the future we plan to find the reason for the discrepancies present in the current results. The application of a solver capable of modeling viscoplastic materials to the same benchmark problem is also planned for the future.

Acknowledgments

The author would like to express his gratitude to mr. Zheng Hui from Computational Mechanics group of University of Siegen and to the authors of [13] for providing their data which was used in comparisons. The research done in this paper was funded by Young Researchers programme of the Slovenian research agency ARRS.

References

[1] V. Danilovskaya, *On a dynamical problem of thermoelasticity*, Prikl. Mat. Mekh. 16, 341–344 (1952).

[2] P. Hosseini-Tehrani *et al.*, *BEM analysis of thermal and mechanical shock in a two-dimensional finite domain considering coupled thermoelasticity*, Engineering Analysis with Boundary Elements 24, 249–257 (2000).

[3] J. Sladek *et al.*, *Meshless local petrov-galerkin method for linear coupled thermoelastic analysis*, CMES - Computer Modeling in Engineering and Sciences 16, 57–68 (2006).

[4] J. Sladek *et al.*, *Two-and three-dimensional transient thermoelastic analysis by the MLPG method*, CMES - Computer Modeling in Engineering and Sciences 47, 61–95 (2009).

[5] C. Zhang *et al.*, *Thermomechanical analysis of functionally graded materials*, in *AIP Conference Proceedings*, vol. 1233, 935–940 (2010), URL `http://dx.doi.org/10.1063/1.3452305`.

[6] G. Kosec *et al.*, *Simulation of semiconductor devices with a local numerical approach*, Engineering Analysis with Boundary Elements 50, 69–75 (2015).

[7] R. Vertnik *et al.*, *Local collocation approach for solving turbulent combined forced and natural convection problems*, Advances in Applied Mathematics and Mechanics 3, 259–279 (2011).

[8] K. Mramor *et al.*, *Low and intermediate Re solution of lid driven cavity problem by local radial basis function collocation method*, CMES: Computer Modeling in Engineering & Sciences 92, 327–352 (2013).

[9] B. Mavrič *et al.*, *Local radial basis function collocation method for linear thermoelasticity in two dimensions*, International Journal of Numerical Methods for Heat & Fluid Flow (In review), to appear.

[10] B. Mavrič *et al.*, *A meshless approach to thermomechanics of DC casting of aluminium billets*, 96, Institute of materials, minerals and mining, London (2014).

[11] G. Liu, *Mesh Free Methods: Moving Beyond the Finite Element Method*, Taylor & Francis (2010), URL `http://books.google.si/books?id=dHKYBOYVb2gC`.

[12] R. Trobec *et al.*, *Comparison of local weak and strong form meshless methods for 2-D diffusion equation*, Engineering Analysis with Boundary Elements 36, 310–321 (2012), URL `http://linkinghub.elsevier.com/retrieve/pii/S0955799711001871`.

[13] B.-J. Zheng *et al.*, *A novel meshless local Petrov-Galerkin method for dynamic coupled thermoelasticity analysis under thermal and mechanical shock loading*, Engineering Analysis with Boundary Elements (2015).

[14] S. N. Atluri, *The meshless method (MLPG) for domain & BIE discretizations*, Tech Science Press, Forsyth, GA (2004).

[15] J. Sladek *et al.*, *Applications of the MLPG method in engineering & sciences: a review*, Comput. Model. Eng. Sci 92, 423–475 (2013).

[16] H. Lin *et al.*, *The meshless local Petrov-Galerkin (MLPG) method for solving incompressible Navier-Stokes equations*, CMES- Computer Modeling in Engineering and Sciences 2, 117–142 (2001), URL `http://care.eng.uci.edu/pdf/(01.5).pdf`.

[17] H. Lin *et al.*, *Meshless local Petrov-Galerkin(MLPG) method for convection diffusion problems*, CMES(Computer Modelling in Engineering & Sciences) 1, 45–60 (2000), URL `http://care.eng.uci.edu/pdf/(00.1).pdf`.

[18] J. Sladek *et al.*, *Meshless local Petrov-Galerkin method for plane piezoelectricity*, CMC: Computers, Materials & Continua 4, 109–117 (2006).

[19] Y. C. Fung *et al.*, *Classical and Computational Solid Mechanics*, vol. 1 of *Advanced Series in Engineering Science*, World Scientific, Singapore (2008).

[20] R. Hetnarski *et al.*, *Thermal stresses - Advanced theory and applications*, Solid Mechanics and its Applications 158, 1–591 (2009).

[21] S. Simonenko *et al.*, *Optimal shape parameter for the solution of elastostatic problems with the RBF method*, Journal of Engineering Mathematics 85, 115–129 (2014), URL `http://dx.doi.org/10.1007/s10665-013-9636-7`.

[22] S. Širca *et al.*, *Računske metode za fizike*, DMFA - založništvo, Ljubljana (2010).

[23] Y. Chen, *Meshless methods in solid mechanics*, Springer, New York, NY (2006).

Sustainability evaluation of different domestic waste collecting approaches

Slavica Schuster

University of Nova Gorica, Vipavska 13, SI-5000 Nova Gorica

Abstract

Waste management has a specific life cycle — one can not go without the other; and in other words said, one has an impact to another. This research is focused on how to make a new, efficient model which will bring lower consumption of energy and lower costs in waste management, we created a questionnaire, which will be sent to waste management municipality companies in Slovenia and Croatia, in order to find current ways of handling waste. Second questionnaire will to give us data which is going to help us calculate lower costs for municipality companies, and also, for the residents of these municipalities, with high energy savings. In the end this paper is going to create (or redefine) our model in a way which will be acceptable to the municipality and their residents. Also for the environment it must be defined in framework of sustainable development.

Keywords: waste collecting, waste environment

1. Introduction

Municipal waste is waste that comes from households, cleaning public areas and is similar in its content and characteristics to household waste. Communal services take care of this kind of waste, since they are in charge of regular collection and disposal of such waste. At present, several different methods exist, regarding waste collection, that are closely related to the efficiency of waste separation and to further management of waste. Waste collection itself also causes quite high economical and ecological loads, making the choice of a cost and separation effective method essential. Reuse of waste is much easier if it is collected separately, thus reducing en-

Email address: slave18@gmail.com (Slavica Schuster)

ergy consumption and costs. These facts are going to be closely explained in further chapters. Our goal is to see how waste is transported in chosen areas. Is it separated in the end (at waste landfills) or is it separated at the beginning.

This paper presents ways of collecting waste in chosen municipalities in Slovenia and Croatia, and the analysis of gathered data. The main difference in collecting waste in Slovenia and Croatia are similar to differences among individual municipalities. One main difference in waste collecting in Croatian households is that in Croatia there are still municipalities, which do not separate waste – all is put in one container and that container is emptied once a week by municipal collecting truck of that municipality.

Waste collection is the first phase of waste management and must be made to include :

- reduction,
- re-use,
- recycling and
- recovery

and is adapted to the purpose of further treatment of waste.

The waste is collected in several ways. Systematic classification methods are possible according to the fraction (material composition) of waste and transport (road, rail, water, hydraulic transport, pneumatic transport).

Road transport is in relation to: the level of care (distance from the waste can, where is firstly collected, to the place where it's going to be put under treatment), the frequency removal (draining container for road transport), the size of the tank (it depends on the amount of waste).

1.1. The purpose of the research

The purpose of this research is to study different domestic waste collecting systems, its transportation and to compare economic and environmental costs of these approaches.

We would like to determine which solution would bring lower costs, for household and for municipality companies and which would cause the lowest environmental impact.Environmental costs are evaluated through energy accounting, ecological footprints and Life Cycle Assessment.

Our hypotheses are:

1. Reducing the amount of produced domestic waste and increasing efficiency of waste separation, resulting in lower environmental and economic costs.
2. Transportation of waste represents the highest environmental and economic costs in the process of collecting domestic waste. Approaches which require smaller transport distance are more sustainable.
3. Collection of mixed domestic waste (without separation at the source) or systems with low efficiency of waste separation have lower economic costs of waste collection but higher environmental costs.
4. Different approaches toward evaluation of environmental cost have quite unique findings and level of complexity. The Life Cycle Assessment approach will show the highest environmental loads.
5. People are generally willing to accept changes in the waste collecting system as long as this does not mean higher costs, extra work and extra traveling distances.
6. People have a positive attitude towards methods that promote a better separation of waste and decrease in their environmental load.

2. Theoretical Background

The definition of waste is [12]: Waste are substances and objects that the owner, or producer of waste (legal or physical person), has rejected or disposed, or intends or must dispose.

Besides this legal definition of the term "waste", in practice a number of definitions may be encountered.

1. Waste is the sum of produced and consumed remains.
2. Waste is a clear imprint of material life of people.
3. Waste is still not a well established source of raw materials and energy.
4. Waste is a variable sum of various substances and energy.

Waste is [2] an unnecessary product of human activities at a given time. Another definition says that waste is the material which we cannot use or do not want to use from economical reasons any longer.

Waste contains many useful materials which can be processed or used for production of new products. If waste production can not be avoided, it should be re-used and collected by types (waste separation) at the point (place) of its production. This saves space on existing landfills.

The simplest example of separated collection is separation of paper and cardboard, which makes one fifth of household waste, and can be recycled

several times, thus saving water, energy and wood. Glass [3] can be fully recycled several times, so can plastic and metal packaging.

Waste management is a set of activities, decisions and measures focused on: waste prevention, waste reduction and/or its harmful environmental impact, collection, transport, use, disposal and other activities related to waste, as well as supervision over these activities, taking care of closed landfills.

Waste management [22] must be implemented in a way which does not bring human health in danger and without using procedure and/or methods that might harm the environment such as sea, water, soil and produce air pollution, noise pollution, and so on.

Preserving the environment by separated collection and recycling of waste brings the following benefits better use of waste products and cost reduction (so-called, co-management of existing facilities), decrease of import of secondary raw materials (e.g. glass, paper and metal waste) hiring employees, decrease of treatment and disposal costs.

There are [6] two main determinants of waste collection:

- separation of usable waste (glass, paper, cardboard, metal, bio-waste, plastic), with purpose of recycling and use,
- separation of problematic substances, i.e. dangerous waste (oil, chemicals, batteries, medicines, etc.), with purpose of detoxification and recycling.

2.1. The waste management hierarchy

Our research will focus on waste collecting and not on waste management after the waste is collected. However, as waste collection and further waste management are interconnected, we have to briefly describe general principles and priorities.

2.2. Ecological Footprint

The Ecological Footprint [6] is a resource accounting tool that measures how much biologically productive land and sea is used by a given population or activity, and compares this to how much land and sea is available. Productive land and sea areas support human demands for food, fiber, timber, energy, and space for infrastructure. These areas also absorb the waste products from the human economy.

The Ecological Footprint measures the sum of these areas, wherever they physically occur on the planet and is widely used as a management

and communication tool by governments, businesses, educational institutions, and non-governmental organizations.

The ecological footprint can be seen or "scanned" in given areas [7]: energy, food production, forests, water and waste.

All given areas cannot be "scanned", or ecological footprint cannot be calculated without deeper view on area of technology, because the way we use technology has impact on our ecological footprint.

Ecological footprint (EF) [7] of some country can be calculated through

$$EF(c) = EF(p) + EF(i) - EF(e) \tag{1}$$

where $EF(c)$ is ecological footprint of consumption or total ecological footprint, $EF(p)$ is ecological footprint of production (total ecological footprint given by exploiting of all resources and bio-productive areas within the boundaries of some country), $EF(i)$ is ecological footprint of import (total ecological footprint which we import from other countries and spend their resources, regardless whether we're talking about energy, food or merchandise) and $EF(e)$ is ecological footprint of export (total ecological footprint which we export to other countries and their inhabitants spend).

Waste disposing [10] has huge environmental impacts and can cause serious problems. It's a fact that waste (waste disposal) [9] can have negative environmental effects, such as: surface water contamination, soil contamination, pollution and leachate (as water trickles through contaminated ground, it causes liquid formation which is called leachate). From knowing the negative effects, we can conclude what would happen, if we reduce waste or collect it and dispose it in a proper way, thus keeping our environment much "healthier". Proper ways of waste management can not only reduce contamination of the environment, but also reduce the costs that keep gathering from improper waste disposal.

On a global scale, education is key. Those who exercise [30] poor waste management techniques may not fully understand the impact of their actions. Teaching identification of different types of waste and appropriate disposal methods is one initiative that can be accomplished globally to reduce improper waste management. Many, however, know the consequences of their actions but have no other choice since their government does not provide proper waste disposal methods. In such cases, we need to help those governments implement the necessary waste management infrastructure.

2.3. Economy and energy in waste transportation

Transportation [31] plays a major role in sustainability of the Earth, but it also must be sustained in order for all people to continue to afford access to economic and social opportunities necessary for meaningful life. According to that, there are two sides of energy use in transportation:

- large contribution made especially by highways transportation sources to pollution problems,
- energy supply security for transportation sectors of each country.

Even though that article is about energy and energy efficiencies in the Chinese transportation sector, we can relate to it in order to conclude:

- Energy and economy in waste transport are related – the bigger the distance between container and landfill is, there is more energy invested and cost more money. Therefore, high consumption of energy and higher costs are not in accordance to sustainable development.

Sustainability [12] is an urban development priority. Thus, energy and carbon dioxide emission reduction is becoming more significant in the sustainability of urban transportation systems. Urban transportation systems are complex and involve social, economic, and environmental aspects.

As the social economy continues its rapid development [13], the topic of sustainable development is an important issue for the world. Sustainability refers to meeting the needs of the present without compromising the ability of future generations to meet their own needs. For humans, in particular, sustainability corresponds to the long-term maintenance of responsibility and has three dimensions: environmental sustainability, economic sustainability, and social sustainability.

Practical use of sustainable development [14] areas which are important in living by principles of sustainable development:

- We should consider three elements: impact on environment and climate, the feasibility in given time and economic costs.
- Transport is directly linked to energy, and today it entirely depends on oil.
- Food production has alway shed great importance for humanity, because it is about production of energy which is necessary for survival.
- Waste production needs to be reduced to save energy. We have created a civilization of waste.

- Bio-capacity needs to be protected. For example, forests must be preserved because they produce oxygen that we need for breathing. In other words, our life depends on it.

- Other levels: by changing ourselves as individuals, we can affect others. Decisions we make are the first step in changing the environment that we live in.

Energy independence [2], energy security, and sustainability are key factors that drive every nation's pursuits to achieve a stable and prosperous economy. With the growing penetration of renewable power generation sources within the electric sector, the penetration of HSR within the US national transportation portfolio seems highly promising to achieve the goals of energy independence, security, efficiency and sustainability. The presented model can be applied to other geographic regions, such as regions with matured HSR markets like Europe.

Assessments of the energy use [15] and emissions from passenger transportation modes are numerous, but rarely are life-cycle assessments (LCA) presented for complete comparisons. In urban regions many transit options may exist and it is not easy to assess each option's energy use or emissions, considering the many influencing variables (vehicle occupancy, fuel types, vehicle age, emissions control devices, and vehicle speed among others). Evaluating vehicle operation environmental factors ignores the life-cycle components of the vehicles, infrastructure, and fuels which are necessary requirements for any transit mode.

The first step [16] towards the widespread use of renewable energy sources and preservation of our environment for the people of the future is to adopt the "green accounting" standards that translate socially and environmentally responsible behavior into monetary terms, the only language businesses understand.

2.4. Ways of waste collection in Slovenia and Croatia

Waste is collected in several ways. Considering the material composition of waste (fractions that are separated) and transport (road, rail, water, hydraulic and pneumatic transport).

In Slovenia [17], there are collective centers in practice known as recycling centers or recycling "yards", with waterproof surface, designed to allow access for trucks and machines used for waste transport. 20 – 60 % of the collective center area is usually covered by roofs or semi-enclosed roofs. The official gazette of the Republic Slovenia [18], states in article 6

from 2001, (in Resolution of waste management for separate collection of fractions in the public service for waste collection), that every area with 500 residents should have regulated waste collection point – a collective center.

Every inhabitant of Slovenia [17] annually produces about 1.7 kg of municipal waste per day. The amount of municipal waste places Slovenia below the average of the European union.

As regards to the way of waste collection in Croatia, it is quite different compared to Slovenia. In Croatia, specific household containers for waste collection are still used. On the official sites of Ministry of Environment and Nature Protection [19], it is possible to find various laws on waste management, such as Law on sustainable waste management, Waste management strategy for Republic of Croatia and Regulations on waste management.

Regulations on waste management [20] prescribe the procedures for recovery and/or disposal of waste,categories, technical and technological conditions for landfills, required qualifications of employees performing storage, use and/or disposal of waste, and the methods of management and delivery of data on waste management. Even though there are regulations on waste management, Croatia has difficulties in supervision – it is possible to say that the system itself is not regulated enough, so there are "loopholes" in every part of the system.

2.5. Waste collection in other countries (Germany, Austria, Italy, Serbia)

2.5.1. Germany

Germany is a Federal Republic [21] consisting of sixteen Federal States (Bundesländer). Responsibility for waste management and environmental protection is shared between the national Government, the Federal States and local authorities. Germany produces [22] 30 million tons of waste annually. The Green Dot system has been one of the most successful recycling initiatives, which has literally put packaging on a diet. The point is that manufacturers and retailers have to pay for a "Green Dot" on products: the more packaging there is, the higher the fee. This clever system has led to less paper, thinner glass and less metal being used, thus creating less waste to be recycled. In Germany [23], it is common to divide waste into different groups instead of throwing everything into the same container.

2.5.2. Austria

According to the Austrian constitution [24] the responsibility for municipal waste management is split between the federal and provincial governments. Austrian laws [25] relating to waste management emphasize the sustainability, protection of people and the environments and protection of

natural resources as an important guideline for waste management in Austria. Applying for regular waste removal service [25] from your property (household waste) for the first time can vary according to city ordinances in the Austrian province where you live.

2.5.3. Italy

The most important piece of Italian waste legislation [7] was issued in 1997 (Legislative Decree 22/97). It shaped the national waste management system (defining the responsibilities of the actors involved), introduced targets about separate collection of municipal waste, established the National Packaging Consortium and provided for the progressive replacement of the old waste tax with a new waste tariff.

In 2015, the European Commission (EC) [26] announced that it was launching legal action against Italy over the chronic waste crisis affecting Naples and the rest of the Campania region. Thousands of tons of waste have been left uncollected in the streets and waste has been disposed of at illegal dump sites. The EC considers that the region's waste disposal installations are inadequate and pose serious problems for human health and the environment.

Even though, over the years [27], the amount of waste that is recycled grows—Italy still needs a better approach in waste management. That is why Italian government is setting a framework to foster more sustainable waste management practices. Italian Environmental Code introduces the concept of compaction – reducing the amount of waste at the source means producing economical advantages for each link of the waste life cycle. At industrial level [27], there are compactors used for different waste streams – waste packaging. A compactor usable on a household level, the Eureka compactor, reduces public dependence on street containers and helps to educate families about waste handling.

2.5.4. Serbia

Serbia has a Waste management law [31], which was published in Official Gazette of Republic Serbia, No 36 from 2009 and No 88 from 2010, that directs: types and classification of waste, waste management planning, subjects of waste management, responsibilities and obligations in waste management, organization of waste management, management of specific waste streams, conditions and procedures for license publishing, waste movement across the state boundaries, report about waste and its databases, waste management funding, supervision and other important

questions of waste management. Waste management is activity of general interest.

As it emerges from the shadow of economic sanctions [31], and previous decades of communist rule, Serbia now faces an enormous challenge to bring its aging waste management infrastructure up to date. Serbia's transition to the market economy occurred much later than in other countries (it has begun after 2001). The pursuit of sustainable development [14] requires that attention be paid to the interactions between the environment, society and economy. During the past several years, a set of environmental laws have been discussed. Rapid industrial development has resulted in an increased need to establish standard procedures in this field, and this is also one of the preconditions Serbia must meet if it is to join European Union.

To make up for lost time, Serbia must speed up the process of integration. Serbia is among the last European countries that do not have a market for communal waste. According to official data, 40% of household waste ends up on one of 4400 unlicensed and unregulated waste landfills, with a little chance of recycling and waste separation. Even though, recycling and waste separation is highly profitable, Serbia is in a position where waste management and profit of it is still a completely new field.

General awareness [14] and knowledge of environmental issues is low. Apart from improving the integration of environmental studies in curriculum of the education system, there is also a need for advanced training in the subject of environmental management for local inhabitants and for local authorities, which can increase the capacity to address local environmental issues at a strategic level.

3. Methods

The methods which are going to be used through our research are questionnaire and analysis of environmental costs, performed in Excel (MS Office). We will use two types of questionnaires: one for waste collecting companies and the other for residents.

3.1. The sampling locations

The sample includes people from several municipalities, which were selected by the following criteria – they are smaller to intermediate settlements with different methods of waste collection and different waste separation efficiency. Municipalities that have been chosen are:

- municipalities from Slovenia: Nova Gorica, Vrhnika, Logatec, Kranj, Ptuj, Celje, Kočevje and Domžale,
- municipalities from Croatia: Koprivnica, Kostrena and Kastav.

3.2. Variable pattern – data from questionnaire

At the very beginning, the questionnaire was sent to the above listed areas (municipalities), to municipality companies, which provided or will provide the desired data on waste (the current state of waste in these municipalities). After that, a new (second) questionnaire will be created and given to 100 people in 2 or 3 selected municipalities. The goal is to collect this data from all municipalities, if possible. Its purpose will be divided in two sections:

1. People will fill the second questionnaire with data that is known for them in current state – we will focus on their opinion and their willingness to accept changes.
2. We are going to show them the results from first questionnaire (inform them about economic and environmental costs of different steps in waste collecting system, and what would individual changes mean for their and environmental costs) and then we are going to ask them to fill (the second) questionnaire.

The second questionnaire will be filled two times so that data which is collected can be compared in order to see, if they have changed their opinions about the waste. With this we will find out if their opinion is based on real facts or is it based on their own "attitude", without any real insight in facts.

3.3. Selection of data about exiting waste collection systems

The first selected municipality was Nova Gorica (Slovenia), where our university is located. In the following, we selected municipalities with similar type of settlement and with different method of waste collection or with different efficiency of waste separation. We selected Vrhnika and Logatec, that have reached very high efficiency of separation of domestic waste. Besides these, we selected some more locations, in which they select domestic waste in slightly different ways (they are collected by different municipal companies) and which share similar settlement pattern and similar population density: Kranj, Ptuj, Celje, Kočevje and Domžale.

Selected municipalities from Croatia are Koprivnica and two municipalities near the city of Rijeka, municipalities Kostrena and Kastav, with

similar population density as for Nova Gorica. Settlements in Croatia were selected in order to explore differences in waste collecting systems in comparison to Slovenia. The questionnaire for municipal companies covered the following categories of questions :

- the number of people who pay waste disposal in a given municipality, amount of collected waste, fractions of waste that are collected, number of containers, eco-islands and collection centers,
- frequency of emptying containers, number of kilometers and hours for transportation of waste,
- price of a working hour, price of machinery and equipment maintenance, other costs related to waste removal,
- monthly cost of waste removal per person or per household.

At the end of the first stage of research we will calculate the energetic and economic price of each individual waste collecting system. Statistical analysis will be done for each selected municipality and then for all municipalities together.

3.4. The alternative model

We are going to ask people if they could predict energetic and economic costs for some of the existing methods of waste collection. For each proposed scenario we will show them calculations, how much energy does it spent and how may economical cost it is causes. For each of the methods we are also going to calculate the ecological footprint. The results will be compared. Among potential scenarios we will include also our (alternative) way of waste collection.

3.4.1. Introduction of alternative model

For faster and more evident comparisons of waste collecting scenarios, we will prepare the model, which will help us calculate energetic and economical cost. With its help, it will be easy to test the sensitivity of the model. Its most important advantage will be the possibility for evident demonstration of differences in energetic and economical costs and how it affect the result (energetic and economical cargo) and how it affects or decreases some of the parameters (number of kilometers, working hours, change of number of the containers and the frequency of the discharge, employees payment, investing in different containers ...). Those parameters were obtained in the first questionnaire.

3.4.2. Model as an educational tool

The model will serve both, as a research and as an educational tool, which will help people see the importance of some of the parameters for final economical and energetic burden (generally, it can contain the environmental impact). For that, we are going to use second questionnaire, to get people's opinion about different waste collecting methodologies and their willingness to accept an alternative model.

4. Results from questionnaire- municipality waste management

After questionnaire has been sent to municipalities (by e-mail), answers were reviewed. Results are formed into tables for easier interpretation. Table 1 presents the population of each municipality and the monthly cost for waste per person. Table 2 presents number of ecological islands, collective centers and number of containers in each municipality. Table 3 presents monthly collected packaging in kilograms (kg) in each municipality. Table 4 presents working hours of communal services per month, number of kilometers traveled by trucks for waste collection per month and the average monthly cost for transport. In those tables VRH is Vrhnika (city in Slovenia), KOČ is Koevje (city in Slovenia), DOM is Domale (city in Slovenia), CE is Celje (city in Slovenia), KOP is Koprivnica (city in Croatia), KOS is Kostrena (city in Croatia) and KAS is Kastav (city in Croatia). It is possible to see, in all tables, that feedback is different (monthly cost for waste per person, number of eco-islands, containers, working hours, cost for transportation, monthly waste packaging in kilograms, traveled miles and penalties), but all selected municipalities stated that their employees perform supervision on waste separation during the collection. Each municipality offered old and new ways of encouraging their residents to separate waste.

Among other answers in questionnaire, these stand out:

- All municipalities have stated that their employees perform supervision during waste collection (to see if waste is properly separated).
- Selected municipalities also offered these ways of encouraging residents for proper waste separation, and also advised some new ways:
  - information fliers, door-to-door,
  - websites,
  - radio, local newspapers,

- educational workshops in schools and kindergartens,
- days of open doors,
- free containers (paid by the municipality) or containers which are given from municipality at half price,
- various booklets which contain allegations how to separate waste,
- banners,
- municipality companies painted vehicles/trucks,
- various magazines,
- various lectures, open to all residents from certain municipalities (with sent invitations).

Table 1: Display of received data for given population of each municipality and the monthly cost for waste (per person/ euro /month), number of residents (a) or households (b)

Municipality	VRH	KOČ	DOM	CE	KOP	KOS	KAS
Population	23.500 (a)	16.700 (a)	34.634 (a)	48.000 (a)	27.053 (b)	1.057 (b)	3.441 (b)
Business facilities						78	243
Cost for collection, transportation and waste disposal	2.06 (a)	3.36 (a)	13 (a)	13 (a)	1.58 (b)	4.41 (b)	4.41 (b)
Cost for collection transportation and bio-waste disposal	3.77	4.98	7.27	12.50	-	-	-

Table 2: Display of received data for given number of ecological islands, collective centers and number of containers.

Municipality	VRH	KOČ	DOM	CE	KOP	KOS	KAS
Number of eco-islands	197	92	117	320	87	0	0
Number of collective centers	1	1	1	1	0	0	0
Number of containers on eco-islands	642	231	610	850	257	0	0

Table 3: Display of received data for monthly collected package in (a)kilograms and (b) tons.

Municipality	VRH	KOČ	DOM	CE	KOP	KOS	KAS
Glass	34.04 (b)	12.6 (b)	770.62 b)	50 (b)	793 (b)	80 (a)	150 (a)
Paper and cardboard	72 (b)	226 (b)	133 (b)	65 (b)	357 (b)	534 (a)	890 (a)
Bio-waste	296 (b)	43 (b)	519 (b)	161 (b)	573 (b)	500 (a)	2.3 (b)
Plastic package	8,4 (b)	-	231 (b)	20 (b)	7.7 (b)	100 (a)	180 (a)
Aluminium package	-	-	96 (b)	-	73 (b)	-	-
Mixed package	139 (b)	-	68 (b)	-	519 (b)	90 (b)	81 (b)

Table 4: Display of received data for working hours of communal services per month, number of kilometers traveled by truck for waste collection per month and the average monthly cost for transport (euro/month).

Municipality	VRH	KOČ	DOM	CE	KOP	KOS	KAS
Average communal services	64	657	156	-	640	192	192
Average numbers of kilometers traveled by truck	47.841	8.700	6.750	-	23.000	1.440	1.440
The average monthly cost for transport	1.333.333	70.000	-	-	469.528	-	-

5. Expected results and contributions to the science

Our research will produce the following results:

- Insight into economical, energetic and environmental costs of different waste collecting approaches.
- A model will enable further improvements in existing waste collecting methodologies and simultaneous monitoring of the three types of costs.
- Research on existing legislation and related possibilities for further improvements.
- Insight into public opinion related to different waste collecting approaches and their willingness to participate in improved waste collecting approaches.
- Effect of education on their willingness to accept new or changed ways of collecting waste.

References

[1] Lončarević Božić, A., Kušić, H., Upravljanje otpadom (Waste management),
https://loomen.carnet.hr/pluginfile.php/267481/mod_resource/content/2/Upravljanje_otpadom_skripta_2012.pdf.
Accessed in April, 2015.(In Croatian).

[2] Krishnan, V. et al., *An optimization model of energy and transportation systems: Assessing the high-speed rail impacts in the United States*, USA: ELSEVIER,2015.

[3] Odvojeno prikupljanje otpada (Seperate waste collection)
http://www.zelenazona.hr.
Accessed in April, 2015 .(In Croatian).

[4] Gospodarenje otpadom (Waste managment)
http://www.cistoca.hr
Accessed in April, 2015.(In Croatian).

[5] Wackernagel M., *O*ur Ecological Footprint Reducing Human Impact on the Earth, Canadian cataloging,1997.

[6] Earth Day Network : Ecological Footprint FAQ, http://www.earthday.org/footprintfaq#ecofootprint Accessed in April, 2015.

[7] Šimleša, D., *Ekološki otisak. Kako je razvoj zgazio održivost (Ecological footprint, Development crushed sustainability)*, Zagreb: Tisak (In Croatian), 2010.

[8] Turn Rund New Media., Environmental impacts,
http://www.greenchoices.org/green-living/waste-recycling/environmental-impacts.
Accessed in April, 2015.

[9] eSchooltoday., Effects of waste and poor waste disposa, l
http://www.eschooltoday.com/waste-recycling/effects-of-poor-waste-management.html2014.
Accessed in April, 2015.

[10] Walls, R. A world of waste., Effect of poor waste management on the planet,

http://www.themindfulword.org/2012/improper-waste-management-disposal2012.
Accessed in April, 2015.

[11] Waste management law l
http://faolex.fao.org/docs/pdf/srb104373.pdfl
Accessed in April, 2015. (In Serbian).

[12] Cheng, Y.-H. et al., *U*rban transportation energy and carbon dioxide emission reduction strategies, Taiwan: ELSEVIER.2015.

[13] Jian, J., *A* factor decomposition analysis of transportation energy consumption and related policy implications, China: International Association of Traffic and Safety Sciences.2014.

[14] Jovanović, P., Making up for the lost decade,
http://www.waste-management-world.com
Serbia, Accessed in April, 2015.

[15] Chester, M. V. et al., *C*omparison of life-cycle energy and emissions footprints of passenger transportation in metropolitan regions, USA: ELSEVIER.2009.

[16] Stanojević, M. et al., *G*reen accounting for greener energy, France: ELSEVIER.2010.

[17] Official gazette of the Republic Slovenia (2001).
https://www.uradni-list.si/_pdf/2001/Ur/u2001021.pdf#!/u2001021-pdf 2001.(Article 6.)
Accessed in April, 2015. (In Slovenian)

[18] Official gazette of the Republic Slovenia
https://www.uradni-list.si/_pdf/2012/Ur/u2012063.pdf#!/u2012063-pdf 2012. (Articles : 24. And 25.)
Accessed in April, 2015. (In Slovenian)

[19] Ministry of Environment and Nature Protection
http://mzoip.hr/hr/otpad/propisi-i-medunarodni-ugovorixx.html
Accessed in April, 2015. (In Croatian)

[20] Regulations on waste management
http://narodne-novine.nn.hr/clanci/sluzbeni/2007_02_23_877.html
Accessed in April, 2015. (In Croatian)

[21] Gear Brand., All about recycling in Germany,
http://www.howtogermany.com 2015.
Accessed in April, 2015.

[22] El-Haggar, S., *S*ustainable Industrial Design and Waste Management, USA: Elsevier Academic Press.2007.

[23] Not all waste is created equal
http://www.study-in-chemnitz.com
Accessed in April, 2015.

[24] General information on waste separation & waste prevention
http://www.come2upperaustria.com
Accessed in March, 2015.

[25] Herczeg, M., *M*unicipal waste management in Austria, Copenhagen Resource Institute: European Environment Agency.2013.

[26] Dal Santo D., Italian Peaks,
http://www.waste-management-world.com/articles/print/volume-8/issue-6/features/italian-peaks.html 2006.
Accessed in April, 2015.

[27] Ferraris, M., Paleari, S., *M*unicipal waste management in Italy, CERIS-CNR: European Environment Agency.2013.

[28] Fischer, C., *M*unicipal waste management in Germany, Copenhagen Resource Institute: European Environment Agency.2013.

[29] Odvojeno prikupljanje otpada (Seperate waste collection)
http://www.6maj.hr
Accessed in March, 2015. (In Croatian)

[30] Zhang , M. et al., *E*nergy and exergy efficiencies in the Chinese transportation sector 1980-2009, China: ELSEVIER.2011.

[31] Žitnik, M. Komunalni odpadki v Sloveniji problem ali izziv?, (Municipal waste in Slovenia-problem or challenge?) EOL 55
http://www.zelenaslovenija.si/revija-eol/arhiv-stevilk-eol/arhiv/759-komunalni-odpadki-v-slovenijiproblem-ali-izziv-eol-5 2009.
Accessed in April, 2015. (In Slovenian)

Ab-initio modeling of peroxy bridge defect in amorphous silica

Blaž Winkler

University of Nova Gorica, Vipavska 13, 5000-Nova Gorica, Slovenia.

Abstract

We have been investigating electronic and optical properties of peroxy link defect (POL) in amorphous silica with first principle methods on 109 atom model. Results show presence of defect induced electronic states within band gap origin from POL with properties strongly depending on a defect geometry. Very low oscillator strength indicates minimal probability of experimental detection. Our calculations were able to reproduce the results of previous studies and give new detailed insight into effects of local geometry to the electronic structure of the defects.

Keywords: silica, defects, numerical modeling

1. Introduction

Silica is an amorphous material widely used in microelectronic and optical technologies. Most commonly it is used as the gate oxide in traditional metal oxide semiconductor field effect transistor (MOSFET) and as the basic compound in optical fibers. Every real material contains imperfections of various sizes which origin from impurities, manufacturing processes, exposures to mechanical stress, chemicals, radiation and many other hazardous environments [1]. With the continuous decrease of the overall transistor size (14nm for second generation tri-gate transistors [2]) and the need for radiation tolerant optical fibers to be used in harsh environments (such as future facilities devoted to fusion) [3, 4, 5], the interest in understanding defects at the atomic scale has been renewed lately.

In general, the presence of defects modify the electric and optical properties of a material by trapping charges and adding absorption / lumines-

Email address: blaz.winkler@ung.si (Blaž Winkler)

cence centers, thus increasing the electronic losses or the optical attenuation. Depending on defect concentration dramatic changes to the dielectric constant and refractive index of the material may occur consequently degrading the performance of the devices. In oxygen surplus silica peroxy radicals can be produced by ionizing radiation or fiber-drawing. It was suggested by [16] that the Peroxy Linkages or POL (≡Si-O-O-Si≡) were the precursor species of peroxy radicals.

Current literature describes POL as common defect in oxygen surplus silicates that can be formed through different chemical routes, including Frenkel pairs formation and the trapping of a O_2 molecule by an oxygen vacancy. The diamagnetic nature of peroxy linkages make their direct identification very difficult from the experimental point of view, as correlations have to be found between different optical techniques and treatments [6]. The properties of POL are uncertain and still under debate (for general review, see [7]).

Experimentally [8] assigned a weak peak at 3.8 eV to POL presence as they observed a significant decrease of the peak absorption intensity after hydrogen treatment and an increase of the hydroxyl peak complemented with the absence of any electronic paramagnetic resonance (EPR) signal. In the later studies of [9, 10] the 3.8 eV band has been re-assigned to Cl_2 impurities . However, as the Cl_2 model alone does not explain the hydroxyl peak increase authors concluded that interstitial oxygen molecules should also be present. In 2000 [11] studied correlation of photoluminescence band at 1.5 eV with optical absorption at 3.8 eV and concluded that their combined origin is more likely POL than Cl_2. In the [12] authors have attributed a broad absorption feature between 6.5 and 7.8 eV to the presence of the POL defect by analyzing UV absorption of various synthetic silica glasses, which decreased after hydrogen treatment followed by increased value of infra red (IR) OH absorption band, in accordance with [8]. In fair agreement, [17] assigned the band at 7.1 eV (FWHM of 0.7eV, oscillator strength f $\approx$ 0.01) by comparing absorption spectra of oxygen rich silica samples before and after F_2 laser treatment.

First *ab-initio* theoretical estimation was proposed by in the 80's [14] using tight-binding Hamiltonian model on 243 α-quartz cluster. POL defect used parameters of H_2O_2 molecule (1.49 Å O-O distance, 100°dihedral angle) and results show lowest $p\sigma$ to empty $p\sigma^*$ excitation at 8.6 eV. In the study [6] peroxy bridge defect in silica on $Si_2O_8H_6$ cluster (1.43 Å O-O distance) using various configuration interaction (CI) calculations has been studied. They predict the lowest transition at 6.5 $\pm$ 0.3 eV from occupied π^* orbital into conduction band with very low probability (approximately

10^{-4}). Hydrogen peroxide molecule was used as simplified reference to peroxy defect in silica. Their calculations show the first excitation at 6.2 $\pm$ 0.2 eV (oxygen π^* into 3s). The study describe in reference [15] also used CI calculations to model optical excitation of H_2O_2 and reports first excitation at 6.24eV (f=0.0013) from $\sigma \rightarrow \sigma^*$. In [13] even bigger cluster has been used with more advanced approach (configuration interaction with double excitations and coupled cluster methods). Results for largest used cluster ($(H_3SiO)_3Si$-O-O-$Si(OSiH_3)_3$, O-O distance 1.49 Å, dihedral angle 133°) show first weak singlet-to-singlet transitions at 5.5 eV (valence to empty σ^* band, f=0.0001) This study also uses H_2O_2 as a simplified model of the POL defect reporting first transition from π^*-type lone pair to anti bonding $\sigma*$ orbital at 5.95 eV with very low oscillator strength. [18] compared properties of POL-formation in various calculated amorphous-silica models resulting in noticeable site-to-site difference. They proposed that proper characterization of defects requires statistical approach. In related study [19] simulated optics of larger 72-atom models using TD-DFT. They report local defect geometry provides no significant variation of transition energies on the 7 different configurations. The lowest excitation is calculated at 4.45$\pm$0.1 eV as a transition from occupied σ to anti-bonding σ with low oscillator strengths in the 10^{-3} region.

Goal of our research is to model opto-electrical properties of silica containing POL bridge defect using state of the art many body perturbation theory (MBPT) method - GW approximation and solutions to the Bethe-Salpeter equation on large system. This approach is known to provide highest correlation between theory and experiments.

2. Methods

Ground state and mean-field electronic structure has been calculated with the framework of density functional theory - DFT with local density approximation (LDA) and hybrid exchange functionals from Quantum espresso software package [22]. Due to well known deficiency of DFT-LDA for description of empty states the values of wave functions have been corrected using GW approximation. This method is often refereed as GW@DFT or G_0W_0. Optical properties were obtained by solving Bethe-Salpeter equation (BSE) which also includes electron-hole interaction of excited particles and the overlap of electronic wave functions. Both steps were performed using Self Energies and Excitations 2.0.2 (SAX) [27] software. This method currently grants optimal ratio between accuracy and computational costs. Both software packages are based on plane-waves,

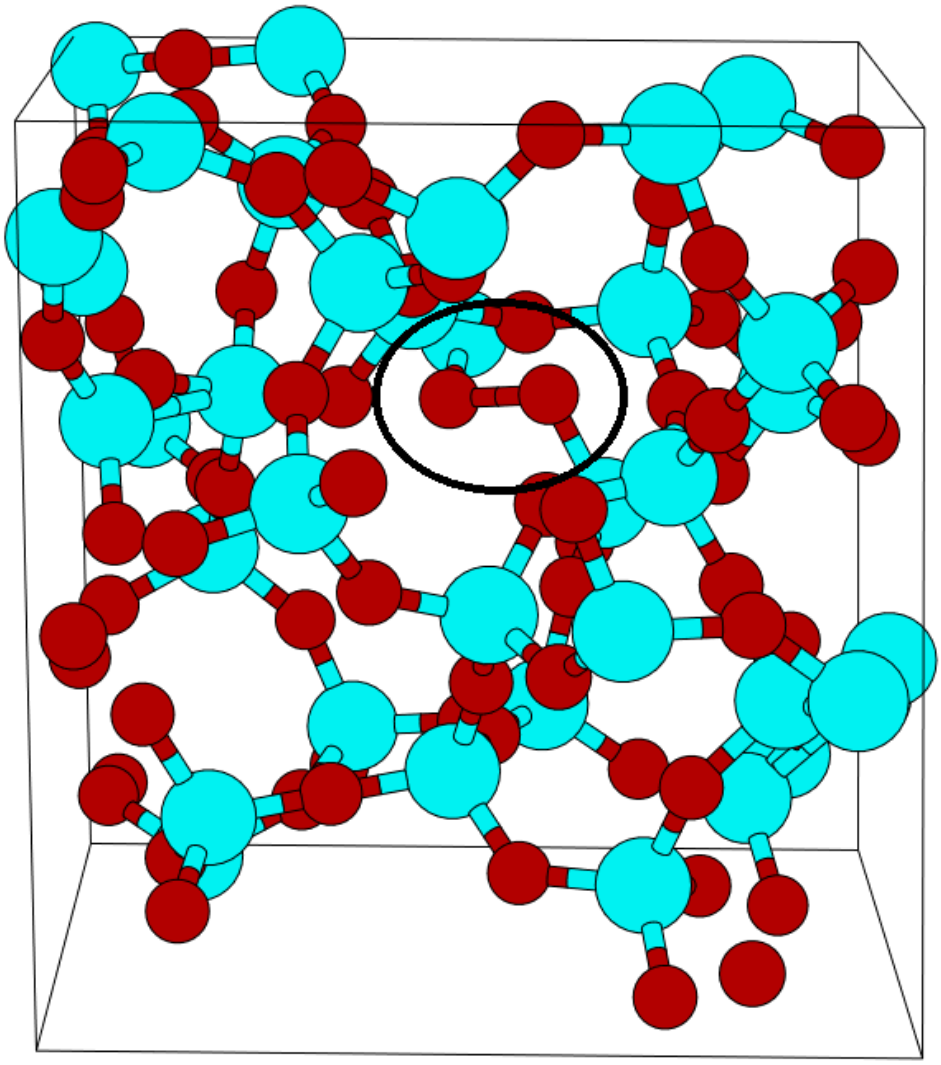

Figure 1: 109 atom amorphous silica model with the lowest formation energy used in the study (labeled as intO27 in table 1). Blue spheres represent silicon atoms and red oxygen atoms. Size of the unit cell is approximately 1 nm. Peroxy bridge defect site is marked with black ellipse

pseudo potentials and periodic boundary conditions. All calculations were performed using Perdew-Zunger-LDA pseudo-potentials [24] available from the Quantum espresso library [22]. Plane-wave energy cut-off was set at appx. 1100 eV to insure dense enough sampling and thus accurate results

even in low energy regime. Similar to previous studies we have considered H_2O_2 as simplified model for peroxyl bridge defect. Simulations were performed on unoptimized structure with O-O distance of 1.474 Å and dihedral angle 111.5°. 160 total electronic states were considered in calculations of simplified model - H_2O_2 molecule and 800 for SiO_2 model. 108 atom silica model was obtained with meld-quench method using semi-empirical molecular dynamics calculations with effective quench rate of 2.6 x 10^{13} Ks^{-1}. An additional oxygen atom was inserted into every oxygen spot in the cell creating 72 different POL defect sites. Detailed description of silica model creation and POL defect formation is provided in [21]. Simulated configurations were systematically selected with respect to their formation energy. Proper statistics of the problem would require simulations of many different systems but due to extreme computational demands of method used in this research only five configurations and reference pure silica were modeled. This approach follows the discussion of [18] stating multiple geometries should be used when modeling amorphous silica.

3. Results and discussion

On the first look our results for hydrogen peroxide molecule are in good agreement with previous studies [13, 6], highest occupied molecular orbitals (HOMO) are $\pi*$ type lone pairs on oxygen atoms followed by σ shaped lowest unoccupied molecular orbitals (LUMO). First absorption occurs at 2.74 eV with very low oscillator strength (f=0.0008) and transition is from HOMO to LUMO.

While nature of transition agrees well with previous studies [13, 6], energy difference is significant as their work show no absorption peaks below

Table 1: Formation energy variations and geometrical properties of all the configurations. Δ angle is provided with respect to 111.5°from hydrogen peroxide molecule while the interatomic distance is expressed with respect to the average length between oxygen atoms in defect

Name	δ E[eV]	D. angle [°]	Δ angle [°]	O-O dist.[Å]	Δ dist. [Å]
intO27	0	106.9	-4.6	1.496	0.022
intO42	0.5503	148.1	36.6	1.498	0.024
intO67	0.6497	164.0	52.5	1.482	0.008
intO41	1.0991	157.2	45.7	1.505	0.031
intO15	1.3812	143.0	31.5	1.515	0.041

6.0 eV. Optical absorption has been measured experimentally in this region for H_2O_2 molecules adsorbed on SiO_2/TiO_2 sol gel substrate [25]. Further analysis of our results indicates that the excitations appear to be complex transitions between many different states. This leads to the presence of delocalized (scattering) states between the LUMO and the vacuum level. No experimental data exists for the Electron Affinity (EA) of hydrogen peroxide. Only theoretical calculations place the EA at -2.5 eV [23]. Vertical ionization potential (VIP) was measured experimentally at 11.6 eV [28, 29]. The difference between our calculated energies and nature of transitions with respect to results reported in literature [13, 6] exists due to the different methods used. Generally Hartree-Fock (HF) and configuration interaction (CI) methods, used in older studies, are based on localized basis sets which provide good accuracy for molecular orbitals but fail completely in the description of delocalized states. On the contrary of the spatial dependent accuracy, precision of plane-waves based methods is energy based thus any electronic state can be accurately described with condition that energy cutoff is large enough [30]. As it can be seen in next paragraphs of this paper, only HOMO-LUMO transition is comparable between simplified and real POL model from which we can conclude that hydrogen peroxide molecule is not good model for optical properties of real POL defect.

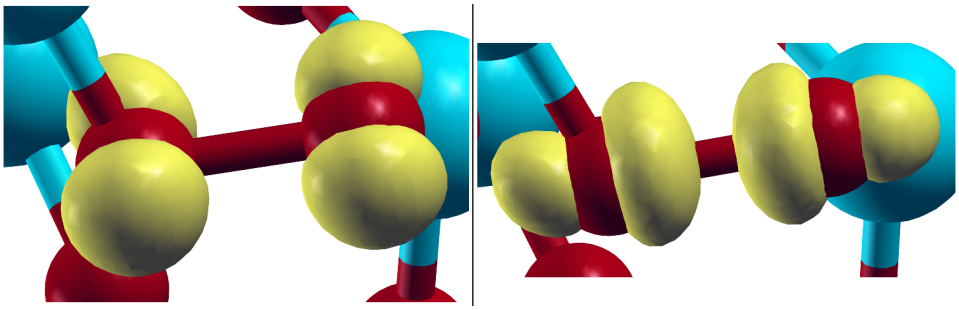

Figure 2: Spatial expectation values of molecular states on peroxy bridge defect: Left - π^* HOMO- Right - σ^* like LUMO

Table 1 summaries formation and geometrical properties of different silica configurations used in this study. All the structures were fully relaxed with variable-cell geometry optimization from QE software [22]. Mean distance between oxygen atoms in relaxed peroxy defect is 1.499 Å. This value provides excellent comparison with some previous studies of [13]. Dihedral angle varies with different configurations and has the average value of 143.8°. The configuration with lowest formation energy (labeled as intO27

Table 2: Average values of the first four possible electronic transitions in silica model containing POL defect.

From	To	Weight	Osc. Str.	Energy[eV]
HOMO	LUMO	0.94±0.01	$6.9 \cdot 10^{-4} \pm 4.4 \cdot 10^{-4}$	3.3 ± 0.4
Valence	LUMO	0.12±0.03	$1.6 \cdot 10^{-3} \pm 6.7 \cdot 10^{-4}$	5.3 ± 0.5
HOMO	Cond.	0.93±0.01	$4.3 \cdot 10^{-4} \pm 3.4 \cdot 10^{-4}$	6.9 ± 0.02
Valence	Cond.	0.91±0.02	$3.6 \cdot 10^{4} \pm 2.1 \cdot 10^{-4}$	7.6 ± 0.1

in table 1) has dihedral angle of 106.9°. As this configuration is closest to energetically favorable H_2O_2 molecule structure it has lowest formation energy. In other configurations it varies from 143°to 164°.

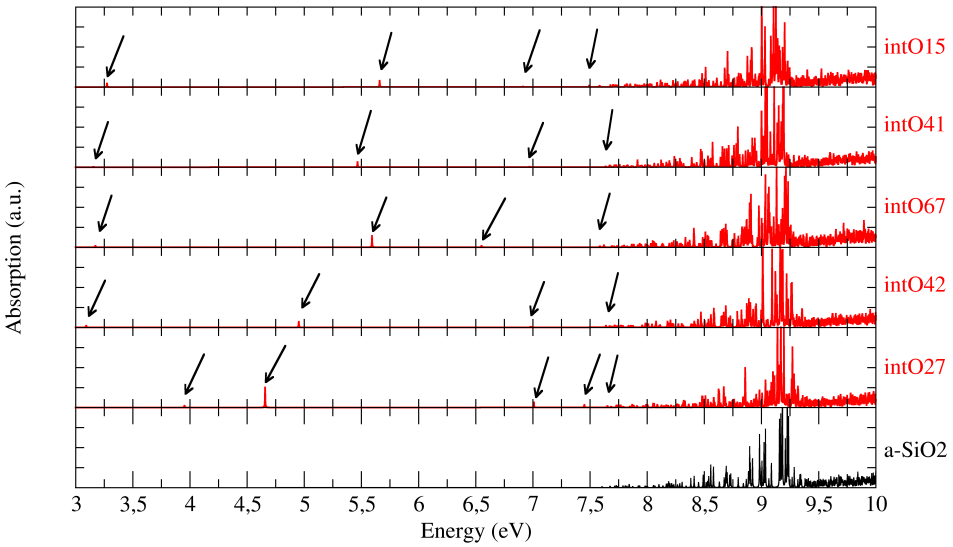

Figure 3: Theoretical spectra of different configurations containing POL defect and reference pure silica spectra. Graphs are oriented by formation energy from lowest at the bottom to highest on the top (formation energies are provided in table 1). Black arrows are used to indicate peaks with lower intensities for the sake of clarification.

Average values of transitions are shown in table 2. Errors are calculated as standard deviation between all configurations. First excitation occurs around 3 eV as a transition from occupied π^* (HOMO) to empty σ^* orbital (LUMO) with oscillator strength in 10^{-4} region. Both are localized on defect oxygen atoms. Second excitation in 5.3 eV region goes from valence

band to empty defect state (LUMO) with a higher probability (10^{-3}). Third transition assigned to POL defect occurs just under 7.00 eV from occupied π^* orbital into conduction and has again very small osc. strength ($\approx 10^{-4}$). Last excitation noted in the table describes transition from valence to the oxygen 3s orbital in 7.5 eV region. It is known from the literature that this state dominates lower conduction band in amorphous silica [26]. Optical

Table 3: Table of first five excitations for the POL configuration with lowest formation energy.

From	To	Weight	Osc. Str.	Energy
HOMO	LUMO	0.935	0.0009	3.95 eV
HOMO-1	LUMO	0.845	0.005	4.65 eV
HOMO	Conduction	0.922	0.0009	7.00 eV
HOMO-1	Conduction	0.918	0.0007	7.45 eV
Valence	Conduction	0.922	0.0002	7.67 eV

properties of configuration with lowest dihedral angle (table 1 - intO27) display different behavior which can be seen in table 3. Because this table describes only one particular case there is no statistical errors. In this configuration first excitation occurs just under 4 eV as a transition from π^* HOMO to σ^* LUMO followed by second transition at approximately 5.5 eV. This is transition from another molecular π^* like state on defect oxygen atoms, positioned on top of valence band, to LUMO, and not valence band to LUMO transition as described in previous paragraph. With this state existing on top of the valence band it creates another absorption related to POL defect due to HOMO-1 transition into conduction before valence→conduction band transition in 7.5 eV region. Again all of the excitations except the second one have oscillator strength in 10^{-4} region. Figure 3 shows the theoretical absorption spectra of all configurations. The spectrum bottom represents pure silica reference and the others are sorted by the formation energy with lowest on bottom. Unlike other studies [6, 13] all of the described transitions have very low oscillator strength. In our opinion it would be very difficult to detect the calculated transitions experimentally and their signal would most probably be covered by signature of other, more active, defects.

Results presented in reference [13] contribute majority of the difference in transition energy to the change of -O-O- inter-atomic distance while our results show no clear correlation in this aspect as seen by comparing the

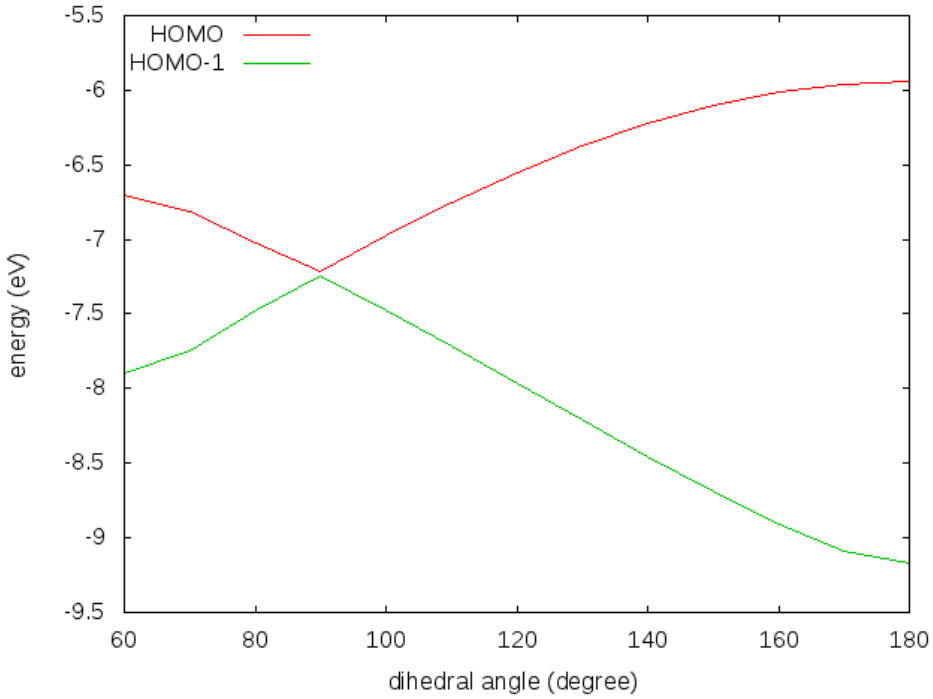

Figure 4: Energy variation of HOMO and HOMO-1 energies of hydrogen peroxide molecule with respect to dihedral angle

table 1 and figure 3. Results for intO27 configuration and results of simpler yet similar hydrogen peroxide model clearly indicate that low dihedral angle tends to pull occupied defect state on top of the valence band.

To clarify how the variation of dihedral angle affects electronic properties, we have performed additional calculations on series of rotated hydrogen peroxide molecules (molecule was rotated around O-O axis). Since the HOMO and HOMO-1 states are very similar their relative lowest energy configuration occurs when states are placed orthogonally with respect to each other as seen in the figure 4. This confirms the dominating effect of defect's dihedral angle to the electronic transitions from π orbitals which dominate the top of the valence band. Inter-atomic distance is obviously more important in properties of empty σ bond, but was not extensively studied in present work as the HOMO-LUMO transitions show no dependence on the inter-atomic distance and dihedral angles (figure 3, intO42-intO15). Because the dihedral angle of lowest formation energy model (intO27) is much smaller compared to other configurations, the energy dif-

Table 4: Energy levels from GW method. On the left average values of the energies for all the systems. Right - energy levels of lowest formation energy (LFE) configuration with the addition of HOMO-1 state

GW state	Energy [eV]	GW LFE state	Energy [eV]
HOMO	0.85±0.20	HOMO-1	0.312
Conduction	9.45±0.03	HOMO	0.762
LUMO	10.32±0.13	Conduction	9.4688
		LUMO	10.266

ference of HOMO/HOMO-1 is smaller so HOMO-1 state resides on top of valence band and not inside of it. This allows additional transitions from this state into empty defect states. Table 4 shows GW corrected energy levels for silica models confirming this effect is also present in silica and not only in simplified model. Neither of those parameters affects bottom of conduction as it is purely described by the symmetrical 3s orbital of oxygen [26].

Older studies based on CI only predict either transitions from HOMO positioned on defect to 3s of oxygen embedded in the conduction band [6] or valence to empty σ transition [13]. Our results predict the former excitation just bellow 7 eV providing decent match with 6.5 eV of [6]. Valence-LUMO transition presented in this work occurs at 5.27 eV which again agrees well with 5.5eV of [13]. In configuration with lowest formation energy this excitation occurs even lower at 4.65 eV. This study again shows no presence of empty σ band inside the valence gap as suggested by [14] and place it into conduction (table 4) in agreement with [6].

4. Conclusions

We have modeled peroxy link defect in amorphous silica using state of the art GW@DFT method. Our results show presence of the following defect induced transitions within band gap: transition from π^* HOMO to σ^* LUMO near 4 eV has not been previously reported while our result of valence $\rightarrow$ LUMO around 5.3 eV and HOMO $\rightarrow$ conduction near 7 eV excitations agree well with previous studies. Because of low oscillator strengths we believe these transitions would be very difficult to detect experimentally and would be covered by other, more active absorptions from other defects and impurities. Detailed study shows dominating effect of local

geometry is dihedral angle which effects low-lying electronic excitations. It promotes π HOMO-1 state on top of valence band creating additional transition options that origin from this state.

5. Acknowledgements

The research was suported by "Young Researcher" grand of the Slovenian research agencs (ARRS). Computational part was performed using GENCI-CCRT High performance computing resources, HPC Jade (DARI Grant number 2014096137).

References

[1] W. D. Callister, D. G. Rethwisch, Fundamentals of materials science and engineering, John Wiley & Sons Inc (2008)

[2] Intel ®corp., Intel ®14 nm Technology, `http://www.intel.com/content/www/us/en/silicon-innovations/intel-14nm-technology.html` (23.1.2015).

[3] T. Kakuta, T. Shikama, T. Nishitani, B. Brichard, A. Krassilinkov, A. Tomashuk, S. Yamamoto, S. Kassai, J. Nucl. Mater. 307, 1277 (2002).

[4] S. Girard, J. Biaggio, J.-L. Leray, Meunier, A. Boukenterm Y. Ouerdane, IEEE Trans. Nucl. Sci. 52, 1497 (2005).

[5] W. J. Hogan, E. I. Moses, B. E. Warner, M. S. Sorem, J.M. Soures, Nucl. Fusion 41, 567 (2001).

[6] G. Pacchioni and G. Ierano, Phys. Rev. B 57, 818 (1998).

[7] L. Skuja, M.Hirano, H. Hosono, K. Kajihira, Phys. Stat. Sol. 2, 15 (2005).

[8] H. Nishikawa, R. Tahmon, Y. Ohki, K. Nagasawa, Q. Hama, J. Appl. Phys. 65, 4672 (1989).

[9] K.Awazu, H. Kawazoe and K. Muta, T. Ibuki, K. Tabayashi, K. Shobatake, J. Appl. Phys. 69, 1849 (1991).

[10] K.Awazu, K. Harada, H. Kawazoe and K. Muta, J. Appl. Phys. 72, 4696 (1992).

[11] Y. Sakurai, J. of Non-Crys. Solids 276, 159 (2000).

[12] H. Imai, K. Arai, H. Hosono, Y. Abe, T. Arai and H. Imagawa, Phys. Rev. B 44, 1812 (1991).

[13] B. B. Stefanov and K. Ragnavachari, J. Chem. Phys. 111, 8039 (1999).

[14] E. O'Reilly and J. Robertson, Phys. Rev. B 27, 3780 (1983).

[15] A. Rauk, J. M. Barriel, Chem. Phys. 25, 409 (1977).

[16] E. J. Friebele, D. L. Griscom, M. Stapelbroek, R. A. Weeks, Phys. Rev. Lett. 42, 1346 (1979).

[17] L. Skuja, K. Kajihara, T. Kinoshita, M. Hirano, H. Hosono, Nucl. Intrum. Methods Phy. Res. B 191, 127 (2002).

[18] M. A. Szymanski, A. L. Shluger, A. M. Stoneham, Phys. Rev. B 63, 224207 (2001).

[19] D. Ricci, G. Pacchioni, M. A. Szymanski, A. L. Shluger, A. M. Stoneham, Phys. Rev. B 64, 224104 (2001).

[20] A. Kokalj, Comp. Mater. Sci. 28, 155 (2003).

[21] L. Martin-Samos, Y. Limoge, J.-P. Crocombette and G. Roma, Phy. Rev. B 71, 014166-1 (2005).

[22] P. Giannozzi, *et al.*, J. Phys. Cond. Mat. 21, 395502 (2009).

[23] J. Hrusak, H. Friedrichs, H. Schwarz, H. Razafinjanahary, H. Chermete, J. Phys. Chem. 100 , 100 (1996).

[24] J. P. Perdew, A. Zunger, Phys. Rev. B 23, 5048 (1981).

[25] J. E. Gonalves, U.P. R.Filho, D.W. Franco, Y. Gushikem, Eclet. Qum. 32 (2007).

[26] N. Richard, L. Martin-Samos, S. Girard, A. Ruini, A. Boukenter, Y. Ouerdane, J.-P. Meunier, J. Phys: Con. Matter 25, 1 (2013).

[27] L. Martin-Samos, G. Bussi, Comp. Phys. Comm. 180, 1416 (2009).

[28] K. Osafune, K. Kimura, Chem. Phys. Lett. 25, 47 (1974).

[29] R. S. Brown, Can. J. Chem. 53, 3439 (1975).

[30] Richard M. Martin, Electronic structure: Basic theory and practical methods, Cambridge university press (2004)